ALMA MATER STUDIORUM · UNIVERSITÀ DI BOLOGNA

SCUOLA DI SCIENZE
Corso di Laurea Magistrale in Astrofisica e Cosmologia

Magnetic field in the outskirts of PSZ2 G096.88+24.18 from depolarization analysis of radio relics

Relatore:
Chiar.ma Prof.ssa
Annalisa Bonafede

Correlatore:
Dott.ssa
Chiara Stuardi

Presentata da:
Emanuele De Rubeis

Appello III
Anno Accademico 2021/2022

Abstract

Galaxy clusters are the most massive virialized structures existing in our Universe. Their low frequency radio emission reveals the presence and properties of relativistic particles and magnetic fields. Cluster diffuse radio sources, not associated with individual cluster galaxies, allow us to investigate the acceleration processes that involve the charged relativistic particles that emit in the radio frequencies and the characteristics of the magnetic field with whom these particles interact.
Radio relics are one of the different types of diffuse radio sources present in a fraction of galaxy clusters. They are characterized by elongated arc-like shapes, with sizes that range between 0.5 and 2 Mpc, and highly polarized emission (up to ∼60%) at GHz frequencies. These properties are expected for sources that trace shocks waves in the cluster outskirts. Radio relics are in fact extraordinary examples of the consequences of the propagation of shocks through the cluster after a cluster-cluster merger. The connection between shock waves and relics is supported by the temperature and surface brightness discontinuities derived from the X-ray bremsstrahlung emission of the intracluster medium (ICM) at the position of the relics.

The polarized emission of radio relics can be used to study the magnetic field properties of the host cluster. During their passage, shock waves compress the magnetized ICM. Hence, the observed polarization angles are generally found to be well aligned perpendicular to the shock front. The linearly polarized synchrotron radiation, moving through a magnetized plasma which is the ICM, is affected by the rotation of the linear polarization vector. This rotational effect, known as "Faraday rotation", can cause a decrease of the observed polarization fraction with respect to the intrinsic one. The study of this effect, provided the distribution of the electron density is known, allows us to constrain the magnetic field projected along the line of sight.

The aim of this thesis work is to constrain the magnetic field intensity and distribution in the periphery of the cluster PSZ2 G096.88+24.18: this cluster has already called the interest because it hosts a pair of radio relics, perpendicular with respect to the merger axis of the cluster, that can be used for polarization analysis.
(Jones et al., 2021) found different polarization fractions for the North and South relics. The northern relic shows a fractional polarization between 10-60%, which is expected in a scenario where, due to the shock, magnetic field is well ordered and compressed along the shock front. Unexpectedly, instead, the southern relic shows a much lower polarization with respect to the northern one, with a maximum of 20% of polarization fraction observed only in the brightest region.
Jones et al. (2021) suggest that the depolarization is caused by the turbulence in the ICM, but the magnetic field contribution has yet to be investigated.

To analyse the polarization properties of the relics in PSZ2 G096.88+24.18 radio relics we used new Jansky Very Large Array (VLA) observations in L-band (1-2 GHz with B and D array), together with archival observations (published by Jones et al., 2021). These data allow us to conduct a polarization analysis with better

angular resolution and higher sensitivity to the extended emission with respect to previous studies.
The polarization study has been performed using the Rotation Measure Synthesis technique, which allows us to recover information about the magnetic field along the line of sight weighted by the electron density of the thermal gas. This technique allows us to exploit the full 1-2 GHz observing band taking bandwidth depolarization into account.
Thanks to more sensitive data, we were able to recover a good fractional polarization for the two relics, and we found a highly polarized region ($\sim$ 28%) in the western edge of the southern relic.
Moreover, using the RM synthesis technique, we gained even more polarization from the southern relic, with values up to $\sim$ 13% for the EAST region and $\sim$ 51% for the WEST region.
We studied also the depolarization trend with the resolution for the southern relic, and found that the polarization fraction decreases with the beamsize. This indicates a contribution of the external medium to the observed polarization fraction.

Finally, we have produced simulated magnetic fields models, varying the auto-correlation lengths of the magnetic field, in order to reproduce the observed depolarization trend in the southern relic.

Comparing our observational results and model predictions, we were able to constrain the scales over which the turbulent magnetic field varies within the cluster. We found, for the two regions (E and W) selected for the southern relic, a best-fit combination of scales $\Lambda_{min} - \Lambda_{max}$ of 45-150 kpc and 45-200 kpc, respectively, with an average magnetic field within 1 Mpc $\langle B_{1Mpc^3} \rangle \sim 1.31$ μG.

We conclude that the depolarization observed in the southern relic is likely due to external depolarization caused by the magnetized ICM distribution within the cluster.

Contents

1 Galaxy clusters and radio relics **1**
- 1.1 Emission from galaxy clusters . . . 1
  - 1.1.1 Optical and infrared emission . . . 2
  - 1.1.2 X-ray emission . . . 3
  - 1.1.3 Inverse-Compton scattering and Sunyaev-Zel'dovich effect . . . 4
  - 1.1.4 Radio emission . . . 7
- 1.2 Diffuse radio emission in galaxy clusters . . . 11
  - 1.2.1 Diffuse cluster radio sources classification . . . 11
  - 1.2.2 Magnetic fields in galaxy clusters . . . 14
  - 1.2.3 Particle acceleration mechanisms . . . 20
- 1.3 Radio relics . . . 21

2 Polarization and Faraday rotation effect **27**
- 2.1 Polarization . . . 27
- 2.2 Faraday rotation effect . . . 28
- 2.3 Depolarization mechanisms . . . 30
- 2.4 RM synthesis . . . 31
  - 2.4.1 Faraday dispersion function deconvolution . . . 34

3 Interferometry fundamentals and radio telescopes imaging **36**
- 3.1 Radio interferometry . . . 36
- 3.2 Synthesis imaging . . . 39
  - 3.2.1 The `CLEAN` algorithm . . . 39
  - 3.2.2 Self-Calibration . . . 41
  - 3.2.3 Primary beam correction . . . 41
  - 3.2.4 Robust Weighting . . . 42
- 3.3 Wide-band and wide-field imaging . . . 43
  - 3.3.1 W-projection . . . 43
  - 3.3.2 Image modes and deconvolution algorithms . . . 44
  - 3.3.3 w-stacking . . . 46
  - 3.3.4 Multi-scale cleaning . . . 46

4 PSZ2 G096.88+24.18 **48**

5 Data analysis: imaging and the application of Rotation Measure synthesis technique **52**
- 5.1 Data used in this thesis work and imaging . . . 52

5.1.1 D-configuration 53
5.1.2 C-configuration 54
5.1.3 B-configuration 54
5.2 Polarization imaging with WSClean 56
5.3 Polarization results 56
5.3.1 Integrated polarization results 56
5.3.2 RM synthesis technique results 59
5.4 Polarization at different resolutions 62

6 Simulations results and discussion **70**
6.1 Magnetic field modeling 70
6.1.1 Simulations of RM maps 70
6.1.2 Determination of the simulations parameters 72
6.2 Results and discussion 74
6.2.1 Polarization results in the E and W regions of the relic 75

7 Conclusion and future perspectives **80**

Chapter 1

Galaxy clusters and radio relics

Clusters of galaxies are the most massive gravitationally bound systems in the Universe, with masses that typically range within $10^{14} - 10^{15}\ M_\odot$ and virial radius of $1 - 5$ Mpc, where virial radius is defined as

$$r_{vir} = \left[\frac{2GM_{vir}}{\Delta_c(z)H^2(z)}\right]^{1/3}, \tag{1.0.1}$$

where Δ_c is the critical overdensity for virialisation, which depends on the cosmology, and $H(z)$ is the Hubble parameter (Cimatti et al., 2019).
They were for the first time mentioned probably by Charles Messier in 1784 and were identified as galaxies concentrations: nevertheless, we know now that these systems are more complex than expected, with galaxies that constitute only a small fraction of their mass. In fact, the most important baryonic component is represented by a hot ($10^7 - 10^8$ K) and low density ($\sim 10^{-3}$ cm^{-3}) thermal plasma permeating the cluster volume called intracluster medium (ICM) which represents $\sim$ 15% of the total mass (Arnaud and Evrard, 1999, Vikhlinin et al., 2006). Galaxies constitute only about 5% of the cluster mass and they are typically elliptical. The largest part of the mass ($\sim$ 80%) of galaxy clusters (GC) is in the form of dark matter (DM), which exhibits only through dynamical effects, such as gravitational lensing.
According to the standard cosmological model Lambda-CDM (ΛCDM), these cosmic structures form in a hierarchical formation process through the whole life of the Universe in what is called "bottom-up" scenario, so they are formed at low redshifts (z$\geq$0.1, Kravtsov and Borgani, 2012). Merger of galaxy clusters are the most energetic phenomena in the Universe, with a dissipated energy that can be as large as 10^{64} erg in a life-time of $\sim 10^9$ yr. Most of this energy is dissipated through shocks and thermalised in the ICM (Brunetti and Jones, 2014). A fraction of this energy, though, is likely responsible for the existence of diffuse radio emission (see Sec. 1.1.4).

1.1 Emission from galaxy clusters

A multi-wavelength approach is necessary in order to have a complete view of galaxy clusters and of their different components.

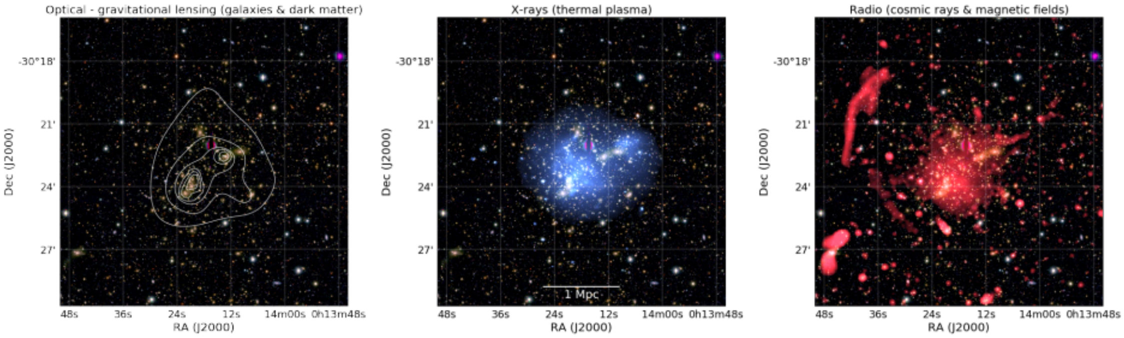

Figure 1.1: The galaxy cluster Abell 2744. in optical, X-ray, and radio. White contours on the optical (left) image represent the mass surface density derived from weak lensing. In the middle panel, the 0.5-2.0 keV X-ray emission reveals the thermal ICM. The radio emission at 1.4 GHz is shown in the right panel (van Weeren et al., 2019, and references within).

1.1.1 Optical and infrared emission

Optical and IR observations are suitable for the analysis of the baryons which are in form of stars in galaxies. Galaxies within GCs are typically early-type galaxies (ETG), as we expect from the morphology-density relation (Dressler, 1980), and in general galaxies in this environment are different from the field ones. Indeed, the interplay between cluster galaxies and ICM has an important impact on their interstellar medium (ISM).

There is strong evidence that star formation is suppressed when galaxies enter high density environments such as cluster, especially in the central regions. Spirals are also present in clusters, although outnumbered, and they show peculiar properties not typically found in the field spirals: they show a lack of gas, also known as "HI deficiency", that could be related to different factors such as collision between galaxies (Spitzer and Baade, 1951), ram pressure ablation (Gunn and Gott, 1972), gas stripping (Kritsuk, 1983, Tarter, 1975) and evaporation of the ISM (Cowie and Songaila, 1977). The fact that this gas deficiency afflicts mostly the galaxies in the central regions suggests that some of these processes (or a combination of them) are more relevant in a denser environment.

Moreover, in this particular environment, is possible to find the most massive galaxies in the Universe, located in the cluster cores and known as "brightest cluster galaxies" (BCG). These are the most massive and luminous galaxies in clusters and, despite their similarities in color and morphology with ETG, they reveal some remarkable features as the presence of blue stars (Crawford et al., 1999), extended low-surface brightness halos (Oemler, 1976) and the prevalence of radio-loud active galactic nuclei (AGN). These properties can be mostly explained assuming that BCG are formed by the merger of several massive galaxies early in cluster history within the cluster core, in a process known as "galactic cannibalism" (Nipoti, 2017, and references within).

Gravitational encounters between objects, especially in the central regions, can conversely explain the presence of extended envelopes surrounding these galaxies that constitute the so-called "intra-cluster light" (ICL): this diffuse optical light permeates the denser regions of GCs and is due to stars being stripped away from the central galaxies.

1.1.2 X-ray emission

As we mentioned above, the baryonic matter of GCs is mostly ($\sim 75\%$) in form of a hot and rarefied plasma called ICM which permeates the clusters volume. This gas is characterized by X-ray thermal emission through the bremsstrahlung mechanism (Fig. 1.2). For a plasma with a temperature T and an ion number density n_i, the bremsstrahlung specific emissivity at a frequency ν is

$$\epsilon_\nu \propto Z^2 \, n_e \, n_i \, g_{ff}(Z, T, \nu) \, T^{-1/2} e^{-\frac{h\nu}{k_B T}} \tag{1.1.1}$$

where Z is the atomic number, n_e the electron number density, k_B is the Boltzmann constant, and g_{ff} is the Gaunt factor which accounts for quantum mechanics effects. The exponential cut-off allows to obtain the ICM temperature from X-ray observations, which is typically about $3 - 10$ keV.

Galaxy clusters can be found using this X-ray diffuse emission since they are very luminous in this band, with $L_X \sim 10^{45}$ erg s^{-1}: this is still one of the easiest way to select GCs, given that with respect to the optical surveys this technique is less vulnerable to accidental line-of-sight projection effects.

The X-ray emission can give us important information about the total mass distribution. In fact, knowing the density ρ and temperature T radial distribution, it is possible to derive the total mass within a certain radius r assuming a gas distribution in hydrostatic equilibrium and spherically symmetric

$$M(\leq r) = -\frac{k_B T r^2}{G \mu m_p} \left[\frac{d \ln \rho}{dr} + \frac{d \ln T}{dr} \right], \tag{1.1.2}$$

where m_p is the proton mass, while μ represents the mean atomic weight and depends on the mass abundances of the gas.

The radial distribution of density and temperature can be found fitting analytical models to reproduce normalization and shape of the observed X-ray surface brightness profile and spectrum, respectively.

For example, a typical model used for the gas density within GC is the so-called "β-model" (Cavaliere and Fusco-Femiano, 1978)

$$\rho(r) = \rho(0) \left[1 + \left(\frac{r}{r_c} \right)^2 \right]^{-3\beta/2}, \tag{1.1.3}$$

where r_c is the "core radius" and

$$\beta \equiv \frac{\mu m_p \sigma_r^2}{k_B T},$$

with σ_r being the galaxies velocity dispersion (Sarazin, 1988). In this model the distribution of gas is assumed to be spherically symmetric and isothermal.

X-ray spectra provide information about the chemical composition and temperature of the ICM within a cluster, being characterized by a continuum from thermal bremsstrahlung and emission lines from highly ionized species. Spectral analysis reveals the presence of highly ionized metals, such as Fe, C, O, Ne, Si, S, Mg, and more, that can give us constraints about both temperature and cluster abundance

through line-to-continuum ratios (Boehringer and Werner, 2009). A typical abundance value for the ICM is ∼1/3 of solar metallicity: this implies that not all gas has a primordial origin from clusters formation processes, but part of it has been enriched by the activity from cluster galaxies (Arnaud et al., 1992).
Gas in the central regions of many relaxed clusters has a radiative cooling time that is much shorter than the Hubble time.

$$t_{cool} = \frac{5}{2}\frac{k_B \rho_{gas} T_{gas}}{\mu m_p}\frac{1}{n_e n_i \Lambda}, \tag{1.1.4}$$

where $\Lambda = \Lambda(T, Z)$ is called "cooling function".

In the absence of a heating source, a cooling flow is expected to develop, whereby the temperature in the central region of the cluster drops and gas flows inwards.

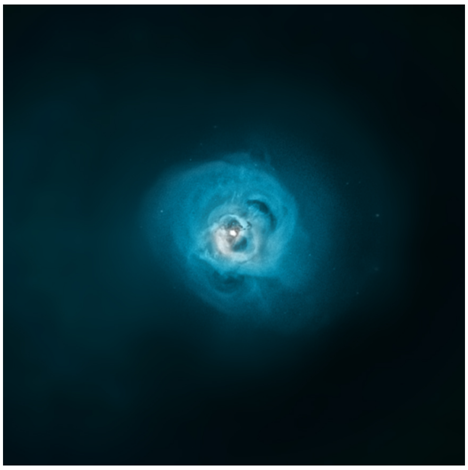

Figure 1.2: Chandra and XMM-Newton combined image of Perseus cluster (Bulbul et al., 2014).

X-ray observations show these temperature drops in some cluster cores (named "cool core clusters"), but there is much less cool gas than what would be expected from the short radiative cooling time. Therefore, some source of heating must balance the radiative losses. Radio galaxies, associated with the BCG, have been identified as the main source of energy input into the ICM (Churazov et al., 2002). X-ray observations show numerous cavities in cool core clusters, coincident with the lobes of the central radio galaxy (e.g. McNamara et al., 2005). Here the radio plasma has displaced the X-ray emitting gas, creating a low-density bubble which rises buoyantly and expands, distributing energy to the surrounding ICM. This process is commonly referred to as "radio-mode" feedback (Fabian, 2012).

1.1.3 Inverse-Compton scattering and Sunyaev-Zel'dovich effect

In inverse-Compton (IC) scattering, ultra-relativistic ($\gamma \gg 1$, where $\gamma = \left(1-\frac{v^2}{c^2}\right)^{-1/2}$ is the Lorentz factor) electrons scatter low energy photons to high energies so that the photons gain energy at the expense of the kinetic energy of the electrons. In this process, contrarily to what happens in the Compton scattering, the electrons lose energy in favour of photons.

If the energy of the photon is $h\nu$ and the angle of incidence is θ in S (laboratory frame), its energy in the electron rest frame S' is, according to the relativistic Doppler shift formula,

$$h\nu^{'} = \gamma h\nu[1 + (v/c)\cos\theta]. \tag{1.1.5}$$

Provided $h\nu \ll m_e c^2$, the Compton interaction in the rest frame of the electron is Thomson scattering and hence the energy loss rate of the electron in S' is the rate at which energy is reradiated by the electron

$$-\left(\frac{dE}{dt}\right)^{'} = \sigma_T c U_{rad}^{'}, \tag{1.1.6}$$

where $U_{rad}^{'}$ is the energy density of the radiation field in the rest frame of the electron, and

$$\sigma_T = \frac{8\pi}{3}\left(\frac{e^2}{m_e c^2}\right)^2 \simeq 6.65 \times 10^{-25}\,\mathrm{cm}^2 \tag{1.1.7}$$

is the Thomson cross section (e is the electron charge and m_e is the electron mass). For the complete calculations, we remind you to Longair (2011). We obtain that

$$U_{rad}^{'} = \frac{4}{3}U_{rad}\left(\gamma^2 - \frac{1}{4}\right), \tag{1.1.8}$$

and, substituting into Eq. 1.1.6, given that $(dE/dt) = (dE/dt)^{'}$,

$$\frac{dE}{dt} = \frac{4}{3}\sigma_T c U_{rad}\left(\gamma^2 - \frac{1}{4}\right). \tag{1.1.9}$$

This is the energy gained by the photon field due to the scattering of the low energy photons.

We have therefore to subtract the initial energy of the low-energy photons to find the total energy gain of the photon field in S. The rate at which energy is removed from the low-energy photon field is $\sigma_T c U_{rad}$ and therefore, subtracting,

$$\frac{dE}{dt} = \frac{4}{3}c\sigma_T U_{rad}\left(\gamma^2 - \frac{1}{4}\right) - c\sigma_T U_{rad} = \frac{4}{3}c\sigma_T U_{rad}(\gamma^2 - 1). \tag{1.1.10}$$

Using the identity $(\gamma^2 - 1) = (v^2/c^2)\gamma^2$, the loss rate in its final form is

$$\left(\frac{dE}{dt}\right)_{IC} = \frac{4}{3}c\sigma_T \gamma^2 \beta^2 U_{rad}, \tag{1.1.11}$$

where $\beta = (v/c)$. Notice the remarkable similarity of this result with the Eq. 1.1.21 for the mean energy loss rate of the ultra-relativistic electron by synchrotron radiation (see Sec. 1.1.4).

Clusters of galaxies can be detected in the microwaves because of an effect on the cosmic microwave background (CMB) known as "Sunyaev-Zel'dovich effect" (SZE, Sunyaev and Zeldovich, 1970). The CMB is characterized by a black-body spectrum at temperature $T_{CMB} \simeq 2.726$ K. The free electrons of the ICM scatter the CMB photons and produce a distortion of the CMB spectrum. The importance of the photon-electron interaction is quantified by the optical depth

$$\tau = \sigma_T \int n_e(x_{los})\, dx_{los}, \tag{1.1.12}$$

where the integral is through the entire cluster along the line of sight (labelled by x_{los}).

As the characteristic energy of the CMB photons is much lower than the energy of the cluster electrons, the result of the interaction is an inverse Compton scattering, with a consequent distortion of the CMB spectrum at the position of the cluster in the plane of the sky. Here we report the main equations describing the SZE in the case of non-relativistic electrons (Birkinshaw, 1999).

A photon of original frequency ν after the scattering has frequency $\nu + \Delta\nu$, with $\Delta\nu/\nu \approx k_B T_e/(m_e c^2)$, where T_e is the temperature of the electrons. Thus, the distorted spectrum is not a black-body spectrum because $\Delta\nu$ depends on ν at given T_e.

At given frequency ν, the spectrum of the emerging radiation can be characterized by the brightness temperature, that, for an unperturbed spectrum, corresponds to the T_{CMB}.

The spectral distortion can be written in terms of T_b as

$$\frac{\Delta T_b}{T_b} = \frac{\Delta I_\nu}{I_\nu}\frac{d\ln T_b}{d\ln I_\nu} = f(x)y, \tag{1.1.13}$$

where I_ν is the intensity at frequency ν, $x \equiv h\nu/(k_B T_b)$, $f(x) = x\coth(x/2) - 4$, and

$$y \equiv \int \frac{k_B T_e(\tau)}{m_e c^2}\, d\tau = \int \frac{k_B T_e(x_{los})}{m_e c^2}\, n_e(x_{los})\sigma_T\, dx_{los} \tag{1.1.14}$$

is the “Compton y-parameter”, which is a dimensionless quantity.

As illustrated in Fig. 1.3, the distortion of the spectrum is such that the intensity (and the brightness temperature) decrease at $\nu < 218$ GHz and increase at $\nu > 218$ GHz.

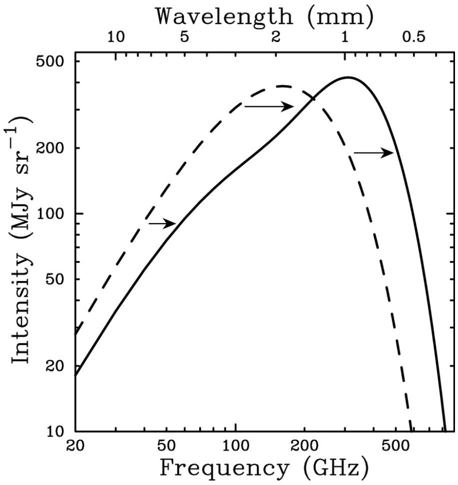

Figure 1.3: Unperturbed black-body CMB spectrum (dashed curve) and CMB spectrum distorted by the SZE (solid curve), which is also known as “thermal SZE” because is due to the thermal motion (Carlstrom et al., 2002).

In the Rayleigh-Jeans regime (low frequency, $h\nu \gg k_B T_b$), $f(x)$ tends to -2 and the variation of brightness temperature is

$$\frac{\Delta T_b}{T_b} = -2y = -\frac{2k_B\sigma_T}{m_e c^2}\int n_e(x_{los})T_e(x_{los})\,dx_{los}. \tag{1.1.15}$$

Therefore, in low-frequency data, galaxy clusters appear as lower-temperature regions in CMB maps. The SZE is small ($\Delta T_b/T_b < 10^{-3}$), but independent on the cluster distance, so it is extremely important especially for studying high-redshift clusters.

With spatially resolved SZE observations it is possible, for a given cluster, to obtain a map of $\Delta T_b/T_b$ and therefore a map of the Compton y-parameter, which can be used to constrain the gas pressure distribution within the cluster ($P \propto n_e T_e \propto y$). When the SZE observation of the cluster is not spatially resolved, the only available measure is the “Compton integrated y-parameter”

$$Y = \int y\,dA = \frac{k_B\sigma_T}{m_e c^2}\int n_e T_e\,dV, \tag{1.1.16}$$

where dA is the projected area element, $dV = dA\,dx_{los}$ is the volume element and the integrals are performed over the entire cluster.

The effect just described is due to thermal motion and is therefore sometimes called the “thermal SZE”. If a cluster has non-negligible peculiar velocity (e.g. it is moving with respect to the CMB), there is an additional spectral distortion of the CMB, known as the “kinetic SZE”, that can only be observed at frequencies close to 218 GHz.

PSZ2 G096.88+24.18, the cluster on which this thesis work is based, has been detected through the SZ effect by the Planck satellite (Planck Collaboration et al., 2016), as later presented in Ch. 4.

1.1.4 Radio emission

Galaxy clusters are also observed in radio band thanks to both AGN and ICM.

The synchrotron radiation is produced by ultrarelativistic particles when they are accelerated in presence of magnetic fields. In a uniform magnetic field B, the particle moves along the magnetic field line on a helical path with constant linear and angular speeds. The orbital angular frequency is

$$\omega = \frac{qB}{(\gamma m)c}, \tag{1.1.17}$$

where q and m are the charge and mass of the charged particle.

If the particle moves with an angle θ between its velocity $\mathbf{v}$ and the magnetic field $\mathbf{B}$, called “pitch angle”, the synchrotron power that emits can be written as

$$\frac{dE}{dt} = \frac{2q^2 a_\perp^2 \gamma^4}{3c^3} \qquad (a_\parallel = 0). \tag{1.1.18}$$

To calculate $a_\perp$, combine force balance in a circular orbit to get

$$a_\perp \equiv \frac{dv_\perp}{dt} = \omega v \sin\theta = \frac{qBv\sin\theta}{\gamma mc}. \tag{1.1.19}$$

Inserting $a_\perp$ into Eq. 1.1.18 gives the power radiated by a single particle moving with pitch angle θ. Given the mass dependencies, lighter particles lose more energy radiatively so we will use from now the electron charge and mass

$$\frac{dE}{dt} = \frac{2e^2}{3c^3}\gamma^2 \frac{e^2B^2}{m_e^2c^2} v^2 \sin^2\theta. \tag{1.1.20}$$

During their lifetimes, electrons are scattered repeatedly by magnetic field fluctuations and charged particles in their environment, and the distribution of their pitch angles gradually becomes random and isotropic. The average synchrotron power per relativistic electron in a source with an isotropic pitch angle distribution is

$$\left(\frac{dE}{dt}\right)_{sync} = \frac{4}{3}c\sigma_T\gamma^2\beta^2U_B, \tag{1.1.21}$$

where $U_B = B^2/(8\pi)$ is the magnetic energy density.
The energy distribution of relativistic electrons in most synchrotron sources is roughly a power law

$$N(E)dE \propto E^{-\delta}dE \tag{1.1.22}$$

where $N(E)dE$ is the number of electrons with energies E to $E + dE$. The relative flux density is then

$$S_\nu \propto B^{(\delta+1)/2}\,\nu^{(1-\delta)/2}. \tag{1.1.23}$$

Thus the spectrum of optically thin synchrotron radiation from a power-law distribution $N(E) \propto E^{-\delta}$ of electrons is also a power-law, and the spectral index α depends only on δ

$$\alpha = \frac{\delta - 1}{2}. \tag{1.1.24}$$

For a typical value of the spectral index $\alpha \approx 0.75$ near $\nu \approx 1$ GHz, we have $\delta \approx 2.5$. In the optically thin regime of sources of synchrotron radiation, spectral breaks or cut-offs are often observed.
In addition, different regions within individual sources may display spectral index variations. Both of these phenomena can be attributed to the effects of ageing of the spectrum of these electrons within the source regions and so provide useful information about time-scales. The lifetimes τ of the electrons in the sources regions are

$$\tau = \frac{E}{(dE/dt)} = \frac{m_ec^2}{(4/3)c\sigma_T\gamma U_B}. \tag{1.1.25}$$

For example, for typical extended powerful radio sources $\gamma \sim 10^3$ and $B \sim 10\ \mu$G, and so the lifetimes of the electrons are expected to be $\tau \leq 10^7 - 10^8\ yr$.

To obtain a quantitative description of the resulting distortions of synchrotron radiation spectra it is convenient to introduce the "diffusion-loss equation" for the electrons

$$\frac{\partial N(E)}{\partial t} = D\Delta^2 N(E) + \frac{\partial}{\partial E}[b(E)N(E)] + Q(E,t), \tag{1.1.26}$$

where D is the diffusion coefficient, $b(E) = -(dE/dt)$, and $Q(E)$ is a source term which describes the rate of injection of electrons and their injection spectra into the source region.

Suppose that there is a continuous injection of electrons with a spectrum $Q(E) = kE^{-\delta}$ for a time t longer than the lifetimes of the individual electrons involved. If synchrotron radiation is the only important loss process, an electron of energy E_b loses all its energy in a time τ such that $(dE/dt)_{t=\tau} = E_b$. For $E < E_b$ (or $\nu < \nu_b$), the electrons do not lose a significant fraction of their energy and therefore the spectrum is the same as the injection spectrum. For $E > E_b$ (or $\nu > \nu_b$), the particles have lifetimes smaller than t and we only observe those produced during the previous synchrotron lifetime τ_b of the particles of energy E, that is $\tau_b \propto 1/E$. Therefore, the spectrum of the electrons is one power of E steeper with respect to the injection one, $N(E) \propto E^{-(\delta+1)}$. This characteristic energy E_b is called "break energy" (or "break frequency" for ν_b).

AGN are galaxies that are characterized by accretion onto their central supermassive black hole (SMBH) that is able to power emission generally across the whole electromagnetic spectrum. Thanks to this accretion, in some cases there can be relativistic jets that are launched from the central regions: these are characterized by synchrotron emission in presence of magnetic fields. Moreover, there is also radio emission from AGN host galaxy driven by star formation activity. These sources have dimensions that range from a few kpc to ∼ Mpc, well beyond the host galaxy. Part of the radio emission related to the AGN is observed in the form of radio "lobes", extended regions of emission diametrically opposed with respect to and quite distant from the compact radio source. Narrow jets originating in the central compact source extend out to the lobes and are the conduits by which energy is carried from an active region deep in the core of the central source to the lobes.

Depending on their radio morphology, radio-loud AGN (RLAGN) have been divided into two main categories by Fanaroff and Riley (1974): center-brightened "FRI" radio galaxies, that have initially relativistic jets that decelerate on kpc scales, and edge-brightened "FRII" radio galaxies, that are thought to have jets that remain relativistic throughout, terminating in a hotspot which is a site of particles acceleration that are then "stored" into the lobes (see Hardcastle and Croston, 2020, and references within).

Cluster radio galaxies (Fig. 1.4) differ from the field ones because of the interaction of jets and lobes of the central sources with the ICM due to their motion, that leads to different morphologies, from wide-angle (WAT), narrow-angle (NAT), to head-tail radio sources (Johnston-Hollitt et al., 2015, Miley, 1980).

As lower-frequency radio observations have become increasingly sensitive, it has become clear that another common feature of cluster centre radio source is the presence of low surface brightness extended lobes permeating a larger volume that the currently active source, and likely to indicate previous episodes of activity (de Gasperin et al., 2012).

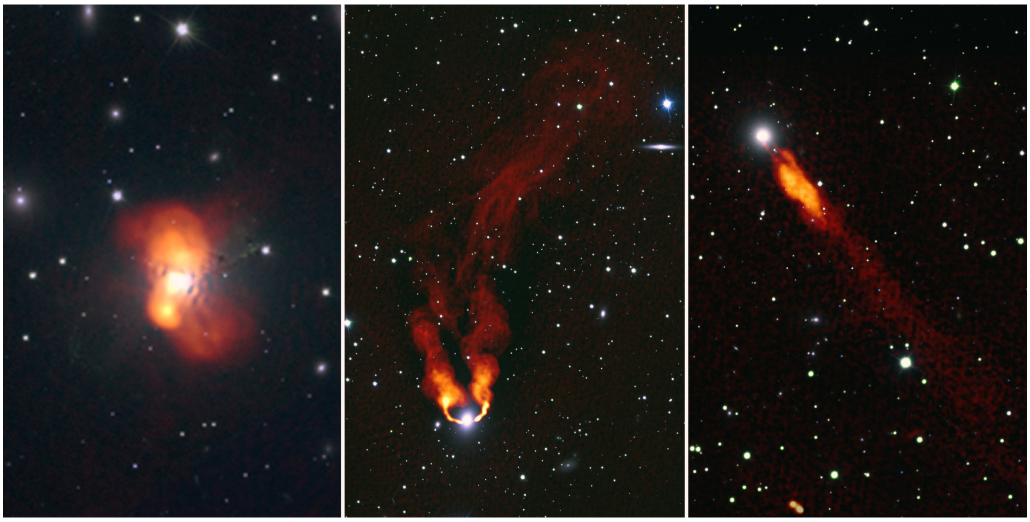

Figure 1.4: Left: NGC 1275, at the core of the cluster, is seen in new detail, including a newly-revealed wealth of complex, filamentary structure in its radio lobes. Center: NGC 1265 shows the effects of its motion through the tenuous material between the galaxies; its radio jets are bent backward by that interaction, then merge into a single, broad tail; the tail then is further bent, possibly by motions within the intergalactic material. Right: the jets of IC 310 are bent backward, similarly to NGC 1265, but appear closer because of the viewing angle from Earth; that angle also allows astronomers to directly observe energetic gamma rays generated near the supermassive black hole at the galaxy's core (Gendron-Marsolais et al., 2020).

Radio observations have shown that the ICM can also host a non-thermal component of cosmic rays (CR) which is not directly associated with the cluster radio galaxies (e.g. Willson, 1970). These GeV CR electrons (with Lorentz factors of $\gamma > 10^3$) emit synchrotron radiation in the presence of $\sim \mu$G ICM magnetic fields. From Eq. 1.1.25, for these kind of electrons, the typical synchrotron lifetime is $\tau \leq 10^8$ yr. For the diffusion, we can use the Bohm approximation for which we can write the diffusion length $l_d = \sqrt{D(E)\tau}$, where D is the diffusion coefficient $D(E) \propto E/B$, with E being the energy of the particle. Using this assumption, the typical diffusion length-scale for a GeV electron in the ICM is of the order of 10 pc. Plasma motions can increase the distance over which GeV electrons travel, but this distance is still expected to remain well below a Mpc.

This means that these Mpc-scale diffuse radio source cannot trace CR electrons that are accelerated at a single location in the ICM. Instead, they need to be (re-)accelerated or produced "in-situ" (Jaffe, 1977).

During the last decade, significant progress has been made in the understanding of this non-thermal component, through observations, theoretical, and numerical work. There is now compelling evidence that ICM shock waves, and likely also turbulence, are able to (re-)accelerate particles to relativistic energies creating this non-thermal CR component of the ICM (Brüggen et al., 2012).

The presence of diffuse synchrotron emission also indicates the existence of large-scale ICM magnetic field with a strength of the order of 0.1-10 μG (Brüggen et al., 2012, Clarke et al., 2001). Cluster magnetic fields play an important role in particle acceleration processes; additionally, magnetic fields inhibit transport processes like heat conduction, spatial mixing of gas, and the propagation of cosmic rays (Pfrommer et al., 2017, Ruszkowski and Oh, 2010). However, the information about the properties of these fields have been obtained only from a limited number of clusters, so more details will be available in the following years.

1.2 Diffuse radio emission in galaxy clusters

In the past decades, an increasing number of cluster hosting diffuse radio emission has been found. The steep radio spectra of such emissions are power-law like ($S_\nu \propto \nu^{-\alpha}$), indicative of synchrotron emission and demonstrating the presence of relativistic particles and magnetic fields. To understand the origin of these diffuse structures it is then crucial to investigate (i) what are the properties of the magnetic field in the ICM and (ii) how particles are accelerated at relativistic energies in such environments.

In this Section, we will present a general view on the main techniques used to unveil the magnetic field properties within cluster environment and list of the main classes of diffuse radio emission structures.

1.2.1 Diffuse cluster radio sources classification

Diffuse cluster radio sources can be divided in three broad classes: radio halos (divided in giant radio halos and mini-halos), radio relics and revived AGN fossil plasma sources (phoenices an GReET). Here these types are presented following the classification from van Weeren et al. (2019). Given their importance for this thesis work, the radio relics are described more in detail in Section 1.3.

Radio halos

Radio halos are extended sources that roughly follow the ICM gas density spatial distribution. A general property of this class is that particle (re-)acceleration/production occurs throughout a significant volume of the cluster: this implies that these global sources should trace Fermi-II processes and/or secondary electrons.

Actually, a further division inside this class can be made, distinguishing between "giant radio halo" and "mini-halo" diffuse sources.

Giant radio halo Giant Mpc-size radio halos (Fig. 1.5) are mostly found in massive dynamically disturbed clusters (Cassano et al., 2010b, Giovannini et al., 1999), where they have generally a smooth and regular morphology with the radio emission approximately following the thermal ICM distribution. They have typical sizes of about 1-2 Mpc and their 1.4 GHz radio powers range between $\sim 10^{23} - 10^{26}$ W Hz^{-1}.

Most radio halos have integrated spectral indices in the range $-1.4 < \alpha < -1.1$ (Giovannini et al., 2009): however, the spectral information of most radio

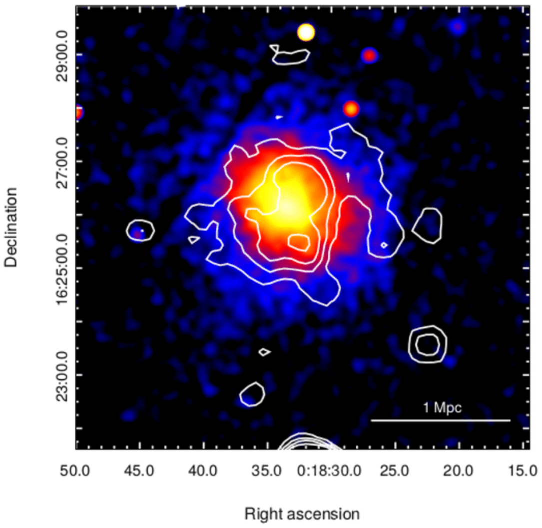

Figure 1.5: Radio emission from the giant radio halo at the center of MACS J0018.5+1626 (CL0016+26), shown in contours, superposed on the X-ray image obtained by Chandra (colour). The HPBW is 40", the noise level is 0.05 mJy per beam, and the shown contour levels are 0.3, 0.5, 0.7, 1 mJy beam^{-1} (Giovannini et al., 2020).

halos is based on measurements at just two frequencies, so there is a lack of information about the spetrum of these sources (van Weeren et al., 2019).

Some halos have been found to have a $\alpha \gtrsim 1.6$ and they have been called ultra-steep spectrum radio halos (USSRH). The existence of this USSRH is expected if the integrated spectra of radio halos include a cutoff: it is expected that only the most luminous radio halos, corresponding to the most energetic merger events, have cutoff frequencies of $\gtrsim 1$ GHz. In the turbulent re-acceleration model, the location of the break frequency ν_b approximately scales as $\nu_b \propto M^{4/3}$ (Cassano et al., 2010a), where M is the mass of the cluster: because of this scaling, it is expected that more USSRH radio halos, corresponding to less energetic merger events, can be uncovered with sensitive observations at low frequencies.

Radio halos are found to be generally unpolarized. This is likely caused by the limited angular resolution of current observations, resulting in beam depolarization. Even at high-angular resolution, magnetic field reversals and resulting Faraday rotation will reduce the amount of observed polarized flux. From models of radio halo polarization signal at 1.4 GHz (Govoni et al., 2013) the radio halos should be intrinsically polarized, with a fractional polarization at the cluster centers of about 15-35% and increasing with radial distance.

Mini-halos Radio mini-halos have sizes of $\sim 100-500$ kpc and are found in relaxed cool core clusters, with the radio emission surrounding the central loud BCG (Fig. 1.6). The sizes of mini-halos are comparable to that of the central cluster cooling regions. They have 1.4 GHz radio powers in the range of $10^{23} - 10^{25}$ W Hz^{-1}. Although smaller than radio halos, radio mini-halos also require in-situ acceleration given the short lifetime of synchrotron emitting electrons. The radio emission from mini-halos does therefore not directly originate from the central AGN, unlike the radio lobes that coincide with X-ray cavities in the ICM: nevertheless, the separa-

tion between AGN lobes and mini-halos can be difficult.
Unlike giant radio halos, where the turbulence is induced by major cluster mergers, mini-halos would trace turbulence in the cluster cores generated by the gas sloshing (ZuHone et al., 2013, 2015). The central AGN is a likely candidate for the source of the fossil electrons that are re-accelerated. The confinement of mini-halos by cold fronts (Mazzotta and Giacintucci, 2008) supports a scenario where turbulence induced by gas sloshing motions re-accelerates particles.
Spectral indices of radio mini-halos are similar to giant radio halos, and investigate on mini-halos spectral index would provide also information on the origin of CR electrons, allowing to discriminate between turbulent re-acceleration and secondary models (van Weeren et al., 2019). If the electrons are re-accelerated by MHD turbulence, the integrated spectra of mini-halos should display a spectral break caused by a cut-off in the electron energy distribution. For example, in Biava et al. (2021) they found that for the mini-halo in RXJ1720.1 also hadronic origin may provide a valid interpretation, not only the re-acceleration of seeds electrons.
Other important studies can be made regarding the possible relation between mini-halos and giant halos in clusters. For example, cluster merger events could transport CR electrons from cluster cores to larger-scales where they are re-accelerated again (Brunetti and Jones, 2014). This could lead to "intermediate" cases where mini-halos could evolve into giant halos and vice versa. Despite some observations support this scenario (Bonafede et al., 2014b, Venturi et al., 2017), it is not clear yet what is the transition mechanism between radio mini-halo and subsequent turbulent re-acceleration so more work is still required.

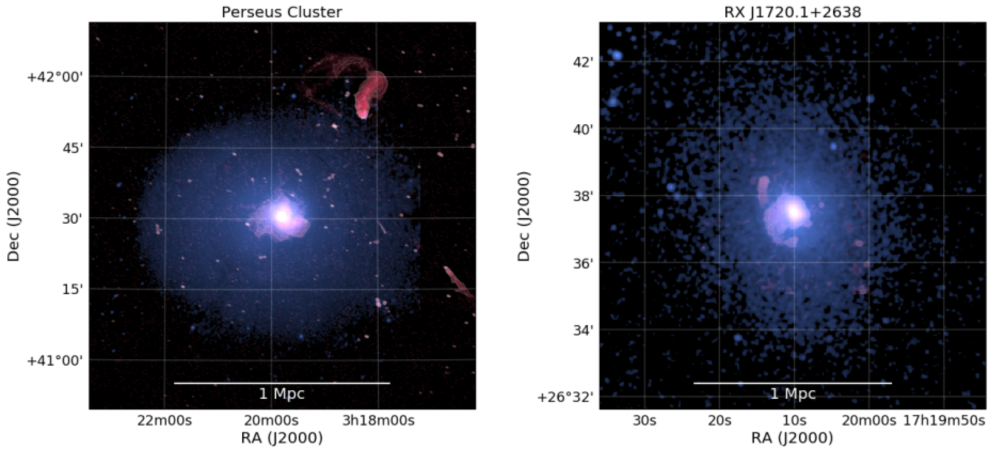

Figure 1.6: Examples of clusters hosting radio mini-halos, see also Figure 12. The radio emission is shown in red and the X- ray emission in blue. Perseus cluster: VLA 230–470 MHz and XMM-Newton 0.4–1.3 keV (Gendron-Marsolais et al., 2017). RX J1720.1+2638: GMRT 617 MHz and Chandra 0.5–2.0 keV (Andrade-Santos et al., 2017, Giacintucci et al., 2014).

Revived AGN fossil plasma sources

The study of mildly relativistic AGN fossil plasma throughout clusters is an important topic since, as discussed, old populations of relativistic electrons have been invoked as seed particles for the formation of radio halos and radio relics. They also retrace past AGN activity and constitute a source of non-thermal pressure in the ICM.

Radio phoenices and revived fossil plasma The currently favored scenario is that phoenices trace old radio plasma from past episodes of AGN activity. When a shock compresses this old plasma, the resulting increase in the momentum of the relativistic electrons and the magnetic field strength can produce a source characterized by a steep and curved radio spectrum (Enßlin and Gopal-Krishna, 2001). Simulations also predict that these sources should often have complex morphologies (Enßlin and Brüggen, 2002). Compared to cluster radio shocks (Section 1.3), revived fossil plasma sources and phoenices are on average found at smaller cluster centric distances, have smaller sizes ($\lesssim 300 - 400$ kpc) and have lower radio powers. The elongated and filamentary morphologies are the most common. The fact that some of these objects are found in cool core clusters, unlike radio relics, indicates that major merger events are not required for their formation.
These sources have integrated spectra that are typically steeper than 1.5, and in many cases show high-frequency spectral steepening; in general, the spectral index distribution across these sources is irregular without clear common trends.
Polarized emission from revived fossil plasma sources and phoenices has also been detected but the polarization fractions are generally lower than for relics.

Gently re-energized tail (GReET) In Abell 1033, and later possibly also in other tails of radio galaxies in GCs, a possible new mechanism to energize old radio plasma has been found. This process of re-energization is so gentle that it barely balances the radiative losses of CR, with a particle acceleration time-scale comparable to the radiative loss time-scale of the electrons emitting at < 100 MHz. A proposed physical explanation for the re-energization mechanism is that Rayleigh-Taylor and Kelvin-Helmholtz instabilities in the tails generate turbulent waves that re-accelerate electrons via Fermi-II mechanisms.
If this process is common also in other tails of GCs radio galaxies, then electrons released by radio galaxies in the ICM would live above 0.5 Gyr and they would be able to accumulate in larger quantities and with higher energies. This could produce a seed population of energetic particles of merger-induced re-acceleration mechanisms, such as turbulence and shocks, that were proposed to explain cluster-scale radio sources.
However, because very few examples of GReETs are known, the precise nature of these sources remains to be confirmed.

1.2.2 Magnetic fields in galaxy clusters

Magnetic fields permeate galaxy clusters and the intergalactic medium (IGM) on Mpc-scales. These fields play key roles in particle acceleration and on the process of large scale structure formation, having effects on turbulence, cloud collapse, large-scale motions, heat and momentum transport, convection, viscous dissipation. In particular, cluster magnetic fields inhibit transport processes like heat conduction, spatial mixing of gas and propagation of CR (van Weeren et al., 2019).

The origin of these fields remains largely uncertain. A commonly accepted hypothesis is that they result from the amplification of much weaker pre-existing seed fields via shock/compression and/or turbulence/dynamo amplification during merger events and structure formation, and different magnetic field scales can survive these processes as the result of turbulent motions (Donnert et al., 2018, Kahniashvili et al., 2013). The origin of seed fields is unknown. They could be either primordial, e.g. generated in the early Universe prior to recombination, or produced locally at later epochs of the Universe, in early stars and/or (proto)galaxies, and then injected in the interstellar and intergalactic medium (Carretti et al., 2022, Rees, 2006).
Magnetic fields are difficult to measure. Observations show that cluster fields are at the μG level, with values up to tens of μG at the center of cool core clusters, while merging clusters are characterized by intensities of a few μG (Vacca et al., 2018). Cosmological simulations of clusters predict μG-level magnetic field strengths in the cluster centers and a decrease of the magnetic field strength with radius in the outer regions (Dolag et al., 1999, 2001, 2002, Vazza et al., 2014, 2018).

Equipartition magnetic fields derived from the synchrotron emission

From the synchrotron emissivity, it is not possible to derive unambiguously the magnetic field properties: if we look at Eq. 1.1.21, we see that in order to obtain the magnetic field from the average emitted power we need also to know γ. The usual way to estimate the magnetic field strength in a radio source is to minimize its total energy content U_{tot}, assuming that the energies in CRs and magnetic fields in the radio emitting regions are the same (Govoni and Feretti, 2004). The total energy of a synchrotron source is due to the energy in relativistic particles (U_{el} in electrons and U_p in protons) plus the energy in magnetic fields (U_B):

$$U_{tot} = U_{el} + U_p + U_B. \tag{1.2.1}$$

The magnetic field energy contained in the source volume V is given by

$$U_B = \frac{B^2}{8\pi}\Phi V \tag{1.2.2}$$

where Φ is the fraction of the source volume occupied by the magnetic field (filling factor). The electron total energy in the range $\epsilon_1 - \epsilon_2$, for an electron energy distribution $N(\epsilon) = N_0\epsilon^{-\delta}$,

$$U_{el} = V \times \int_{\epsilon_1}^{\epsilon_2} N(\epsilon)\epsilon \, d\epsilon = V\, N_0 \int_{\epsilon_1}^{\epsilon_2} \epsilon^{-\delta+1}\, d\epsilon \tag{1.2.3}$$

can be expressed as a function of the synchrotron luminosity L_{syn}

$$L_{syn} = V \times \int_{\epsilon_1}^{\epsilon_2} (-\frac{d\epsilon}{dt}) N(\epsilon)\, d\epsilon = c_2(B\sin\theta)^2 V N_0 \int_{\epsilon_1}^{\epsilon_2} \epsilon^{-\delta+2}\, d\epsilon \tag{1.2.4}$$

by eliminating VN_0 and by writing ϵ_1 and ϵ_2 in terms of ν_1 and ν_2 ($\nu_c = c_1(B\sin\theta)\epsilon^2$):

$$U_{el} = c_2^{-1} c_1^{1/2} \tilde{C}(\alpha, \nu_1, \nu_2) L_{syn} B^{-3/2} = c_{12}(\alpha, \nu_1, \nu_2) L_{syn} B^{-3/2} \tag{1.2.5}$$

where $\sin\alpha$ has been taken equal to 1 and

$$\tilde{C}(\alpha, \nu_1, \nu_2) = \left(\frac{2\alpha - 2}{2\alpha - 1}\right) \frac{\nu_1^{(1-2\alpha)/2} - \nu_2^{(1-2\alpha)/2}}{\nu_1^{(1-\alpha)} - \nu_2^{(1-\alpha)}}. \tag{1.2.6}$$

The energy contained in the heavy particles U_p can be related to U_{el} assuming:

$$U_p = kU_{el} \tag{1.2.7}$$

where k depends on the nature of the plasma, and is generally the most uncertain term related to this assumption.
Finally, the total energy is obtained as a function of the magnetic field:

$$U_{tot} = (1 + k) c_{12} L_{syn} B^{-3/2} + \frac{B^2}{8\pi} \Phi V. \tag{1.2.8}$$

In order to obtain an estimate for the magnetic fields, it is necessary to make some assumptions about how the energy is distributed between the fields and the particles. The condition of minimum energy is obtained when the contributions of the magnetic field and the relativistic particles are approximately equal:

$$U_B = \frac{3}{4}(1 + k) U_{el}. \tag{1.2.9}$$

For this reason the minimum energy is known as "equipartition" value:

$$U_{tot}(min) = \frac{7}{4}(1 + k) U_{el} = \frac{7}{3} U_B. \tag{1.2.10}$$

The magnetic field for which the total energy content is minimum is:

$$B_{eq} = (6\pi(1 + k) c_{12} L_{syn} \Phi^{-1} V^{-1})^{2/7}. \tag{1.2.11}$$

The total minimum energy is then:

$$U_{tot}(min) = c_{13} \left(\frac{3}{4\pi}\right)^{3/7} (1 + k)^{4/7} \Phi^{3/7} V^{3/7} L_{syn}^{4/7}, \tag{1.2.12}$$

where $c_{13} = 0.921 c_{12}^{4/7}$, and the total minimum energy density is:

$$u_{min} = \frac{U_{tot}(min)}{V\Phi} = c_{13} \left(\frac{3}{4\pi}\right)^{3/7} (1 + k)^{4/7} \Phi^{-4/7} V^{-4/7} L_{syn}^{4/7}. \tag{1.2.13}$$

In terms of observed quantities, including the K-correction, assuming $\Phi = 1$ and expressing the parameters in commonly used units, we can write:

$$u_{min}\left[\frac{erg}{cm^3}\right] = \xi(\alpha, \nu_1, \nu_2)(1+k)^{4/7} (\nu_{0[MHz]})^{4\alpha/7} (1+z)^{(12+4\alpha)/7} \times (I_{0\left[\frac{mJy}{arcsec^2}\right]})^{4/7} (d_{[kpc]})^{-4/7}, \tag{1.2.14}$$

where z is the source redshift, I_0 is the source brightness at the frequency ν_0, d is the source depth.
The equipartition magnetic field is then obtained as:

$$B_{eq} = \left(\frac{24\pi}{7} u_{min}\right)^{1/2}. \tag{1.2.15}$$

Equipartition values for GC are usually computed assuming a constant $k = 0$ or $k = 1$. In the Coma cluster, equipartition field strength has a value of $\simeq 4$ μG (Beck and Krause, 2005), not too far from that derived from Faraday rotation data (Bonafede et al., 2010). Another example is the ICM magnetic field found with the equipartition assumption in MACS J0717.5 +3745 by Bonafede et al. (2009), which is ~ 1.2 μG in agreement with other values found in the literature.

Magnetic fields derived from Inverse Compton emission

When the synchrotron radio and IC X-ray emission are produced by the same population of relativistic electrons, the total synchrotron and IC luminosities are related (Govoni and Feretti, 2004). The IC emissivity is proportional to the energy density in the radiation field, $\mathrm{U_{rad}}$ (Eq. 1.1.11), which for the cosmological blackbody radiation is $\sim 5\times10^{-13}(1+z)^4\,\mathrm{erg\,cm^{-3}}$, whereas the synchrotron emissivity is proportional to the energy density in the magnetic field, $\mathrm{U_B} = \mathrm{B}^2/8\pi$ (Eq. 1.1.21). This leads to a simple proportionality between synchrotron and IC luminosities

$$\frac{L_{syn}}{L_{IC}} \propto \frac{\mathrm{U_B}}{\mathrm{U_{rad}}}. \tag{1.2.16}$$

CR electrons present in the ICM should scatter photons from the CMB, creating a hard power-law of X-ray emission on top of the thermal bremsstrahlung from the ICM (Rephaeli, 1979, Rephaeli et al., 1994, Sarazin and Kempner, 2000). However, there is no conclusive evidence yet for this IC emission from the diffuse CR component of the ICM: the difficulty associated with the detection of IC emission is related to the requirement of accurately modeling the contributions of the instrumental and astronomical backgrounds.
Recently, Adam et al. (2021) modelled the γ-ray emission from the Coma cluster, detected with Fermi-Large Area Telescope (Fermi-LAT), assuming that the γ-ray emission arises from hadronic interactions between CR protons and the thermal gas. They found that the energy stored in the CR protons is about 1.5% of the thermal energy of the Coma cluster, with a slope of the energy distribution of 2.8, larger than the one usually assumed following DSA.
Secondary CR electrons are also expected from hadronic interactions, and they could serve as seeds for the turbulent re-acceleration. In this framework, we expect to have future updates thanks to instruments like the Cherenkov Telescope Array (CTA).
Following Petrosian (2001), the monochromatic IC X-ray and synchrotron radio flux ratio (R_{obs}) can be written as $R_{obs} \equiv \frac{f_{IC}(kT)}{f_{syn}(\nu)}$

$$R_{obs} = 1.86\times10^{-8}\left(\frac{\mathrm{photons}}{\mathrm{cm^2\,s\,keV\,Jy}}\right)\times\left(\frac{kT}{20keV}\right)^{-\Gamma}\left(\frac{\nu}{GHz}\right)^{\Gamma-1}\left(\frac{\mathrm{T_{CMB}}}{2.8\mathrm{K}}\right)^{\Gamma+2}\left(\frac{B}{\mu\mathrm{G}}\right)^{-\Gamma}c(\delta), \tag{1.2.17}$$

where $\Gamma = (\delta + 1)/2$, δ is the power-law slope of the electron energy distribution $N(E) \propto E^{-\delta}$, $f_{IC}(kT)$ is the IC flux density at energy kT, $f_{syn}(\nu)$ is the synchrotron flux density at frequency ν, $\mathrm{T_{CMB}}$ is the CMB temperature at the cluster redshift and c(δ) is a normalization factor that is a function of δ.
With Equation 1.2.17 and some approximations, the expression for the magnetic field strength becomes

$$\begin{aligned} B &= \left(\frac{20\mathrm{keV}}{kT}\right)\left(\frac{\nu}{\mathrm{GHz}}\right)^{(\delta-1)/(\delta+1)} e^{\frac{2.84(\delta-r)}{\delta+1}}\,\mu\mathrm{G}, \\ r &\equiv 0.7\ln\left[\frac{R_{obs}(kT,\nu)}{1.11\times10^{-8}}\right]. \end{aligned} \tag{1.2.18}$$

By deriving upper limits on the IC X-ray emission and combining them with radio flux density measurements, lower limits on the global ICM magnetic field strength can be computed (e.g. Locatelli et al., 2020, where using this technique a lower limit on $B > 0.4$ μG was set for a new radio relic discovered around the GC Abell 2249). For radio halos (see 1.2.1), it is generally challenging to obtain stringent lower limits: the reason is that radio halos are typically faint. In addition, the IC emission is co-spatial with the thermal ICM, making it harder to separate the components. Furthermore, bright radio galaxies located in the cluster center can also produce non-thermal X-ray emission. The lower limits that have been computed for radio halo hosting clusters range around 0.1-0.5 μG (van Weeren et al., 2019, and references within).

Faraday rotation effect

The techniques that we have just introduced present some drawbacks. For what concerns the equipartition, we need too much assumptions in order to obtain the magnetic field (the minimum total energy content, the volume of the source, k), while for IC emission the difficulties are related to the limitations of present X-ray observations in the hard X-ray domain and to the problem of distinguishing between the non-thermal and the thermal X-ray emission. When the IC X-ray emission is not detected from a radio emitting region, only lower limits to the magnetic field can be derived.
The most promising technique to derive a more detailed view of the magnetic fields in clusters is via the analysis of the Faraday rotation of radio sources located inside or behind the cluster (Clarke, 2004, Govoni and Feretti, 2004).

The Faraday rotation effect appears during the propagation of linearly polarized radiation through a magnetized plasma: due to birefringence of the magneto-ionic medium, the polarization angle of linearly polarized radiation that propagates through the plasma is rotated as a function of frequency. Faraday rotation changes the intrinsic polarization angle (χ_0). The Faraday depth (ϕ) is related to the properties of the plasma that causes the rotation (Brentjens and de Bruyn, 2005, Burn, 1966)

$$\phi(\mathbf{r}) = 0.81\int_{source}^{observer} n_e\,\mathbf{B}\cdot d\mathbf{r}\quad \mathrm{rad\,m^{-2}}, \tag{1.2.19}$$

where n_e is the electron density in cm^{-3}, $\mathbf{B}$ the magnetic field in units of μG, and $d\mathbf{r}$ is an infinitesimal path length along the line of sight in units of parsec.
The rotation measure (RM) is defined as

$$RM = \frac{d\chi(\lambda^2)}{d\lambda^2}, \tag{1.2.20}$$

where λ is the observed wavelength.
The Faraday depth equals the RM at all wavelengths if there is only one source along the line of sight, which in addition has no internal Faraday rotation

$$\chi(\lambda^2) = \chi_0 + \phi\lambda^2. \tag{1.2.21}$$

From RM measurements, the strength and structure of cluster magnetic fields can be constrained by semi-analytical approaches, numerical techniques or RM synthesis (Brentjens and de Bruyn, 2005), which will be the technique used in this thesis in order to perform the polarimetric analysis of the relics emission. Because of its importance in this work, it will be described in detail in Ch. 2.
Information about the magnetic field in individual clusters through RM studies have been obtained so far for about 30 objects, including both merging and relaxed clusters. The observed data are generally consistent with a turbulent field following a Kolmogorov power-law spectrum ($\propto k^{-11/3}$ in 3D). From energy considerations it is inferred that the magnetic field profile scales with the gas density n_e as $B \propto n_e^{\eta}$. The value of this index η reflects the magnetic field formation and amplification: it is expected a value of $\eta = 2/3$ in the case of adiabatic compression during a spherical collapse due to gravity, while if the energy in the magnetic field scales as the energy in the thermal plasma a value of $\eta = 1/2$ is expected.

From the analysis of the fractional polarization of radio sources in a sample of

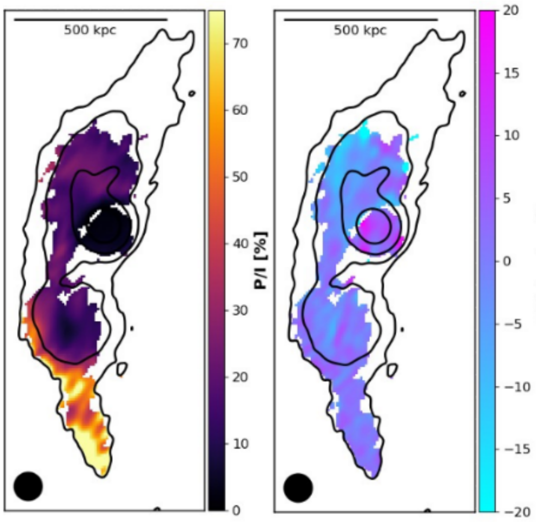

Figure 1.7: Fractional polarization and RM images of the E radio relic in the C-configuration observation in Abell 2345. The $6\sigma_{QU}$ detection threshold was imposed in polarization and only pixels above this threshold are shown. Black contours show the total intensity image used to compute the fractional polarization, start from 3 times the root mean square (RMS) noise and are spaced by a factor of four (Stuardi et al., 2021).

X-ray luminous clusters from the NRAO VLA Sky Survey (NVSS), a clear trend of the fractional polarization increasing with the distance from the cluster center has been derived (Bonafede et al., 2011, Osinga et al., 2022). The low fractional polarization in sources closer to the cluster center is interpreted as the result of higher beam depolarization, occurring in the ICM because of fluctuations within the observing beam and higher magnetic field and gas densities in these regions. Results are consistent with fields of a few μG.
In Osinga et al. (2022), the average central magnetic field strength is between 5-10 μG with a $\eta = 0.5$ fixed. For Abell 194, Govoni et al. (2017) found instead a central magnetic field strength of $(1.5{\pm}0.2)$ μG with a best-fit value of $\eta = 1.1{\pm}0.2$. Stuardi et al. (2021) found an average central magnetic field of (2.8 ± 0.1) μG in the double relic galaxy cluster Abell 2345 (Fig. 1.7) but a $\eta = 1$, larger than the value obtained in cosmological simulations (Vazza et al., 2018) and for the Coma cluster ($\eta = 0.5$ in Bonafede et al., 2010).

1.2.3 Particle acceleration mechanisms

There are several physical mechanisms to accelerate particles in the ICM and produce the synchrotron emitting CR electrons. Here a general overview of these processes is presented.

- *Diffusive shock acceleration* (DSA): In this Fermi-I like process, particles are accelerated at a shock with the acceleration taking place diffusively. To be accelerated, particles cross back and forward across the shock front as they scatter from magnetic field inhomogeneities in the shock down and upstream region. At each crossing, particles gain additional energy, forming a power-law energy distribution of CR. The synchrotron power related to the DSA model depends strongly on the Mach number M

  $$P_{sync} \propto \eta(M) \cdot M^3, \tag{1.2.22}$$

  where η is the shock acceleration efficiency.

- *Second order Fermi acceleration* (Fermi-II): This is a stochastic process where particles scatter from magnetic inhomogeneities, for example from magnetohydrodynamical (MHD) turbulence (Brunetti et al., 2001). Particles can either gain or loose energy when scattering, but when the motions are random the probability for a head-on collision, where energy is gained, is slightly larger. Because of its random nature, second order Fermi acceleration is an inefficient process.

- *Adiabatic compression*: A shock wave can adiabatically compress a bubble/lobe/cocoon of (old) relativistic radio plasma from an AGN. Due to compression, the CR electrons in the cocoon regain energy boosting the radio synchrotron emission.

- *Secondary models*: In these processes, CR electrons are produced as secondary particles (decay products). In the hadronic model, collisions between relativistic protons and the thermal ions produce secondary CR electrons. Since CR protons have a very long lifetime compared to CR electrons, they will accumulate over the lifetime of a cluster once they are accelerated. Possible mechanisms to produce CR protons are DSA, AGN activity and galactic outflows (supernovae, winds).

1.3 Radio relics

Radio relics are mostly found in the outskirts of galaxy clusters and are characterized by elongated shapes, with length of 0.5-2 Mpc, and strong polarization at GHz frequencies ($\gtrsim$ 20%, Enßlin et al., 1998). They seem to be produced during a cluster binary merger. In fact, in an idealized binary merger, "equatorial" shocks form first and move outwards in the equatorial plane. After the dark matter core passage, two "merger" shocks are launched in opposite directions along the merger axis (Fig. 1.8), which can explain the formation of cluster double radio relics in observed merging clusters. The radial distribution of observed radio shocks can be explained by the radial trend of dissipated kinetic energy in shocks, which increases with cluster centric distance up until half of the virial radius (Vazza et al., 2012).
The strength of a shock wave can be quantified by the so-called "Mach number"

$$M = \frac{v}{c_s}, \tag{1.3.1}$$

where v is the velocity of the shock and

$$c_s = \left(\frac{\partial p}{\partial \rho}\right)^{1/2} \tag{1.3.2}$$

is the sound speed.
If the radio relics are tracing shocks accelerated particles, these shock waves should coexist at the location of radio shocks.
From X-rays observations, the intensity of shock structure, quantified by the X-ray-derived Mach number M_X, can be estimated from the Rankine-Hugoniot jump conditions (Landau and Lifshit's, 1959). Assuming a ratio of specific heats as $\gamma = 5/3$, we have

$$\frac{T_2}{T_1} = \frac{5M_X^4 + 14M_X^2 - 3}{16M_X^2}, \tag{1.3.3}$$

$$\frac{\rho_2}{\rho_1} = \frac{4M_X^2}{M_X^2 + 3}, \tag{1.3.4}$$

where the subscripts 1 and 2 refer to the pre- and post- shock ICM density or temperature, respectively.
On the other hand, based on the assumption of simple DSA theory, the Mach number can be also estimated from the radio injection spectral index ($\alpha_{inj} = (\delta - 1)/2$, where $\delta = 2\frac{M^2+1}{M^2-1}$) via

$$M_{radio} = \sqrt{\frac{2\alpha_{inj} - 3}{2\alpha_{inj} + 1}}. \tag{1.3.5}$$

In principle, both X-rays and radio approaches are independent methods to characterize the shock strength, meaning shock strengths inferred from these different wavelength regimes should match each other, if underlying assumptions are correct. However, for a number of radio shocks has been found that $M_{radio} > M_X$. This discrepancy, if real, may point to problems in the DSA scenario for shocks in clusters. It is possible that the X-rays derived Mach numbers are somewhat underestimated due to unfavorable viewing angles and the complexity of the shock surface. In addition, the shock acceleration efficiency is thought to be a strong function of shock Mach number (Hoeft and Brüggen, 2007). Therefore, the CR-energy-weighted Mach number is expected to be higher than the kinetic-energy-weighted Mach number (Ha et al., 2018). Thus radio measured Mach numbers will be biased towards parts of the shock with the highest Mach numbers. Therefore, both Mach numbers characterise a part of the true shock dynamics.

Analyzing the properties of shocks associated with synthetic merging clusters in structure formation simulations, Ha et al. (2018) found that the CR production peak at $\sim$ Gyr after the core passage, with the shock-kinetic-energy-weighted Mach number $\langle M_s \rangle_\phi \simeq 2-3$ and the CR-flux-weighted Mach number $\langle M_s \rangle_{CR} \simeq 3-4$. The elongated shapes of these structures are expected for sources that trace shock waves in the cluster outskirts and are seen close to edge-on.

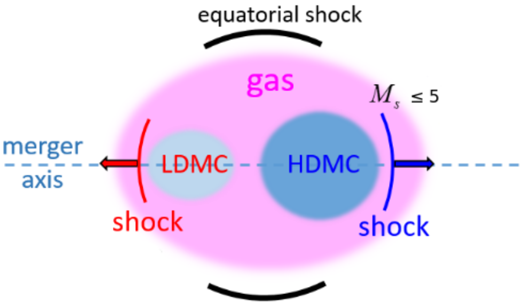

Figure 1.8: Schematic picture of an idealized binary cluster merger about 1 Gyr after core passage. Equatorial shocks expand outwards in the equatorial plane perpendicular to the merger axis, while merger shocks lunch in the opposite directions along the merger axis. Typically, the shock ahead of lighter DM core has the higher shock kinetic energy flux and becomes the brighter radio shock (van Weeren et al., 2019).

Deep high-resolution observations of large elongated radio shocks have also revealed a significant amount of filamentary structures (Fig. 1.11). The observed filaments could be substructures of a complex shock front, possibly highlighting the underlying distribution of Mach numbers and a range of electron acceleration efficiencies by shock acceleration. Conversely, they can reflect a pattern of fluctuations in the magnetic field strength. The MHD turbulence can also produce sheet-like large filaments (Rajpurohit et al., 2018, 2022, van Weeren et al., 2017).

The merger axis of relics hosting clusters are generally in or near the plane of the sky: this indicates that there are selection biases for finding cluster radio shocks based on the viewing angle, and so many radio relics with less favourable orientations are probably missing in current samples.

The integrated radio spectra of relics display power-law shapes with spectral indices ranging from about 1.0 to 1.5. Radio relics often show a clear spectral index gradient across their width: the region with the flattest spectral index is located on the side away from the cluster center, while there is a steepening of the spectral index towards the cluster center which is thought to be caused by synchrotron and IC losses in the downstream region (Fig. 1.9, van Weeren et al., 2016).

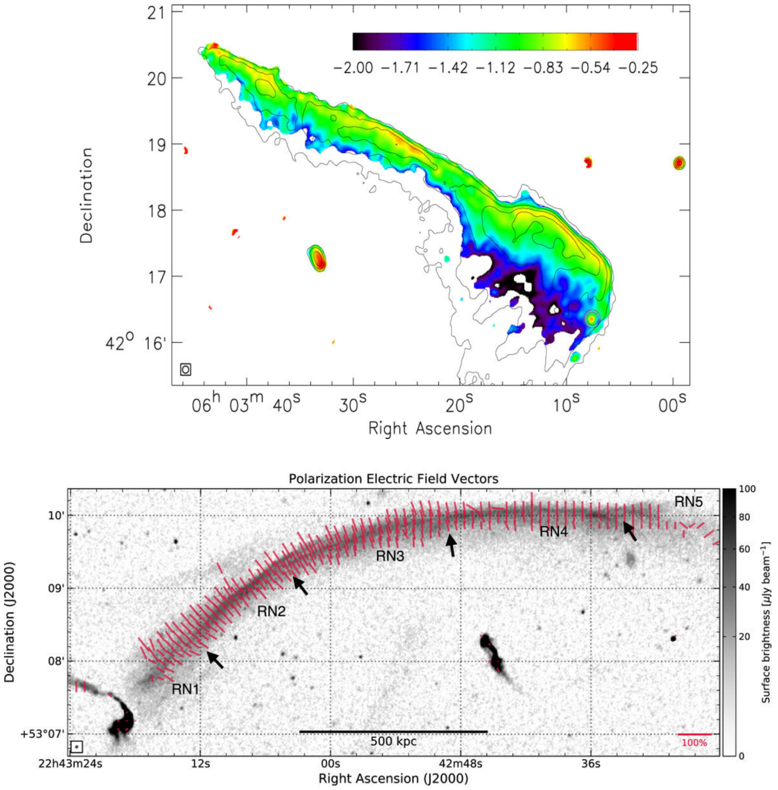

Figure 1.9: Top: spectral index map between 151 and 610 MHz at 6.5” resolution of the Toothbrush relic in the cluster RX J0603.3+421, one of the brightest radio relic sources known. Black contours are drawn at levels of [1,2,4,...]×1.25 mJy beam^{-1} and are from a 151 MHz image. Pixels with values below 4.5 σ_{rms} were blanked (van Weeren et al., 2016).
Bottom: high-resolution (2”.1 × 1”.8) Stokes I observation in the 1–2 GHz band with the polarization electric field vectors at 2”.7 resolution, corrected for Faraday rotation, displayed in red; the length of the vectors is proportional to the intrinsic polarization fraction (scale in the lower right corner) (Di Gennaro et al., 2021).

Radio relics are amongst the most polarized sources in the extragalactic sky: the polarization fractions can reach ∼ 60% in some cases and these polarization properties are expected if these sources trace edge-on shock waves (Enßlin et al., 1998). For large relics the intrinsic polarization angles, corrected for the effect of Faraday rotation, are found to be well aligned (Fig. 1.9, Di Gennaro et al., 2021). The polarization magnetic field vectors are oriented generally parallel to the shock front, as expected in presence of plasma compression (Brunetti and Jones, 2014).

Because of their shapes, locations, and spectral and polarimetric properties, radio relics are considered to trace particles accelerated at shocks. These shocks can be

generated by cluster merger activity or accretion flows from surrounding large-scale structures (Enßlin et al., 1998). Particle acceleration at shocks can be described according to DSA theory. Radio relics are special environments as they are unique laboratories for constraining the physics of particle acceleration at Mpc-scale weak shocks, given that for these sources the DSA shows some issues in order to explain the observed synchrotron emission from shock accelerated electrons.
First of all, the thermal electrons from the ICM do not have a sufficiently large gyroradius in order to interact with the magnetic field inhomogeneities in the shock down and upstream region and start to be accelerated. This is known as "injection problem" and has two possible solutions, that can both be valid at the same time.

- A possible solution is represented by the (recent) radio observations of streams of electrons connected to nearby radio galaxies, being accelerated by radio relics (Fig. 1.10, Bonafede et al., 2014a). In this case shocks producing radio relics are not accelerating electrons from the thermal pool, but can use these "fossil" electrons injected from radio galaxies with a Lorentz factor already of $\gamma \sim 10^2$ to accelerate them to $\gamma \geq 10^4$-10^5 via DSA. However, not for every relic this sort of "stream" has been observed and moreover this scenario is viable if the jets and lobes of radio galaxies are lepton-dominated (Vazza et al., 2016).

- Another possibility relies on the presence of some other mechanism produced in weak shocks which can pre-accelerate electrons and let DSA be activated later. An example is the so-called shock drift acceleration (SDA), where if a shock is weak (low Mach numbers) electrons can "surf" the shock surface and move (anti)parallel to the electric field induced by $\mathbf{E} = -\mathbf{V} \times \mathbf{B}$. Simulations have started showing (e.g. Guo and Giacalone, 2015) that this additional pre-acceleration stage is enough to increase the electrons gyroradius and let them enter the DSA regime.

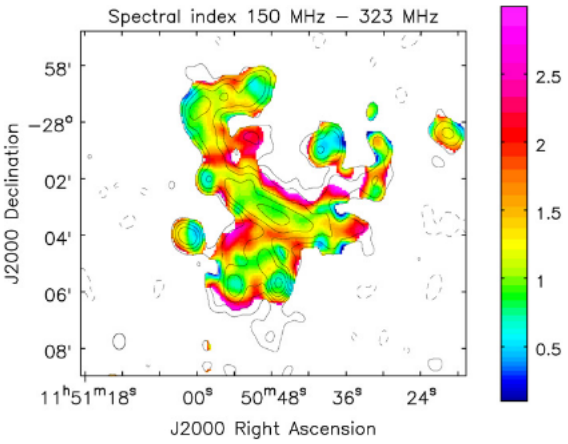

Figure 1.10: Spectral index and spectral index error image obtained considering the 150 and 323 MHz images (colors) for the extended emission detected NW of the NW relic in PLCKG287.0+32.9. The 150 MHz contours are overlaid (Bonafede et al., 2014a).

Second, given that thermal protons have sufficiently large energy (and so gyroradius), we expect them to be accelerated by the weak shocks that accelerate electrons.

These CR protons should then collide with the thermal particles of the ICM, given that from DSA their number should be much larger than CR electrons, and produce an hadronic cascade (Pfrommer et al., 2006): at the end of these processes, from the spontaneous decay of neutral pions π^0, a couple of γ-ray photons should be produced. While the radio emission in galaxy clusters (halos and relics) can also be explained by other "primary models" (Fermi-II and Fermi-I respectively), a detection of the γ-ray emission from the ICM would unambiguously unveil hadronic emission from cosmic ray protons. Unpredictably, this expected diffuse gamma-ray emission of hadronic origin has not been observed yet. It has been noted by Vazza and Brüggen (2014) and Vazza et al. (2015, 2016) that the expected gamma-ray emission from DSA shock acceleration at relics is in tension with gamma-ray upper limits for some clusters, that have been constrained by the Fermi telescope with $X_{CR} = \frac{E_{CR}}{E_g} \leq 1.5\%$ within the virial radius of GCs ($\leq$1-3 Mpc). This represents the energy ratio of CR protons with respect to the thermal gas energy.

The mystery of "missing" CR protons (from γ-rays) is exacerbated by the fact that instead we have evidence of plenty of cosmic ray electrons from radio observations. Moreover, we expect the radiative lifetime of protons to be much longer (over Gyrs) than the one of the electrons: this means that all the protons accelerated by the shocks during the cluster lifetime should still be in the cluster volume and emit γ-rays.

In order to explain the existence of CR electrons without CR protons different solutions have been proposed.

- Weak shocks almost do not accelerate CR protons at all, and DSA works with electrons only because they are "fossil" relativistic electrons already injected by radio galaxies and AGN. However, this solution can work only if jets and lobes from AGN and radiogalaxies are mostly lepton-dominated.

- Weak shocks almost do not accelerate CR protons at all, but they do accelerate CR electrons through some kind of "pre-acceleration" stage. In this scenario the obliquity angle (θ), defined as the angle between the upstream magnetic field ($\mathbf{B}_0$) and the shock normal ($\mathbf{v}_s$), has an important role in distinguishing between protons and electrons. When $\theta \geq 45$ protons are not scattered upstream, no being able to start DSA, while electrons can be pre-accelerated by SDA and can later undergo DSA acceleration. With recent cosmological simulations (Banfi et al., 2020), it was possible to show that in the very turbulent ICM magnetic field, shocks have an almost random distribution ($P(\theta) \propto \sin\theta$, Wittor et al., 2017). Most shocks are quasi-perpendicular and the injection of CR protons is suppressed, while the electron acceleration via SDA remains.

- In both cases, maybe our estimate of the Mach number is wrong, which will change the energetic because $\Phi_{CR} \propto \eta(M) \cdot M^3$, where Φ_{CR} is the cosmic rays flux and η the shock acceleration efficiency (Ryu et al., 2003).

Magnetic fields at radio relics

Similar to radio halos, measurements of IC X-rays emission can be used to determine magnetic field strength at the location of cluster radio shocks (see 1.3), but so far no

undisputed detections have been made. With deep X-rays observations, mostly from the XMM-Newton and Suzaku satellites, interesting lower limits on the magnetic field strength have been determined (van Weeren et al., 2019, and reference within), with a range of lower limits between 0.7-3 μG.
Another method to constrain the magnetic field strength at the location of cluster radio shocks is to use the source's width. Here the assumption is that the width is determined by the characteristic timescale of electron energy losses (up to $\sim 10^8$ yr for synchrotron and IC losses) and the shock downstream velocity. Using this method, values of either $\sim$1 or $\sim$5 μG were found for Sausage cluster (van Weeren et al., 2010). However, recent work by Rajpurohit et al. (2018) suggests that there are more factors affecting the downstream radio brightness profiles making the interpretation more complicated, for example, due to the presence of filamentary structures in the radio shock and a distribution of magnetic field strengths.

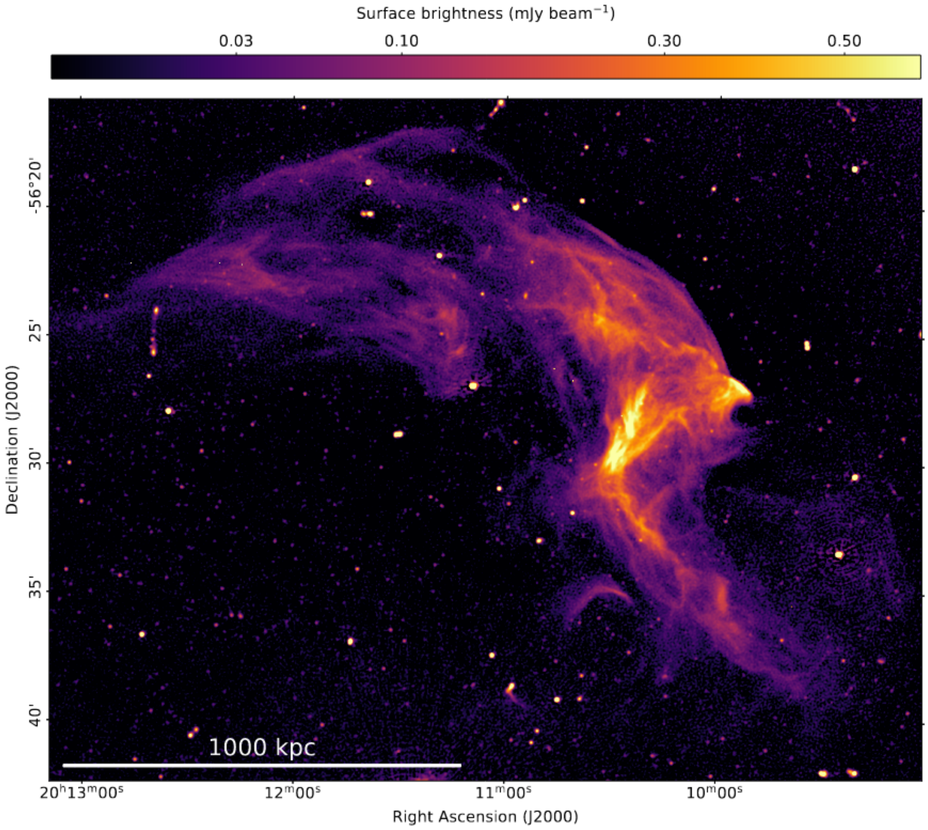

Figure 1.11: Radio emission from the northern radio relic in Abell 3667 where can be clearly seen the filamentary structure that characterize several relics. The image has a local RMS noise of 10 μJy beam^{-1} and a beam of 5" × 5". (de Gasperin et al., 2022).

Chapter 2

Polarization and Faraday rotation effect

In this Chapter we present the techniques used for this thesis work in order to study the polarized emission from the two relics hosted by the PSZ2 G096.88+24.18 cluster (Ch. 4), and constrain their magnetic fields. After a description of the polarization properties of synchrotron radiation, we discuss the basis of the RM synthesis technique (Sec. 2.4).
The concepts reported here represent an extension of the rotation measure work of Burn (1966) made by Brentjens and de Bruyn (2005).

2.1 Polarization

The synchrotron emission is linearly polarized. In the optically thin case, the degree of intrinsic linear polarization, for a homogeneous and isotropic distribution of relativistic electrons with a power-law spectrum $N(E)dE = N_0 E^{-\delta} dE$, is:

$$p_{int} = \frac{3\delta + 3}{3\delta + 7} \tag{2.1.1}$$

with the electric (polarization) vector perpendicular to the projection of the magnetic field onto the plane of the sky (Le Roux, 1961).
For typical values of the particle spectral index ($\delta \sim 2.5$, so $\alpha \sim 0.7$), the intrinsic polarization degree is about 70%, although, in practice, the observed polarization degree is often smaller due to several effects that will be described later.
The polarization of an electromagnetic wave is described in terms of the Stokes parameters I, Q, U, V, which are parameters of a reference system representing the orientation of the wave electric field. Each i-th antenna of an interferometer measures a voltage: for example, the electric field of the incoming monochromatic radiation is converted into a voltage V to be sampled

$$\begin{aligned} V_L^i &= V_L \sin(\omega t + \phi_L^i) \\ V_R^i &= V_R \sin(\omega t + \phi_R^i), \end{aligned} \tag{2.1.2}$$

with R,L being right and left circular polarization, respectively, ϕ the relative phase term, and ω the frequency of collected radiation.
Doing radio interferometry, the signals of two antennas, i and j, are cross-correlated. The Stokes parameters are defined as:

$$I = \frac{V_R^i V_R^j + V_L^i V_L^j}{2}, \qquad U = \frac{V_R^i V_L^j - V_L^i V_R^j}{2}$$
$$Q = \frac{V_R^i V_L^j + V_L^i V_R^j}{2}, \qquad V = \frac{V_R^i V_R^j - V_L^i V_L^j}{2}. \tag{2.1.3}$$

Following Burn (1966), we define the complex linear polarization P as

$$P = \|p\| I e^{2i\chi} = Q + iU, \quad \text{with} \quad |\mathrm{P}| = \sqrt{\mathrm{Q}^2 + \mathrm{U}^2}, \tag{2.1.4}$$

where $\chi = \frac{1}{2}\arctan\frac{U}{Q}$ is the observed polarization angle.

2.2 Faraday rotation effect

As we mentioned before in Section 1.2.2, due to the birefringence of the magneto-ionic medium, the polarization angle of linearly polarized radiation that propagates through a magnetized plasma is rotated as a function of frequency, as can be seen in Fig 2.1. This effect is called Faraday rotation.
A linearly polarized wave can be decomposed into opposite-handed circularly polarized components (Govoni and Feretti, 2004). The right-handed and left-handed circularly polarized waves propagate with different phase velocities within the magneto-ionic material: this effectively rotates the plane of polarization of the electromagnetic wave.
According to the dispersion relation, for a wave of angular frequency ω, the refractive index of a magnetized dielectric medium can take two possible values

$$n_{L,R} = \left(1 - \frac{\omega_p^2}{\omega^2 \pm \omega\Omega_e}\right)^{1/2}, \tag{2.2.1}$$

where $\omega_p = (\frac{4\pi n_e e^2}{m_e})^{1/2}$ is the plasma frequency, with e and m_e the electron charge and mass, respectively, and $\Omega_e = \frac{eB}{m_e c}$ is the cyclotron frequency. Different refractive indices mean different propagation velocities for the left- and the right-handed circularly polarized waves.
Therefore, after the transition across the medium, the two circular components are out of phase with those of the original radiation. The global effect is a change in the polarization angle of the linearly polarized radiation when crosses a magnetized plasma.
The radio frequencies dominate the values of ω_p and Ω_e obtained for typical magnetic fields ($B \simeq 1$ μG) and gas densities ($n_e \simeq 10^{-3}$ cm^{-3}) in the ICM. In the limit $\omega \gg \Omega_e$, Eq. 2.2.1 can be approximated as

$$n_{L,R} \approx 1 - \frac{1}{2}\frac{\omega_p^2}{(\omega^2 \pm \omega\Omega_e)}. \tag{2.2.2}$$

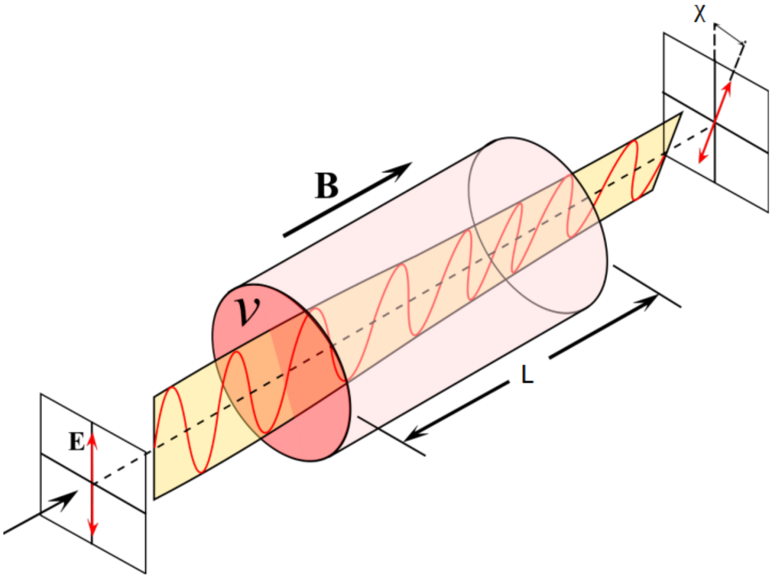

Figure 2.1: Scheme of how the Faraday rotation effect can cause variations in the polarization angle of linearly polarized radiation (Wikipedia, 2022)

Thus the difference in time of the two opposite handed waves to travel a path length dl results

$$\Delta t \approx \frac{\omega_p^2 \Omega_e dl}{c\omega^3} = \frac{4\pi e^3}{\omega^3 m_e^2 c^2} n_e B dl, \tag{2.2.3}$$

and the phase difference between the two signals $\Delta\psi = \omega\Delta t$. Therefore, travelling along a path length L, the intrinsic polarization angle χ_0 will be rotated by an angle $\Delta\chi = \frac{1}{2}\Delta\psi$, resulting

$$\chi(\lambda) = \chi_0 + \Delta\chi = \chi_0 + \frac{e^3\lambda^2}{2\pi m_e^2 c^4} \int_0^L n_e(l) B_{\parallel}(l)\, dl, \tag{2.2.4}$$

where $B_{\parallel}$ is the component of the magnetic field along the line of sight and λ the radiation wavelength.
Usually, $\chi(\lambda)$ is written in terms of the Faraday depth ϕ:

$$\chi(\lambda) = \chi_0 + \lambda^2\phi, \tag{2.2.5}$$

where ϕ can be written, in practical units, as seen in Eq. 1.2.19.
By convention, a positive Faraday depth implies a magnetic field pointing toward the observer. This Equation is valid only in the simplest possible scenario, where there is a single background source along the line of sight and with a Faraday rotation due to only a foreground magneto-ionic medium (Brentjens and de Bruyn, 2005).
We have previously discussed the differences between the Faraday depth and the RM (Section 1.2.2): throughout this thesis, we are only going to consider Faraday thin sources, therefore both terms (and their respective symbols, ϕ and RM) will be used interchangeably.

2.3 Depolarization mechanisms

In the simplest possible case, given Eq. 2.1.4, the complex polarized intensity of synchrotron radiation affected by Faraday rotation is

$$P_{obs}(\lambda^2) = P_{int} e^{2i(\chi_0 + \phi\lambda^2)} \tag{2.3.1}$$

where P_{int} is the intrinsic polarization of the synchrotron emission, χ_0 is the relative intrinsic polarization angle at the source of emission and RM quantifies the Faraday rotation caused by the foreground magneto-ionic medium.
In a radio source the observed polarization intensity, $P_{obs}(\lambda)$, can be significantly lower with respect to the intrinsic value, P_{int}. The Faraday rotation changes the polarization angle during the propagation of radiation but $|P|$ does not change. However, several intrinsic and instrumental effects can induce a depolarization of the observed radiation in different circumstances.
Depolarization towards longer wavelength can occur due to mixing of the emitting and rotating media, as well as from the finite spatial resolution of our observations (O'Sullivan et al., 2012). Here are presented the main depolarization mechanisms, following the discussions in Sokoloff et al. (1998) and Stuardi et al. (2022).

1. *Differential Faraday rotation*: This effect occurs when the emitting and rotating regions are co-spatial and are in the presence of a regular magnetic field. The polarization plane of the emission at the far side of the region undergoes a different amount of Faraday rotation compared to the polarized emission coming from the near side, causing depolarization when summed over the entire region.
   For a uniform slab, we have

   $$P_{obs} = P_{int} \frac{\sin \phi\lambda^2}{\phi\lambda^2} e^{2i(\chi_0 + \frac{1}{2}\phi\lambda^2)}. \tag{2.3.2}$$

   We note that depolarization increases at longer wavelengths.

2. *Internal Faraday dispersion*: This occurs when the emitting and rotating regions also contain a turbulent magnetic field. In this case, depolarization occurs because the plane of polarization experiences a random walk through the region. For identical distributions of all the constituents of the magneto-ionic medium along the line of sight, it can be described by

   $$P_{obs} = P_{int} e^{2i\chi_0} \left(\frac{1 - e^{2i\phi\lambda^2 - 2\zeta_{RM}^2\lambda^4}}{2\zeta_{RM}^2\lambda^4 - 2i\phi\lambda^2} \right) \tag{2.3.3}$$

   where ζ_{RM} is the internal Faraday dispersion of the medium.

3. *External Faraday dispersion/beam depolarization*: This occurs in a purely external non-emitting Faraday screen. In the case of turbulent magnetic fields, depolarization occurs when many turbulent cells are within the synthesized telescope beam. On the other hand, for a regular magnetic field, any variation

in the strength or direction of the field within the observing beam will lead to depolarization.
Both effects can be described by:

$$P_{obs} = P_{int} e^{-2\sigma_{RM}^2 \lambda^4} e^{2i(\chi_0 + \mathrm{RM}\lambda^2)}, \tag{2.3.4}$$

where σ_{RM} is the dispersion about the mean RM across the source on the sky.

4. *Bandwidth depolarization*: Occurs when a significant rotation of the polarization angle of the radiation is produced across the observing bandwidth.

2.4 RM synthesis

The RM synthesis technique allows to recover the value of Faraday depth, ϕ, and study the polarized emission from a source.
Once the value of ϕ is obtained, it is possible, following Eq. 1.2.19, to recover information about the magnetic field along the line of sight as well as the electrons distribution of the medium responsible for the Faraday rotation.
The simplest case for the Faraday rotation is the one with a single source along the line of sight and with an external rotating medium: in this case, the observed polarization vector can be written as Eq. 2.3.1, and the corresponding observed polarization angle is given by Eq. 1.2.21.
In principle, RM could be determined by plotting the observed polarization angle as a function of the square of the observing wavelength, and performing a least-squares fit to the data. There are three potential problems with this approach.

- The observed polarization angle is only known modulo π radians; thus, with measurements in only a few wavelength bands, the RM fit is often arbitrary. This is commonly referred to as “nπ ambiguity”.

- Different polarized sources can be present in a single line of sight: the signal from these different regions mixes and makes a linear fit inappropriate, so that the polarization angle is no longer proportional to λ^2.

- Faint sources with high rotation measure will be undetectable in individual channels due to low signal-to-noise ratio, and will remain undetectable even after integrating all channels due to bandwidth depolarization.

In order to solve these problems the RM synthesis has been developed by Brentjens and de Bruyn (2005), who extended the work of Burn (1966) to the case of limited sampling of λ^2 space.
Given the observed polarization vector $P(\lambda^2)$, they found that this can be written as a function of $F(\phi)$, which is the Faraday dispersion function and describes the intrinsic polarized flux as a function of the Faraday depth

$$P(\lambda^2) = \int_{-\infty}^{+\infty} F(\phi) e^{2i\phi\lambda^2} \, d\phi. \tag{2.4.1}$$

This expression means that we have a Fourier transform relation between observed ($P(\lambda^2)$) and intrinsic ($F(\phi)$) quantities. The equation can be inverted in order to express the instrinsic polarization in terms of observable quantities:

$$F(\phi) = \int_{-\infty}^{+\infty} P(\lambda^2) e^{-2i\phi\lambda^2}\, d\lambda^2. \tag{2.4.2}$$

However, we do not observe at wavelengths where $\lambda^2 < 0$, nor we observe at all values of $\lambda^2 > 0$.

These issues are solved by Brentjens and de Bruyn (2005) introducing a weight function (also known as window function), $W(\lambda^2)$, which is non-zero only at values of λ^2 which are sampled by the telescope. With this implementation, we can rewrite Eqns. 2.4.1 and 2.4.2 to express the observed polarized flux density as

$$\tilde{P}(\lambda^2) = W(\lambda^2)P(\lambda^2) = W(\lambda^2)\int_{-\infty}^{+\infty} F(\phi) e^{2i\phi(\lambda^2-\lambda_0^2)}\, d\phi \tag{2.4.3}$$

and the "reconstructed" Faraday dispersion function, also known as Faraday spectrum, as

$$\tilde{F}(\phi) = F(\phi) \circledast R(\phi) = K \int_{-\infty}^{+\infty} \tilde{P}(\lambda^2) e^{-2i\phi(\lambda^2-\lambda_0^2)}\, d\lambda^2 \tag{2.4.4}$$

where K is the inverse of the integral over $W(\lambda^2)$, the $\circledast$ denotes convolution, and $R(\phi)$ is the RM transfer function (RMTF, in Fig. 2.2). This function, in analogy to telescope optics, is more similar to the point spread function (PSF) than to the optical transfer function (OTF), so it has been renamed the RM spread function (RMSF)

$$R(\phi) \equiv K \int_{-\infty}^{+\infty} W(\lambda^2) e^{-2i\phi(\lambda^2-\lambda_0^2)}\, d\lambda^2. \tag{2.4.5}$$

In this thesis work the latter denomination will be used.

The quantity λ_0^2 is the mean of the sampled λ^2 values, weighted by $W(\lambda^2)$, and has been introduced by Brentjens and de Bruyn (2005) in order to improve the behaviour of the RMSF.

$\tilde{F}(\phi)$ is an approximate reconstruction of $F(\phi)$. More precisely, it is $F(\phi)$ convolved with $R(\phi)$, therefore after Fourier filtering by weight function $W(\lambda^2)$. The quality of reconstruction depends mainly on the weight function $W(\lambda^2)$. A more complete coverage of λ^2 space improves the reconstruction. Fewer gaps in the λ^2 sampling reduce the sidelobes of $R(\phi)$, while covering a larger range of λ^2 increases the resolution in ϕ space. Hence, a complete and wide range of λ^2 measurements leads to a better defined RMSF and a fine sample in ϕ space, allowing a better reconstruction of $F(\phi)$.

This is similar to what happens when performing image synthesis with an array of radio telescopes (Sec. 3.2.1). In that case, the larger is the baseline the higher will be the resolution (smaller synthesized beam), while the higher is the number of measurements the lower will be the height of the sidelobes on the dirty beam. In particular, The RMSF can be seen as conceptually equivalent to the dirty beam

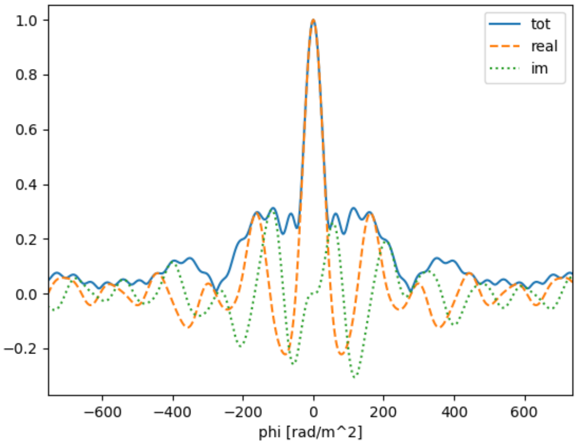

Figure 2.2: The RMSF of the observation used in our thesis work, with 1024 MHz bandwidth, centered at 1.5 GHz, and using 256 frequency channels. The RMSF is shown with $\lambda_0 = 0$. We distinguish with dashed orange lines the real part of the RMSF, with dotted green lines the imaginary part, ad with solid blue lines the amplitude.

produced by an array: in fact, both define the resolution of the final image. Brentjens and de Bruyn (2005) showed that Eqns. 2.4.4 and 2.4.5 can be written as sums: these are the equations which define the RM synthesis technique as it is implemented in practice

$$\tilde{F}(\phi) \approx K \sum_{c=1}^{N} \tilde{P}_c \, e^{-2i\phi(\lambda_c^2 - \lambda_0^2)}, \tag{2.4.6}$$

$$R(\phi) \approx K \sum_{c=1}^{N} W_c \, e^{-2i\phi(\lambda_c^2 - \lambda_0^2)}, \tag{2.4.7}$$

$$K = \left(\sum_{c=1}^{N} W_c \right)^{-1}, \tag{2.4.8}$$

where the index c refers to the individual frequency channels in which the polarized flux is observed at the radio telescope and N is the total channels number.

Three main parameters are involved when using the RM synthesis technique: the channel width $\delta\lambda^2$, the width of the λ^2 distribution $\Delta\lambda^2$, and the shortest wavelength squared λ^2_{min}. These parameters determine respectively the maximum observable Faraday depth, the resolution in ϕ space, and the largest scale in ϕ space to which one is sensitive. Given these parameters, the FWHM of the main peak of the RMSF is given by

$$\delta\phi \approx \frac{2\sqrt{3}}{\Delta\lambda^2} \tag{2.4.9}$$

the scale in ϕ space to which sensitivity has dropped to 50% is

$$\text{max scale} \approx \frac{\pi}{\lambda^2_{\text{min}}} \tag{2.4.10}$$

and the maximum Faraday depth to which one has more than 50% sensitivity

$$\|\phi_{max}\| \approx \frac{\sqrt{3}}{\delta\lambda^2}. \tag{2.4.11}$$

Comparing Eqns. 2.4.9 and 2.4.10 we can see where analogy between RM synthesis and regular synthesis imaging breaks down. In synthesis imaging, the width of the synthesized beam is inversely proportional to the maximum absolute uv vector, that is the distance between the origin and the uv point most distant from it. The maximum scale that one can measure depends on the shortest baseline, therefore one is always maximally sensitive to structures smaller than the width of the synthesized beam.

In RM synthesis instead it is possible that a source is unresolved in the sense that its extent in ϕ is less than the width of the RMSF, yet "resolved" out because one has not sampled the typical ϕ-scale of the source due to lack of small λ^2 points. Eq. 2.4.9 shows that the width of the RMSF depends on the width of the λ^2 distribution, not on the largest λ^2 measured. Nevertheless, the largest scale in ϕ that one is sensitive to is set by the smallest λ^2 as is shown in Eq. 2.4.10.

2.4.1 Faraday dispersion function deconvolution

As seen with Eq. 2.4.4, after performing the RM synthesis the reconstructed Faraday dispersion function, $\tilde{F}(\phi)$, is the convolution of the actual Faraday dispersion function, $F(\phi)$, with the RMSF, $R(\phi)$. When multiple features appear in a reconstructed Faraday dispersion function, confusion with RMSF sidelobes can make the interpretation difficult. The situation can often be improved by performing a deconvolution operation.

In Heald (2009) the `CLEAN` algorithm was proposed in order to realize such deconvolution (see Section 3 for a more complete description of the `CLEAN` algorithm), and is often referred to as `RMCLEAN`: this technique was developed for use with aperture synthesis radio telescope images and described by Högbom (1974). The differences with respect to the "original" `CLEAN` routine are

1. the deconvolution takes place in one dimension (Faraday depth) rather than two (spatial) dimensions;

2. the functions involved are complex quantities.

The implementation of RM synthesis deconvolution proceeds as follows. First, the location of the peak of the reconstructed Faraday dispersion function, ϕ_p, is searched for. Once ϕ_p is determined, the values of the real and imaginary parts of $\|\tilde{F}(\phi_p)\|$ are scaled by a loop gain parameter g typically taken to be 0.1. This is stored as a "clean component". Next, a version of the RMSF, shifted and scaled to be equal to $g\|\tilde{F}(\phi_p)\|$ at $\phi = \phi_p$, is subtracted from the Faraday dispersion function. The residuals are searched for a new peak, and this loop is repeated until the residuals are all below a specified threshold or a maximum number of performed iterations. Finally, the clean components are convolved with a restoring function and added to the residuals. The result is the deconvolved Faraday dispersion function and can be seen in Fig. 2.3.

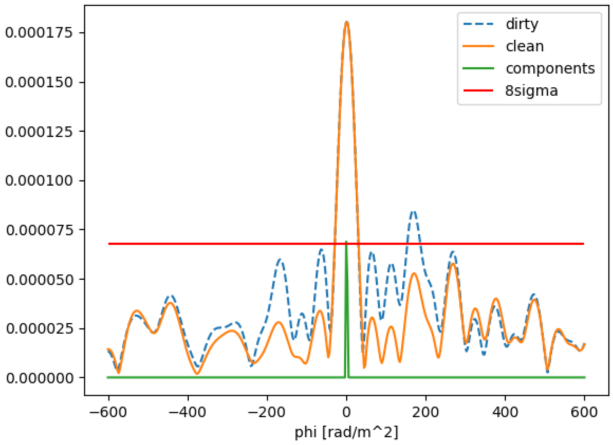

Figure 2.3: An example of the reconstructed FDF deconvolution based on our thesis data. In dashed blue lines we have the "dirty" (original) FDF while in solid orange line we see the "cleaned" FDF. We note the reduction of the sidelobes resulting with this technique. In green we see the selected component relative to the main peak, while the horizontal red line represents the threshold used as a stopping criteria.

Chapter 3

Interferometry fundamentals and radio telescopes imaging

In this Chapter we are going to see the basic theory of interferometry with a quick view on how it works and what we truly observe through radio telescope arrays. The calibration procedure will be presented quickly because the data used in this thesis were already calibrated. Then, we will see how an image can be made starting from reduced data using the so-called `CLEAN` algorithm. Firstly, we present how the imaging is made from a theoretical point of view, then we will see more practically how the `CASA` `tclean` task works and how we configured it, what we did to obtain the final image and how we improved it using the self-calibration.

3.1 Radio interferometry

When we think of a radio telescope we typically refer to a single-dish radio antenna, which is characterized by a large reflector to collect and focus power onto its small feed antenna (connected to receivers), generally with a parabolic shape: this shape is chosen because it can focus the plane wave from a distant point source onto a single focal point, keeping all parts of the on-axis plane wavefront "in phase" at its focal point. This kind of reflector antenna, with a projected diameter D called "aperture", has an effective area A_e which approaches its geometric area $A = \pi D^2/4$.

The response of an radio telescope antenna is not the same in all directions. For a radio telescope, we call "power pattern" the angular distribution of the instrumental response: for a uniformly illuminated aperture, the power pattern $P(\theta)$ is the square of the field pattern

$$P(\theta) = \left(\frac{D}{\lambda}\right)^2 sinc^2\left(\frac{\theta D}{\lambda}\right). \tag{3.1.1}$$

The central peak of the power pattern between first zeros is called the main beam and its angular size, which can be defined as the "half-power beam width" (HPBW), sets the resolution limit for the radio telescope

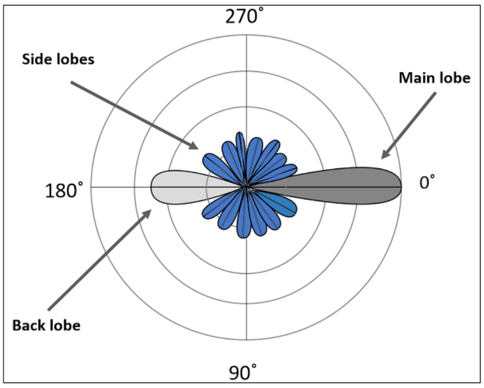

Figure 3.1: This figure represents the power pattern of a dipole antenna. The major part of the received field, in dark grey, is the main beam (or main lobe). This is the portion where maximum gained signal exists and the direction of this lobe indicates the directivity of the antenna. The blue features sidewards are known as sidelobes, and are separated by nulls in the power pattern when $\theta = \pm n\lambda/D$.

$$\theta_{HPBW} \approx 0.89\,\frac{\lambda}{D}. \tag{3.1.2}$$

The resolution of a radio antenna is “diffraction limited”.
In order to recover better angular resolution larger parabolic dishes are required: these are, however, very challenging to build and in fact the largest fully steerable single-dish has a $D \approx 100\,\mathrm{m}$. A solution to this problem comes from interferometry.

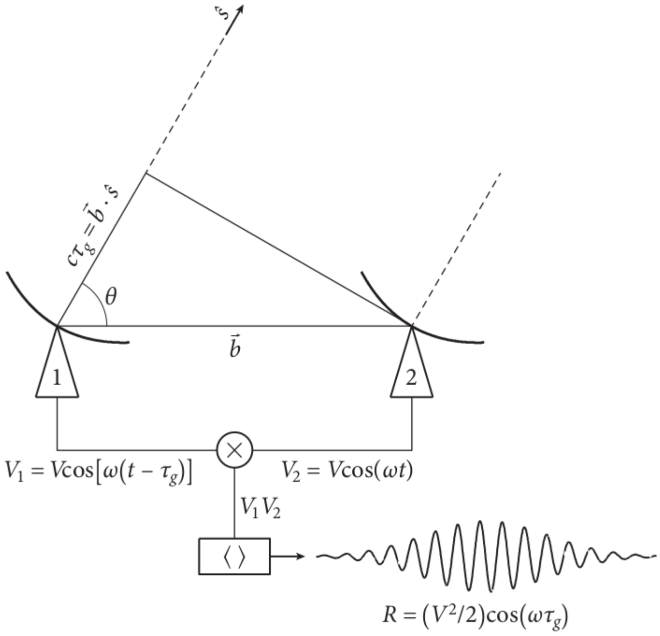

Figure 3.2: Example of two-element multiplying interferometer observing in a very narrow radio frequency range centered on $\nu = \omega/(2\pi)$ (Condon and Ransom, 2016).

The interferometric technique allows to combine several single-dish telescopes into a multi-element array in order to improve the angular resolution. The simplest

example of interferometer is given by a pair of radio telescopes whose voltage outputs are correlated: even the most elaborated interferometers, made by N antennas, can be treated as $N(N-1)/2$ independent two-element interferometers.
Fig. 3.2 shows two identical dishes separated by the baseline vector $\mathbf{b}$ of length b that points from antenna 1 to antenna 2. Both dishes are pointing in the same direction specified by the unit vector $\hat{s}$, and θ is the angle between $\mathbf{b}$ and $\hat{s}$. Plane waves from a distant point source must travel an extra distance in order to reach antenna 1 with respect to antenna 2, and this causes a lag in time called "geometric delay"

$$\tau_g = \frac{\mathbf{b} \cdot \hat{s}}{c}. \tag{3.1.3}$$

The two output voltages of antennas 1 and 2 at time t can be written as

$$V_1 = V \cos\left[\omega(t - \tau_g)\right] \quad \text{and} \quad \mathrm{V_2 = V\cos(\omega t)}. \tag{3.1.4}$$

A correlator multiplies and time averages the two outputs: the correlator output voltage $R = (V^2/2)\cos(\omega\tau_g)$ varies sinusoidally with the Earth rotation, which changes the source direction relative to the baseline vector. These sinusoids are called fringes. The response R of a two-element interferometer is this sinusoid multiplied by the product of the voltage patterns of the individual antennas. In most arrays, like JVLA, the two antennas are identical, so this product is the power pattern of the individual antennas and is called the "primary beam" of the interferometer.

In case of a multi-element interferometer, the instantaneous synthesized beam projected on the sky is the arithmetic mean of the individual responses of its component two-element interferometers, and rapidly approaches a Gaussian as N increases. The synthesized beam, which represents the point-source response of the array, is generally called "dirty beam" $B(x, y)$. If the source is slightly extended, with sky distribution $I_\nu(\hat{s})$, the response of the interferometer is obtained by treating the extended source as the sum of independent point sources. The combination of cosine and sine correlators is called a "complex correlator". The "complex visibility" is defined as

$$V \equiv R_c - iR_s = Ae^{-i\phi}, \tag{3.1.5}$$

where R_c is the cosine correlator, R_s the sine correlator, $A = (R_c^2 + R_s^2)^{1/2}$ is the visibility amplitude, and $\phi = \tan^{-1}(R_s/R_c)$ is the visibility phase.
The response to an extended source with brightness distribution $I_\nu(\hat{s})$ of the two-element interferometer with a complex correlator is the complex visibility, which is the Fourier transform of the sky brightness distribution

$$V = \int I(\hat{s})\, exp(-i2\pi\mathbf{b} \cdot \hat{s}/\lambda)\, d\Omega. \tag{3.1.6}$$

The three-dimensional generalization of Eq. 3.1.6 is

$$V(u,v,w) = \int\int \frac{I_\nu(l,m)}{(1-l^2-m^2)^{1/2}}\, e^{-i2\pi[ul+vm+w(\sqrt{1-l^2-m^2}-1)]}\, dldm \tag{3.1.7}$$

where u, v, and w are the components of the baseline vector in wavelength units and l,m are cosine sky coordinates.
The w-axis is in the reference direction $\hat{s}_0$ usually chosen to contain the target radio source: however, in case of small fields of view (FoV), $w = 0$ making Eq. 3.1.7 an ordinary invertible two-dimensional Fourier transform.

A single baseline "samples" a discrete point in the (u,v) plane by measuring both the amplitude and the phase of the complex visibility. Given two-element interferometer made by the i-th and j-th antennas, the visibilities obtained can be written as

$$V^{ij} = A^{ij} e^{-i\phi^{ij}}. \tag{3.1.8}$$

The observed visibilities, V^{ij}_{obs}, are different from the intrinsic ones, V^{ij}_{true}, because of the presence of several factor that can corrupt the incoming sky signal as it propagates through the telescope receivers: phase distortions due to the atmosphere, amplitude variations due to the electronics, polarization leakages, etc.
In order to correct the observed visibilities for these effects, in a process known as "calibration", complex factors called "gains", G^{ij} in Eq. 3.1.9, are defined to account for these corruptions and, once found their values (usually observing known sky sources called "calibrators"), to correct the received signal

$$V^{ij}_{obs} = G^{ij} V^{ij}_{true}. \tag{3.1.9}$$

3.2 Synthesis imaging

3.2.1 The `CLEAN` algorithm

Once visibilities are calibrated, they can be Fourier-transformed to obtain a sky image. Under the assumption of small FoV, as said before, the relation between V and I_ν becomes a simple 2D Fourier transform and the sky brightness distribution can be written as

$$I_\nu(l,m) = \int\int V(u,v)\, e^{2\pi i(ul+vm)}\, dl\, dm. \tag{3.2.1}$$

$V(u,v)$ is a continuous function: if one could sample continuously the (u,v) plane we would be able to obtain directly the true visibility function and, doing its Fourier transform, the sky brightness distribution without using any deconvolution. However, the sampling of the (u,v) plane depends, among the others, on the number of baselines and their projected lengths; even the Earth rotation can be used to increase the number of components (visibilities) available, in order to extend the (u,v) coverage in a technique known as "Earth-rotation aperture synthesis". Nevertheless, it is not possible to sample $V(u,v)$ through all the (u,v) plane, so the sky

brightness distribution cannot be obtained by doing just a Fourier transform: we need to operate a deconvolution using what we are able to sample from the array.
As we said before we cannot sample the entire (u,v) plane, so we have visibilities only in the sampled points of the plane: we can define the sampling function $S(u,v)$, whose inverse Fourier transform gives the dirty beam, as the function which contains all the points where visibilities are measured. If we multiply this function with the true visibility from the source, which is the ideal Fourier transform of the source brightness distribution, we obtain the sampled visibility, which is what we truly observe with our interferometer and will be our starting point for the image reconstruction. The inverse Fourier transform of the sampled visibility, called "dirty map", gives the true sky brightness distribution, which is the final result we want to obtain at the end of the cleaning process, convolved with the dirty beam. Hence, so to obtain the final map we have to "deconvolve" the dirty map for the dirty beam, which means to reduce the sidelobes created by the gaps in (u,v) coverage to obtain the best possible image: this is what the `CLEAN` algorithm does.
We present now the `CLEAN` algorithm (Clark, 1980, Högbom, 1974), which is the most popular and widely-studied method for reconstructing a model image based on interferometer data, implemented in the `tclean` task of `CASA` (Common Astronomy Software Applications McMullin et al., 2007). The `CLEAN` algorithm assumes that the sky brightness can be described as a sum of point-like sources.

1. Initializes the residual map $I^R(x,y)$ to the dirty map $I^D(x,y)$ and the `CLEAN` components $I^C(x,y)$ list to an empty value.

2. The first `CLEAN` cycle finds the peaks of a certain intensity I_{max} in the residual map and saves them as clean components, multiplying them for the "loop gain" γ (in our case $\gamma = 0.1$) and removing them from the residuals;

3. A dirty beam pattern is subtracted over the whole map, including the full sidelobes, centered on the position of the peaks saved in the clean component list, and normalized to the $\gamma \times I_{max}$ at the beam center: going on iterating, where for every iteration the residual image becomes the new dirty image, other peaks will emerge in the residuals map that will be removed and added to the model, and the cycles keep going until certain stopping criteria are reached. The final clean components list contains all the peaks with different intensities found in all the different cycles
$$I^R(x,y) = I^D(x,y) - \gamma B(x,y) \ * \ I^C(x,y). \tag{3.2.2}$$

4. Now is time to "restore": the clean components are multiplied for the clean beam $B^{clean}(x,y)$, which is the mathematical Gaussian that better fits the main lobe of the dirty beam, and added back to the residuals map with the same position but only with the main lobe to obtain the "cleaned" final image $I(x,y)$
$$I(x,y) = I^C(x,y) \ * \ B^{clean}(x,y) + I^R(x,y). \tag{3.2.3}$$

This is how an image is built.

3.2.2 Self-Calibration

The initial calibration assumes that the amplitude and phase terms of the gains are constant, where the phase is evaluated using a phase calibrator, which is near the source and observed repeatedly every 20/30 minutes. However, in order to refine the solutions, it is possible to use the image itself for a further calibration: this operation is called "self-calibration".

The idea here is to derive a model from the data imaged after the initial calibration, and refine phase and amplitude gain solutions because there can be residual phase or amplitude errors in the data. The observed visibility data on the i-j baseline can be seen as in Eq. 3.1.9. For an array made by N antennas, at any given integration time, there are $N(N-1)/2$ visibility data but only N gain factors, needed to convert what we observe in what is the true visibility (without instrumental or atmospheric noise): but if $N \geq 8$ solutions to this set of coupled equations converge quickly, so we can obtain V^{ij}_{true}.

To better explain the self-calibration procedure, we outline the structure of a measurement set (MS). There are three column of interest in the dataset: the `DATA` column, the `MODEL` column and the `CORRECTED DATA` column. With the split we made just before the imaging we set the `CORRECTED DATA` column equal to the `DATA` column.

1. Produce an image with the `tclean` task using the `CORRECTED DATA` column, like we have just done.
2. Derive the gain corrections using the `gaincal` task by comparing the `DATA` columns and the Fourier transform of the image, stored in the `MODEL` column, and these gains are saved in an external table.
3. Apply these corrections through the `applycal` task to the `DATA` column, to form a new `CORRECTED DATA` column which is different from the previous and will be used for the imaging.

At the end of these steps, if the selfcal gain solutions have improved the calibration we expect to have an image with a lower RMS and less artifacts.

3.2.3 Primary beam correction

The aperture illumination function (AIF) of each antenna results in a direction-dependent complex gain that can vary with time and is usually different for each antenna. The resulting antenna power pattern is called the "primary beam" and is the most important direction-dependent effect.

A simple method of correcting the effect of the primary beam is a post-deconvolution image-domain division of the model image by an estimate of the average primary beam or some other model. This method ignores primary beam variations across baselines and time, and is therefore approximate, limiting the imaging dynamic range even within the main lobe of the beam.

The primary beam correction can be made within the `tclean` task in `CASA` or using a specific task called `impbcor` (McMullin et al., 2007): this constructs a primary beam corrected image from an image and a primary beam pattern. The primary beam pattern can be provided as an image, in which case:

1. it must have the same shape as the input image and its coordinate system must be the same, or
2. it must be a 2D image in which case its coordinate system must consist of a (2-D) direction coordinate which is the same as the direction coordinate in the input image and its direction plane must be the same shape as that of the input image.

By default, the image is divided by the primary beam pattern.
This allows to correct the response of the antennas in the array to get accurate intensities for source outside the core of the beam.

3.2.4 Robust Weighting

With large arrays, the visibility data in the (u,v) plane must be interpolated onto a uniform grid in order to make computations tractable (see Sec. 5.2 from Thompson et al., 2017). The simplest approach is called "cell averaging", where each data point is associated with the nearest (u,v) grid point. The number of points averaged in a cell will decrease with increasing (u,v) distance, and many cells will have zero entries. Thus, the variance of the visibility estimates will vary considerably over the (u,v) plane. A compromise must be reached between the goal of forming a synthesized beam that is narrow and has low sidelobes and achieving the optimum sensitivity for the detection of weak sources.
The best strategy for detecting a weak point source in the field is to use "natural" weighting, where weights are inversely proportional to the noise variance of a visibility. This is equivalent to give weights equal to unity to all data, as the noise is usually uniformly distributed. This weighting scheme provides the maximum imaging sensitivity at the expense of a lower resolution and higher PSF sidelobes.
On the other hand, an image with better resolution and lower sidelobes can be obtained with "uniform" weighting, where the gridding weights per visibility data point are the original data weights divided by the total weights of all data points that map to the same (u,v) grid cell.
Briggs (1995) introduced a logarithmic parametrized scheme that allows a continuous variation in weighting between uniform and natural weighting. The process is called "robust" weighting. The weighting of cell (i,k) in the (u,v) plane whose visibility has an rms error of σ_{ik} is specified as

$$w_{ik} = \frac{1}{S^2 + \sigma_{ik}^2}, \tag{3.2.4}$$

where S is a parameter defined by

$$S^2 = \frac{(5 \times 10^{-R})^2}{\bar{w}}. \tag{3.2.5}$$

R is the robustness factor, and $\bar{w}$ is the average variance weighting factor over the number of cells in the image.

The nominal range of R is -2 to 2. $R = 2$ makes S very small with respect to w so that the weighting approaches natural weighting (high sensitivity), whereas $R = -2$ makes S large with respect to w so that the weighting approaches the uniform weighting (high resolution). As this value increases, the effect of a bad point in a cell with few data points is suppressed.

3.3 Wide-band and wide-field imaging

We have just described an approach to radio interferometric images that relies on the approximation of small FoVs, for which $w = 0$ making Eq. 3.1.7 an ordinary invertible two-dimensional Fourier transform. Wide-field imaging typically, instead, refers to FoVs over which the basic 2D Fourier transform assumption of interferometric imaging does not apply and where standard on-axis calibration will not suffice.

For wide-field imaging, sky curvature and non-coplanar baselines result in a non-zero w term. Standard 2D imaging applied to such data will produce artifacts around sources away from the phase center: luckily, efficient algorithms exist to correct for many of these effects.

3.3.1 W-projection

We have seen before that the response of a narrow-frequency interferometer to spatially incoherent radiation from the far field can be expressed as Eq. 3.1.7: when the magnitude of the term $2\pi w(\sqrt{1-l^2-m^2}-1)$ is much less than unity it may be ignored, and this is the assumption that held in our previous analysis. However, if this term is comparable to or exceeds unity, a 2D Fourier transform cannot be used: as a consequence, it is not possible to estimate the sky brightness by simple Fourier inversion of the measured visibility. With the assumption that the maximum $w \approx b_{max}/\lambda$, the value of the extra phase term is roughly

$$\frac{b_{max}\lambda}{D^2} = \left(\frac{r_F}{D}\right)^2, \tag{3.3.1}$$

where b_{max} is the maximum baseline length, D is the antenna aperture, and λ is the observing wavelength. The parameter r_F is the Fresnel zone diameter for a distance b_{max}. It is easier to work with the inverse of r_F, which is called Fresnel number

$$N_F = \frac{D^2}{b_{max}\lambda}. \tag{3.3.2}$$

Wide-field imaging is affected by this non-planar baselines effect when the Fresnel number N_F is less than unity: this occurs for small apertures, long baselines, or long wavelengths (Cornwell et al., 2008).

In this thesis work we had to deal with this issue and, in order to solve it, we used the "w-projection" technique in `CASA`. In this method, visibilities with non-zero w values are gridded using a gridding convolution function (GCF) given by the Fourier transform of the Fresnel electromagnetic-wave propagator across a distance of w wavelengths. In practice, GCFs are computed for a finite set of w values ("wprojectplanes") and applied during gridding. W-projection is implemented in the `tclean` task in `CASA` via *gridder='wproject'* (McMullin et al., 2007). The *wprojplanes* parameter must be set: it represents the number of discrete w values that must be used to quantize the range of w values present in the dataset to be imaged. An appropriate value of *wprojplanes* depends on whether there is a bright source far from the phase center, the desired dynamic range of the image, the maximum w value in the measurements, and the desired trade off between accuracy and computing cost. The formula that `CASA` uses to calculate the number of *wprojplanes* is

$$N_{wprojplanes} = 0.5 \times \frac{W_{max}}{\lambda} \times \frac{imsize}{(radians)}, \tag{3.3.3}$$

where W_{max} is the maximum w in the (u,v,w) data and *imsize* is the largest linear size of the image.

3.3.2 Image modes and deconvolution algorithms

Until recently, with broad-band instruments such as Jansky Very Large Array (JVLA), Australian Square Kilometer Array Pathfinder (ASKAP) or Low Frequency Array (LOFAR), the primary goal of wide-band imaging has been to obtain a continuum image that makes use of the increased sensitivity and spatial-frequency coverage offered by combining multi-frequency measurements. To do so, we need imaging algorithms that model and reconstruct both spatial and spectral structure simultaneously, and that are also sensitive to various effects of combining measurements from a large range of frequencies (namely varying ranges of sampled spatial scales and varying array-element response functions).

Deconvolution refers to the process of reconstructing a model of the sky brightness distribution, given a dirty/residual image and the point-spread-function of the instrument. This process is called a deconvolution because under certain conditions, the dirty/residual image can be written as the result of a convolution of the true sky brightness and the PSF of the instrument.

We have seen in Sec. 3.2.1 the `CLEAN` algorithm, which is the basis of most deconvolution algorithm used in radio interferometry. However, there exist several variants of this technique. For example, fields of compact sources are best represented by delta function locations and amplitudes. Extended emission is modeled as a linear combination of components of different scale sizes and transformed into a multi-scale basis where again, delta functions are all that are required to mark the location and amplitude of blobs of different sizes. Multi-term algorithms for wideband imaging model the sky brightness and its spectrum simultaneously, using coefficients of a Taylor polynomial as a sparse representation of a smooth spectrum. In this case, the location of each (multi-scale) component is chosen via a search and the values of the Taylor coefficients for that component are solved for via a direct linear least squares calculation.

In order to account for the varying source spectrum and PSF over large observing bandwidth, the "Multi-Frequency Synthesis" (MFS) (Conway et al., 1990) has been developed. This represents the technique of combining measurements at multiple discrete receiver frequencies during synthesis imaging. MFS was initially done to increase the aperture-plane coverage of sparse arrays by using narrow-band receivers and switching frequencies during the observation. Data from all selected data channels are mapped to a single broadband uv-grid using appropriate *uvw* coordinates, and then imaged. This option is accessed via *specmode = 'mfs'* option in the `tclean` task.

An improvement to standard MFS is the Multi-Term MFS (MTMFS). It accounts for changes in spectral index as a function of sky position and uses Taylor-weighted averages of data from all frequencies accumulated onto N terms uv-grid before imaging. These Taylor-weighted residual images form the input for the minor cycle of the MTMFS deconvolution algorithm, which performs a linear least squares fit during deconvolution to obtain Taylor coefficients per component. This option is accessible via *specmode='mfs'* and *deconvolver='mtmfs'*. The advantages of such an image reconstruction are that the combined (u,v) coverage from all channels is used, flux components are "tied" across frequency by the use of an explicit spectral model or physically motivated constraints, and the angular resolution of the resulting intensity and spectral index images is not limited to that of the lowest frequency in the band.

The MTMFS algorithm models the spectrum of each flux component by a Taylor series expansion about frequency ν_0

$$\mathbf{I}_\nu^m = \sum_{t=0}^{N_t-1} w_\nu^t \mathbf{I}_t^{sky}, \quad \text{where} \quad \mathrm{w}_\nu^\mathrm{t} = \left(\frac{\nu-\nu_0}{\nu_0}\right)^\mathrm{t} \tag{3.3.4}$$

where $\mathbf{I}_\nu^m$ represents a multi-scale model image, $\mathbf{I}_t^{sky}$ a multi-scale Taylor coefficient image, and N_t the order of the Taylor series expansion, which can be set in the `tclean` task with *nterms* (Rau and Cornwell, 2011).

By increasing the number of terms, it i be possible to remove spectral artifacts. One practical choice for the coefficient image is represented by a power law with a varying index, given also that continuum synchrotron emission is usually modeled and observed as a power law distribution with frequency

$$\mathbf{I}_\nu^{sky} = \mathbf{I}_{\nu_0}^{sky}\left(\frac{\nu}{\nu_0}\right)^{\mathbf{I}_\alpha^{sky}+\mathbf{I}_\beta^{sky}\ln\left(\frac{\nu}{\nu_0}\right)}. \tag{3.3.5}$$

Here, I_α^{sky} represents an average spectral index and I_β^{sky} represents spectral curvature.

A Taylor expansion of Eq. 3.3.5 yields the following expressions for the first three coefficients from which the spectral index I_α^{sky} and the curvature I_β^{sky} can be computed algebraically

$$\mathbf{I}_0^m = \mathbf{I}_{\nu_0}^{sky} \quad ; \quad \mathbf{I}_1^\mathrm{m} = \mathbf{I}_\alpha^\mathrm{sky}\mathbf{I}_{\nu_0}^\mathrm{sky} \quad ; \quad \mathbf{I}_2^\mathrm{m} = \left(\frac{\mathbf{I}_\alpha^\mathrm{sky}(\mathbf{I}_\alpha^\mathrm{sky}-1)}{2}+\mathbf{I}_\beta^\mathrm{sky}\right)\mathbf{I}_{\nu_0}^\mathrm{sky}. \tag{3.3.6}$$

3.3.3 w-stacking

The final images used for the RM synthesis technique have been obtained using the software `WSClean v3.1.0` (Offringa et al., 2014). The different task for this package will be described in the data analysis part (Sec. 5.2). Here we present the "w-stacking" algorithm implemented in the software, which accounts for the three-dimensional nature of the sky curvature in a different way with respect to what is done in `CASA` (Sec. 3.3.1). With this technique, Eq. 3.1.7 is re-written factorizing the w-dependent term from the others, obtaining

$$V(u,v,w) = \int\int \frac{I_\nu(l,m)e^{-i2\pi w(\sqrt{1-l^2-m^2}-1)}}{(1-l^2-m^2)^{1/2}} e^{-i2\pi(ul+vm)}\, dldm. \tag{3.3.7}$$

The FoV is divided in tiles of sufficiently small angular size so that the w term of each tile can be approximated as constant, e.g. the small FoV approximation holds for each tile. Therefore, inside each tile, Eq. 3.3.7 is an ordinary two-dimensional Fourier transform going from (u,v) space to (l,m) space (2D Fourier transform), and can be inverted to get

$$\frac{I(l,m)}{\sqrt{1-l^2-m^2}} = e^{i2\pi w(\sqrt{1-l^2-m^2}-1)} \int\int V(u,v,w)e^{i2\pi(ul+vm)}\, dudv. \tag{3.3.8}$$

Then, in order to reconstruct for sky signal from every direction (e.g. for all the possible w terms), Eq. 3.3.8 is integrated (both sides) over w_{min} to w_{max}, the minimum and maximum value of w respectively, resulting in

$$\frac{I(l,m)(w_{max}-w_{min})}{\sqrt{1-l^2-m^2}} = \int_{w_{min}}^{w_{max}} e^{i2\pi w(\sqrt{1-l^2-m^2}-1)}\, dw \int\int V(u,v,w)e^{i2\pi(ul+vm)}\, dudv. \tag{3.3.9}$$

The final step is to make the (u,v,w) parameters discrete, so that the integration over u and v can become an inverse Fourier transform and the integration over w becomes a sum.

These are the principles of the w-stacking technique, which calculates the 2D Fourier transform for a fixed w and then sums over all possible w values. With this technique, it is possible to quickly recover $I(l,m)$ and correct for large FoVs, e.g. overcoming the planar-sky assumption.

3.3.4 Multi-scale cleaning

`WSClean` supports multi-scale deconvolution with an optimized version of the Cornwell (2008) algorithm.

Like `CASA`, `WSClean` multi-scale deconvolution selects the highest peak and subtracts it with the best fitting "scale", although internally it works somewhat different.

In `WSClean`, the scales to fit for do not have to be specified: `WSClean` will automatically use as many scales as necessary. The delta scale is always present, while the next scale is calculated relative to the synthesized beam. Further scales are added by continuing to multiply by two until the scale is larger than the image size. Multi-scale deconvolution can be turned on by adding *multiscale* to the command line.

Chapter 4

PSZ2 G096.88+24.18

PSZ2 G096.88+24.18 (also known as ZwCL1856.8+6616, Zwicky et al., 1961) was detected in the Planck Sunyaev-Zel'dovich Survey (Planck Collaboration et al., 2011), through the SZ effect as explained in Sec. 1.1.3, and reported to have a redshift $z = 0.304$ and mass $M^1{}_{500} = (4.7 \pm 0.3) \times 10^{14}\ M_\odot$ in the second Planck data release (Planck Collaboration et al., 2016).
Using optical and X-ray data, Finner et al. (2021) investigated the merger scenario of PSZ2 G096.88+24.18 (Fig. 4.1). They estimated a 1:1 mass ratio, with a total mass of $M^1{}_{200} = 2.4^{+0.9}_{-0.7} \times 10^{14}\ M_\odot$, from simoultaneously fitting two Navarro-Frenk-White (NFW) halos to the lensing signal. This mass estimate is lower than the SZE mass estimate from Planck. However, cluster masses derived from the SZE are known to be significantly larger than those derived from weak lensing, primarily due to departures from hydrostatic equilibrium, to which SZE measurements are sensitive (see von der Linden et al., 2014, and references within).
Combined with the spectroscopic results of Golovich et al. (2019), who found a single-peak redshift distribution of galaxies associated with PSZ2 G096.88+24.18, the merger is likely a head-on collision on the plane of the sky and the time since collision is $0.7^{+0.3}_{-0.1}$ Gyr. This merger state is confirmed also by X-ray observations, where there are two clumps of gas at a projected distance of $\sim$ 600 kpc.

de Gasperin et al. (2014) discovered a pair of radio relics on the northern and southern edges of PSZ2 G096.88+24.18 at 1.4 GHz with Westerbork Synthesis Radio Telescope (WSRT). The two relics have dimensions of ~900 kpc (northern) and ~1.4 Mpc (southern), and are at a distance from the peak of X-ray emission of 770 kpc and 1145 kpc, respectively. They also made a polarization analysis, and found that the Relic N appear to have electric field vectors mostly aligned perpendicular to the relic extension meaning that the magnetic field is aligned with the relic (as found in other relics, see Sec. 1.3). However, the Relic S shows vectors that are ~45° apart from being perpendicular to the relic extension.
These observational results, together with the short distance between the relics and the peak of the cluster X-ray emission, suggest that the merger axis is slightly tilted compared to the plane of the sky, with the southern relic farther away from the

---

[1] $M_{500(200)}$ is the mass enclosed within the radius $r_{500(200)}$, at which the mean density of the cluster is 500(200) times the critical density of the Universe at the cluster redshift.

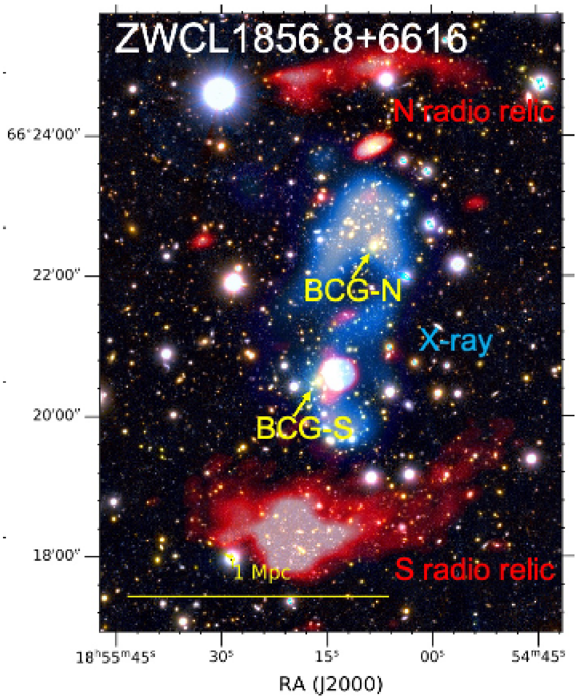

Figure 4.1: Subaru color image of ZWCL1856.8+6616 with 114 MHz LOFAR radio emission (red) from Jones et al. (2021) and 0.5-7 keV XMM-Newton X-ray emission (blue). Yellow arrows mark the location of the two BCGs. The bright X-ray morphology shows an inverted S shape in both clusters. The position and alignment of the radio relics are almost mirrored and are located at opposite ends of the elongated X-ray distribution (Finner et al., 2021).

observer meaning further Faraday rotation effect for the relic. In fact, recalling Eq. 2.3.4, if the source lies further from the observer we expect to have higher RM (and σ_{RM}), with a consequent higher depolarization.
Moreover, they detected traces of an extended, low-surface brightness feature extending from the two relics towards the centre of the cluster that can be a hint of a halo which could extend from the cluster centre up to the two radio relics.

More recently, Jones et al. (2021) studied this cluster in order to unveil the nature of a "connection" between a bright radio galaxy and the southern relic that affects its properties. With respect to the previous article, they used LOFAR High Band Antenna (HBA) stations, at 120-187 MHz, and VLA L-band radio observations (with C and CnB-B configurations), as well as Chandra data of the cluster.

The morphology, location at the cluster periphery, and spectral index variation (Fig. 4.2) of the arc-like radio structures in PSZ2 G096.88+24.18 confirm that we are observing a pair of radio relics. At 120-187 MHz the relics have largest linear sizes (LLS) of ~0.9 and 1.5 Mpc and a flux ratio of 1:3.5 for the north and south relics respectively. Both relics have a non-uniform brightness along their major axis, and high resolution images show filament-like substructures in the northern relic.
Both the north and south relics exhibit spectral steepening from the shock edge towards the cluster centre (Fig. 4.2), from about $\alpha = 0.6$ to $\alpha = 2.0$ for the southern relic and $\alpha = 0.5$ to $\alpha = 1.5$ for the northern relic. A spectral steepening towards the cluster centre is expected from downstream synchrotron and IC losses, as ob-

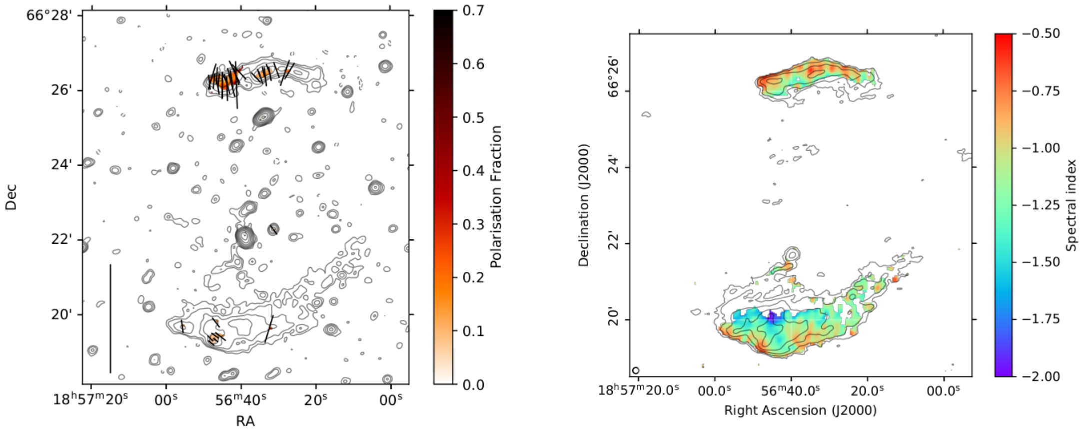

Figure 4.2: Left: Linear polarization fraction image. Electric field vectors are plotted in black, with amplitude proportional to the polarization fraction. A reference vector, corresponding to 100% polarization fraction, is plotted in the bottom left. Contours are set at $3\sigma_{rms} \times [1, 2, 4, ...]$ from VLA 1.5 GHz image (resolution: 10" × 9", RMS noise: 8 μJy beam^{-1}), while dashed contours are set at $-3\sigma_{rms}$.
Right: Spectral index map created between 140 MHz and 1.5 GHz at 10"×10" resolution (Jones et al., 2021).

served in many other clusters (Bonafede et al., 2012, Hoang et al., 2017, van Weeren et al., 2016). Whilst the radio relics show a general steepening of the spectral index towards the cluster centre, the distribution in the southern relic is non-uniform.
Despite the availability of X-rays data, they were unable to detect evidence of a shock front at the position of the relics. Due to the low count statistics in cluster outskirts, the Chandra data are likely not sensitive enough to detect a shock. Finner et al. (2021) also did not detect a shock with a 12 ks XMM-Newton observation. The low electron density at the outskirts of galaxy clusters, where radio relics are typically located, makes detection of shocks with X-ray observations challenging.

In their polarimetric analysis (Fig. 4.2), they found that in the northern relic there are significant regions of polarized emission, mostly corresponding to the brightest parts of the relic, with a linear polarization fraction which ranges from 10-60% and magnetic field ordered and compressed along the shock front, as a consequence of the shock front passage (Enßlin et al., 1998). The southern relic has polarised emission in only a few small regions and the polarization fraction is much lower than in the northern relic, reaching a maximum of 20%. In these small regions, the electric field vectors do not lie perpendicular to the shock, in agreement with the results by de Gasperin et al. (2014).
These findings are in line with those of de Gasperin et al. (2014), although obtained with a different dataset.
The origin of the different behaviour of polarization in the two relics is not yet understood.

- de Gasperin et al. (2014) suggested that this could be caused by the southern relic lying further away from us. In this scenario, the observed radio emission would have to pass through more magnetized, ionized plasma and therefore be subject to more Faraday rotation (as discussed before, see also Eq. 2.3.4). Spectroscopic observations of PSZ2 G096.88+24.18 show that the redshift distribution of the member galaxies is well fit by a single Gaussian (Golovich et al., 2019). This makes it unlikely that significant additional Faraday rotation due to projection effects is causing the observed difference in polarization angle. However, we need to consider that gas and galaxies can have a different distribution: this is in fact a key point of our discussion, that is carried out in Ch. 6.

- The localised nature of the polarized emission and unexpected electric field vector orientation could instead indicate that we are observing emission from a polarized radio galaxy in projection within the relic. However, the area of polarized emission coincides with the brightest part of the radio relic, making it almost impossible to determine from the radio observations if there is indeed a radio galaxy producing the polarized emission that we observe. Furthermore, any likely optical counterparts in the Subaru image has been observed.

- Another possible reason for the lack of polarized emission in the southern relic could be that the turbulence in the relic has mixed the magnetic field lines. Turbulence mixes field lines at scales larger than the Alfvén (l_A), the scale at which the velocity of turbulence is equal to Alfvén speed (Brunetti and Lazarian, 2016). If this scale is smaller than the beam size, then we would observe depolarization effects. In view of this, the stark differences between the north and south relics may be explained if the turbulence in the north relic is generated with lower efficiency or at larger scales than in the south relic.

In this thesis work, we will use new polarimetric observations and we will use 3D magnetic field simulations to constrain the magnetic field power spectrum and understand what is causing the low polarization fraction observed in the southern relic.

Chapter 5

Data analysis: imaging and the application of Rotation Measure synthesis technique

After a presentation of the state of the art on the magnetic fields in GC, especially derived from polarimetric analysis, and a quick view of the theoretical aspect of the techniques and softwares that we use, we will describe in this Chapter the process of data analysis, that comprehend the practical application of image synthesis and RM Synthesis technique discussed in Chapters 2 and 3.

5.1 Data used in this thesis work and imaging

For this thesis work, we used radio data with JVLA telescope in the L band (1-2 GHz). For each observation, presented in Tab. 5.1, the band has been divided in 16 Spectral Windows (Spw), each of them composed by 16 channels of 4.0 MHz, for a total bandwidth of 64.0 MHz per spectral window.

Freq. (GHz)	Array Conf.	Obs. date	Tot. obs. time	Beam Size	RMS (Jy beam^{-1})
1.5 GHz	B	2017 Oct. & Dec.	4h 20m	3.6” × 2.7”	1.4×10^{-5}
1.5 GHz	C	2016 Feb.	3h 30m	14.5” × 9.7”	1.9×10^{-5}
1.5 GHz	D	2017 Feb.	46m	61.3” × 29.3”	6.8×10^{-5}

Table 5.1: List of the observations used in this thesis work. Column 1: central frequency of the observation. Column 2: JVLA antennas configuration. Column 3: year and months of observation. Column 4: size of the restoring beam with Briggs weighting scheme and *robust=0*. Column 5: best RMS obtained for every dataset.

This thesis work starts from data that had already been calibrated. For the first imaging part we used `CASA v6.4.0.16` (McMullin et al., 2007). Now we present the imaging analysis made for the single configurations, with the aim of obtaining images in I, Q, and U configurations in order to increase the sensitivity to the extended emission and, at the same time, to identify the sources that contaminate this emission. Then, we put together all the three configurations in order to remove the external sources and obtain the basic image for the Rotation Measure synthesis technique.

5.1.1 D-configuration

In order to make the interferometric image in total intensity (Stokes I), it is required to set the main parameters in the imaging software that we used (`tclean` task in `CASA`).

First of all, we need to set the pixel size and the image size. For the cell size, we need to follow the "Nyquist theorem" (Shannon, 1949, and references within), which requires the sampling of the beam size with at least 2 pixels: in this thesis work, we will sample it 4 times in order to determine the cell size

$$\text{cell size} = \frac{1}{4 \times \text{max UVwave}} = 10\text{''}, \tag{5.1.1}$$

where "max UVwave" is the maximum projected baseline separation in units of the observing wavelength (in this case $\lambda = 20$ cm). Then, we need to give `tclean` the dimensions of the image. This is the FoV expressed in pixels

$$\text{FoV} = \frac{\lambda}{D} \approx 1648\text{''} \approx 28' \ , \tag{5.1.2}$$

$$\text{imsize} = \frac{\text{FoV}}{\text{cell size}} = 240 \text{ pixels}. \tag{5.1.3}$$

In Sec. 3.3.2 the theoretical concepts of the deconvolution algorithms were presented: now, we will see their practical applications.

We used a multi frequency multiscale imaging deconvolution algorithm (using *specmode='mfs'* and *deconvolver='mtmfs'* in `CASA`, see Sec. 3.3.2) to improve the MFS reconstruction because we use the combined (u,v) coverage from all channels. The deconvolution *scales* that we choose are:

$$\text{scales} = [0,\ \text{beam (in pixels)},\ 3 \times \text{beam (in pixels)}].$$

With these scales we are setting the dimension of the circular Gaussians that are used for the model. It is recommended that a zero scale always be included to model unresolved sources. The largest scale size should be less than or equal to the smaller dimension of large scale features. One must also take care to avoid scale sizes that correspond to the unmeasured short spacings in the central region of uv space, as the reconstruction on these scales will see no constraints from the data and can result in arbitrary values (or divergence).

Related to the multi-frequency mode there is also the number of Taylor coefficients in the spectral mode: we imposed *nterms = 3*, for a 3rd order Taylor expansion about the central frequency 1.5 GHz.

weighting = 'briggs' is a weighting scheme that is intermediate between natural and

uniform weighting, based on the value of the robustness parameter R (see Sec. 3.2.4). For this configuration, and intermediate value of robustness has been used, with *robust = 0*.
Finally, we used *gridder = 'wproject'* in order to correct for the sky curvature (see Sec. 3.3.1) and better "clean" the most peripheral sources of the image, reducing the artifacts. Following Eq. 3.3.3, we imposed *wprojplanes = 256*.
For the starting image, the beam measures 61.3" × 29.3" and the $\sigma_{rms} = 1.4 \times 10^{-4}$ Jy beam^{-1}. This was the only configuration for which the self-calibration was possible. Thanks to 4 self calibration cycles, we were able to reduce σ_{rms} to 6.8×10^{-5} Jy beam^{-1}. The solutions are computed every 60 seconds for the first self-calibration, and then every 40 seconds for the rest of the cycles, and are applied only to the first 14 spectral windows. This choice was made because for the last two spectral windows, given the low flux at these frequencies within the band, the SNR was too low to allow a good working self-calibration. To be able to use them for the polarimetric analysis we then preserve them, given that solutions for these spectral windows have not been found.

5.1.2 C-configuration

Here we have a restoring beam of 14.5" × 9.7", with a $\sigma_{rms} = 1.9 \times 10^{-5}$ Jy beam^{-1}, in case of a *weighting='briggs'* with *robust = 0* and *scales = [0, 5, 15]*, corresponding to 0, 14.5", and 43.5", respectively. Also in this case the original image present a RMS near the thermal noise, and the self-calibration did not help improving the image further.

5.1.3 B-configuration

The resulting image has a restoring beam of 3.6" ×2.7" and $\sigma_{rms} = 1.4 \times 10^{-5}$ Jy beam^{-1} and does not present artifacts. Here, given that we did not see particularly bright sources in the peripheral regions of the image, we chose to reduce the image size around the cluster.
We tried to perform a self-calibration for this dataset but, unfortunately, it did not improve the RMS with respect to the original image.

Once the different configurations have been analyzed individually, we have combined the observations in the visibility space, in order to obtain a single image on which we will perform the Rotation Measure synthesis technique. To combine together the three configurations the task `concat` is needed, which concatenates several visibility data sets into a single Measurement Set (MS).
Given the fact that the single MS have been calibrated and then combined, is necessary to re-calculate the weights for the visibilities, and this is possible thanks to the tasks `initweights`, that provides for initialization of the weight information in the MS, and `statwt`, that computes values for the `WEIGHT` and `WEIGHT SPECTRUM` (if present) columns and/or the `SIGMA` and `SIGMA SPECTRUM` (if present) columns based

on the variance of values in the `CORRECTED DATA` or `DATA column`. The weights are re-scaled by a factor, for the B, C, D configurations respectively,

$$\text{visweightingscale} = [1.0, 0.4225, 0.2927]. \tag{5.1.4}$$

We subtracted the more peripheral sources in order to focus only on the cluster region and speed up the computation time in the following analysis. To do this we firstly need to obtain a model in order to write the `MODEL COLUMN`: this image has been made using the "w-projection", with *wprojplanes = 256*, and a Gaussian taper of 10" (Fig. 5.1). Within the image, we selected a region which contains the cluster and set a zero value for every pixel of the model in the region, and then, with the task `ftw`, we converted this model into model visibilities in the `MODEL COLUMN` of the total MS. At this point, with the task `uvsub`, the models of the sources external to the region are subtracted from the image, with a residual `CORRECTED DATA` column that contains only the visibilities corresponding to the sources within the region. This column was then splitted in order to obtain a final MS with data related only to the cluster area.
This will be our reference MS for the RM synthesis.

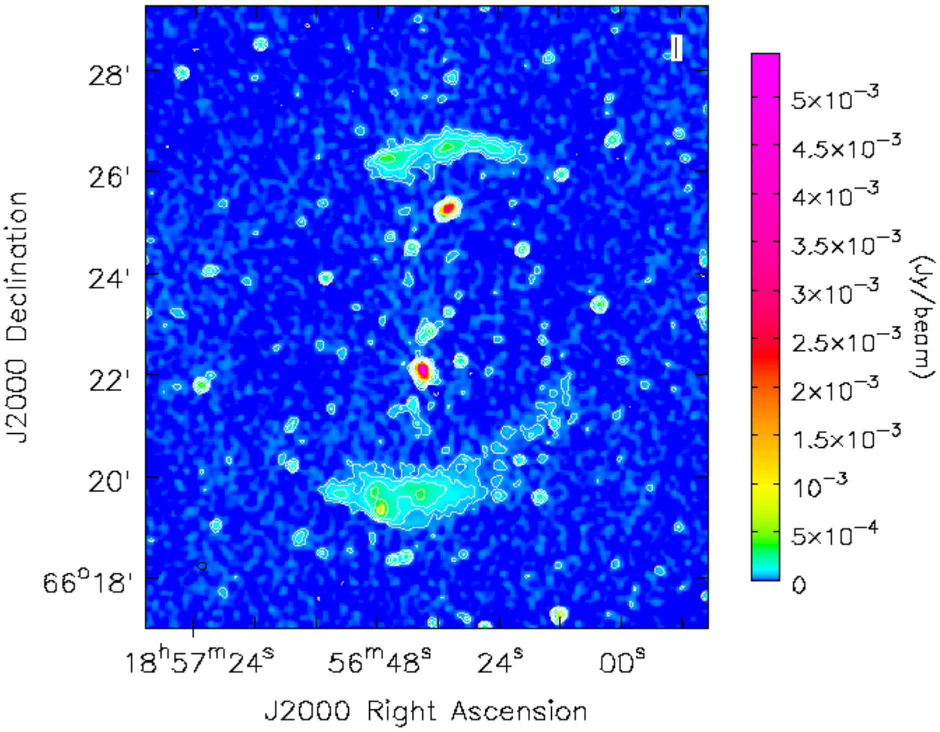

Figure 5.1: Total intensity (Stokes I) image of PSZ2 G096.88+24.18 obtained with VLA at 1.5 GHz (resolution 9.6" $\times$9.2" using a Gaussian taper of 10", RMS noise 12 μJybeam^{-1}) with B, C, D configurations. Contour levels are set at $3\sigma_{rms} \times [1, 2, 4, \ldots]$. Dashed contours represent $-3\sigma_{rms}$.

5.2 Polarization imaging with WSClean

Once our combined dataset has been obtained, we have to prepare the way for the RM synthesis technique, true pivot of this work.
In order to perform this technique, we need to obtain an image cube, whose axes are right ascension (RA), declination (DEC), and frequency. This kind of images can be produced thanks to the `WSClean` (w-stacking clean, Offringa et al., 2014) software. With this software, it is possible to make both a MFS image (putting together all channels) and a cube with an image made for each channel, that is what we need. We produced a cube made by 64 images for I, Q, U Stokes, using a Gaussian taper of 10", as well as a wide-band image. We used 64 images for each cube, which means 4 images for every spectral window, with a bandwidth of 16 MHz per image. This choice is motivated by the fact that, within each channel, we are sensitive to a maximum observable $\phi \sim 655$ rad m^{-2} (see Sec. 5.3.2). This means that we do not have significant bandwidth depolarization within the channels.
This software, contrary to `CASA`, has an "auto-masking" function that allows automated deep cleaning up to a certain threshold limit that can be specified directly in the command. Moreover, it is possible to perform a "multi-scale cleaning" that automatically uses as many scales are necessary. `WSClean` has a special weighting mode, called "multi-frequency weighting", that changes the way in which spectral imaging is performed: in fact, with this task, all weights are gridded on the same grid, and hence the sum of the image cube equals a MF image with the same weighting. Then, the residuals are found in the combined image and deconvolved separately for each channel[2].

The cube of 64 images and the MFS image for the I, Q, U Stokes parameters (Fig. 5.2), produced as explained above, will be the starting point for the polarimetric studies that will constitute the following steps.

5.3 Polarization results

5.3.1 Integrated polarization results

Before going deeper into the polarimetric analysis, we have to prepare the starting images.
We firstly set for all the cubes images the same resolution, which is necessary for the RM synthesis. We chose a common resolution of 13", which corresponds to the one of the first image of the cubes. We did this also for the MFS images, which is the image from the full observed band, in order to be consistent for the comparison of the obtained results.
Then, the MFS images as well as the I, Q, and U imaging cubes, have to be corrected

---

[2] However, using a Briggs weighting, the total weight of a visibility is determined by the number of visibilities that fall into that cell: the fewer visibilities fall into the same cell, the more weight this visibility receives. In order to remove any possible outlier, in the case of an only visibility gridded in a particular (u,v) cell that has a lot of weight, the "weight rank filter" is used because it calculates a local weight RMS of the grid, and truncated all weights that are some factor above the local RMS. This results in very little change in the PSF, but can effect the noise in the image significantly.

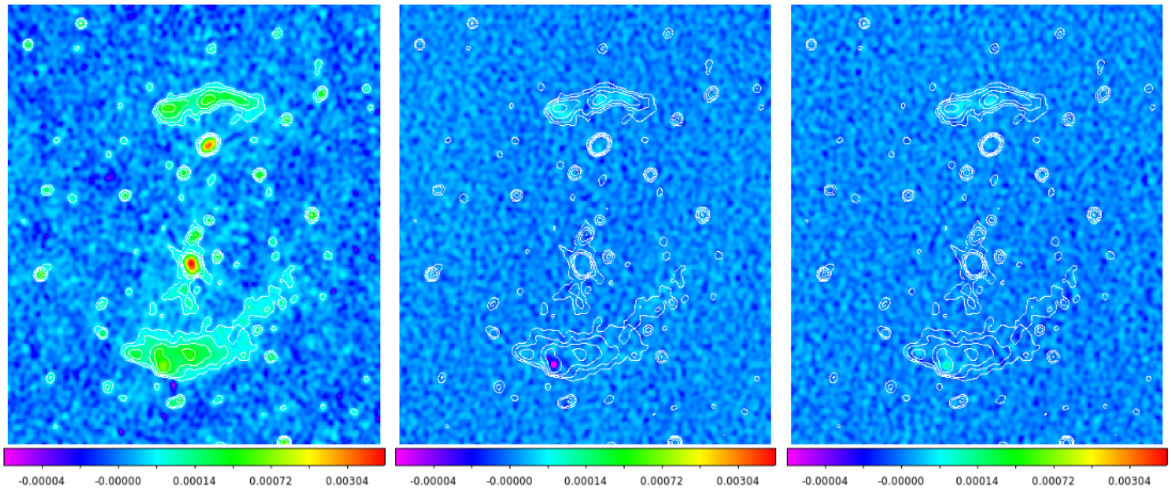

Figure 5.2: From left to right: MFS images obtained with `WSClean` for I, Q, U Stokes parameters, with a Gaussian taper of 10” (resolution: 11.1” ×10.4”). The colorbar represents the flux density in Jy beam^{-1}. The RMS is 1.2×10^{-5}, 7.8×10^{-6}, and 9.2×10^{-6} Jy beam^{-1}, respectively. The white contours represent $3\sigma_{rms,I}\times$ [1,2,4,...] based on the total intensity $\sigma_{rms,I} = 1.2\times10^{-5}$ Jy beam^{-1}. These images are different with respect to the ones obtained with `CASA` because of the different algorithms used for both masking and deconvolution.

for the primary beam (see Sec. 3.2.3). In `CASA`, we can use the task `widebandpbcor` in order to compute a set of PB at the specified frequencies, in our case 64 PBs, corresponding to the ones that constitute the cubes, calculates Taylor-coefficient images that represent the PB spectrum, performs a polynomial division to PB-correct the output Taylor-coefficient images from `tclean` (with nterms=2), and recomputes the spectral index (and curvature) using the PB-corrected Taylor-coefficient images. This set of image represents the PB pattern that is required for the task `impbcor` for the PB correction.
Lastly, within the 64 images of the cube, 8 were removed because the Spw 8 and 9 are completely flagged: the final PB-corrected cube is then composed by 56 images.

In order to obtain the polarization fraction we started to evaluate the ratio between the integrated flux in P and the integrated flux in total intensity I. To do this, we used the MFS images produced with `WSClean` and corrected for the primary beam. To study these polarization properties we selected three regions within both relics within which to calculate the polarization fraction: these regions, nominated “NORTH”, “EAST” and “WEST”, are shown in Fig. 5.3. Particularly, the WEST region has been chosen because our more sensitive data have revealed the presence of highly polarized emission in the western edge of the southern relic not detected by Jones et al. (2021). The polarized flux density P image has been obtained combining the Q and U images and then correcting for the Ricean bias. This correction is needed because of the positivity of the noise in $S_P = \sqrt{U^2 + Q^2}$. In this thesis work, the chosen solution for the Ricean bias correction is the one suggested by Wardle and Kronberg (1974), in which the intrinsic polarized intensity

$$S_P \sim \sqrt{S^2_{P_{obs}} - \sigma^2_{S_P}}. \tag{5.3.1}$$

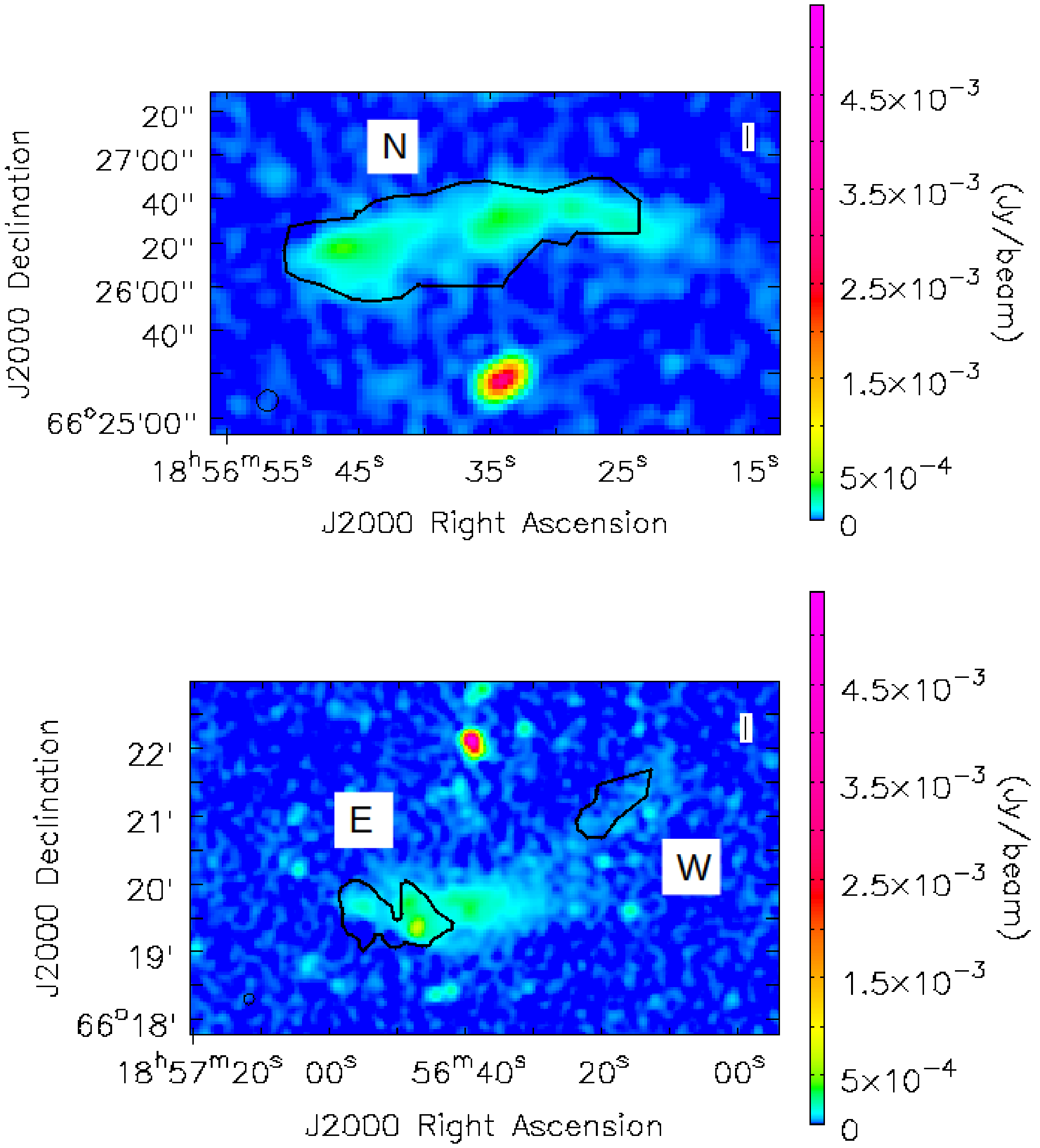

Figure 5.3: Detail of southern relic of PSZ2 G096.88+24.18 with the three regions selected for the polarimetric analysis (black solid lines). These three regions will be nominated "N" for the northern relic (Top), and "E" and "W" for the southern relic (Bottom).

The value σ_{S_P} has been computed considering the average noise level between the Q and U images and is 3×10^{-6} Jy beam^{-1}.
For each region, the flux density in both total intensity I (S_I) and polarized intensity P (S_P) has been obtained, as well as the respective flux error calculated as

$$\sigma_{flux} = \frac{\sigma_{RMS}}{\sqrt{n_{beam}}}, \tag{5.3.2}$$

where $flux = I,\ P$ and n_{beam} is the number of beam contained within the chosen region. In the classical formula, is generally present also the residual calibration error on the flux: however, given that we are interested in the polarization fraction

trend, we can ignore this term because it is a systematic value that affects equally P and I.
We calculate the polarization fraction for both regions as

$$f_{pol} = \frac{S_P}{S_I}, \tag{5.3.3}$$

and the error on the polarization fraction is obtained through the propagation of errors

$$\delta f_{pol} = \sqrt{\left(\frac{1}{S_I}\delta S_P\right)^2 + \left(-\frac{S_P}{S_I^2}\delta S_I\right)^2}. \tag{5.3.4}$$

For the selected regions, given the flux densities listed in Tab. 5.3 for I and P, we obtain respectively

- $f_{pol} = (13.1 \pm 0.1)\%$ for the NORTH region
- $f_{pol} = (7.7 \pm 0.1)\%$ for the EAST region
- $f_{pol} = (27.7 \pm 0.6)\%$ for the WEST region.

The values that we obtained have to be compared to the ones of Jones et al. (2021). In their paper, they found a very low value for the fractional polarization in the southern relic ($\leq 10\%$).
With our analysis, we obtained a compatible value for what concerns the EAST region. This region corresponds nearly to the one from which the polarization fraction was studied in the previously cited article. Hence, we confirm with our deeper and more sensitive data that the integrated polarization in the E region of the relic is lower than usually found. In addition, we detected a polarization fraction of 27.7% at 13" resolution, from a region which was not even detected in the previous works.

5.3.2 RM synthesis technique results

Beside the integrated analysis of polarization, we applied the RM synthesis technique to resolve the in-band depolarization and understand if the low polarization fraction observed in the southern relic can be due to bandwidth depolarization. This technique, as already explained in Sec. 2.4, uses in fact an observing bandwidth splitted up into many individual narrow frequency channels. Adding up the individual channels may cause bandwidth depolarization: however, using the value of Faraday depth that maximize the signal resulting from the coaddition of the polarized flux from all channels, it is possible to recover the polarized flux.
With the RM synthesis technique, it is possible to obtain the reconstructed Faraday spectrum for each pixel, in which this value of $\phi$is evaluated taking into account the sampling characteristics of the observation.

To perform RM synthesis technique on image-frequency cubes we used the `RMsynth3D` tool present in the `RM-tools` software (Purcell et al., 2020). This package takes two input files (Stokes Q and U cubes produced with `WSClean`) and a list of channel frequencies in order to produce, as outputs:

- The dirty FDF, which represents the intrinsic polarized flux, made by three components: the real (Stokes Q), the imaginary (Stokes U), and the amplitude. Starting from the observed polarized flux, given the instrumental characteristics, the software is able to produce the distribution of the intrinsic polarization with respect to the Faraday depth ϕ following Eq. 2.4.4.
- The RMSF, which takes into account the sampling properties of the interferometer, with the same structure as the dirty FDF. In addition it also contains as the 4-th extension a map of the FWHM of the RMSF.
- A map of the maximum polarized intensity in each FDF (e.g., for each pixel).
- A map of the Faraday depth corresponding to the maximum polarized intensity in each FDF. These are the values of ϕ that maximize the polarized flux in each pixel, and consequentially recover polarized signal with respect to the integrate analysis.

These last two products are calculated from the Faraday depth values sampled by the FDF, without interpolation over the discrete channels. Moreover, we also added a list of RMS for each channel (e.g., image of the cube) that can set the weighting scheme.
Using Eq.s 2.4.9 and 2.4.11 we were able to calculate some useful parameters for RM synthesis given the lists of frequencies and RMS, respectively the theoretical FWHM of the RMSF (~ 53 rad m^{-2}) and the maximum observable ϕ (~ 655 rad m^{-2}), as well as the theoretical noise in P, listed in Tab. 5.2:

$$\sigma_P = \frac{1}{\sqrt{\sum_{i=1}^{56} \frac{1}{\sigma^2_{list,i}}}}, \tag{5.3.5}$$

where $\sigma_{list,i}$ are the average RMS values between Q and U images of each channel of the cube.
The range of Faraday depths over which to calculate the FDF is set to be ±1000 rad m^{-2}, while the sample spacing in Faraday depth for the FDF is 3 rad m^{-2}: the wide range in ϕ for the FDF has been chosen in order to use the external intervals to evaluate the noise in each pixel, given that at $|\phi| > 655$ rad m^{-2} we avoid contamination from residual sidelobes of the sources.

Once performed the RM synthesis at 13”, we also “cleaned” the dirty FDF following the description in Sec. 2.4.1. The deconvolution is possible using the package `RMclean3D`, that applies the `CLEAN` algorithm independently to every pixel in a Faraday depth cube. It takes as inputs the total intensity dirty FDF and RMSF, and produces several output files:

- a total and “cleaned” FDF.
- a cube, with the same format as the cleaned FDF, containing the complex clean components found by `CLEAN`.
- a map showing the number of `CLEAN` iterations used for each pixel.

As stopping criteria, a cut-off threshold was set to $8 \times \sigma_P$, following George et al. (2012), which corresponds to a false detection rate of 0.06 % and to a Gaussian significance level of about 7σ according to Hales et al. (2012). For all the RMclean performed, the cut-off threshold was reached.

For the study of the polarization fraction within the southern relic, we need to produce a map of the polarized intensity using the results obtained with the RM synthesis technique. In order to produce this image, we need first of all to compute, for every pixel, the maximum value of the cleaned FDF $S_{P_{obs}}$. Then, it is necessary to correct for the Ricean bias. The value $\sigma^2_{S_P}$, present in Eq. 5.3.1, has been computed considering the average noise level between the real and imaginary cleaned FDF evaluated in the ranges $[-1000, -600]$ rad m^{-2} and $[+600, +1000]$ rad m^{-2} along the Faraday depth axis.

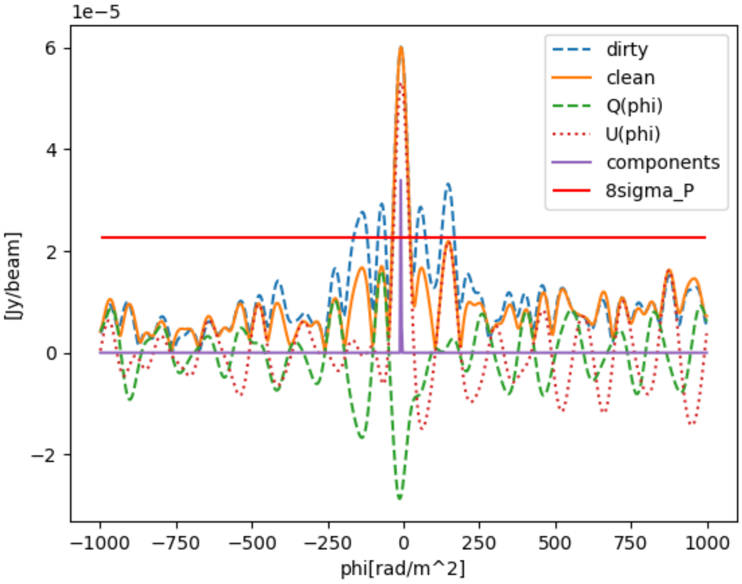

Figure 5.4: An example of the reconstructed FDF deconvolution based on our thesis data. In dashed blue lines we have the "dirty" (original) FDF while in solid range line we see the "cleaned" FDF. We note the reduction of the sidelobes resulting with this technique. In purple we see the selected component relative to the main peak, while the horizontal red line represents the threshold used as a stopping criteria. This cleaned Faraday spectrum has been taken from a pixel in the EAST region of the southern relic.

With respect to the results obtained in the previous Section, here, thanks to the usage of RM synthesis technique, we were able to recover an important fractional polarization in each region chosen for both relics. Given the flux densities and respective errors, listed in Tab. 5.5, we obtained a value of fractional polarization with the RM synthesis technique of

- $f_{pol} = (20.3 \pm 0.1)\%$ for the NORTH region
- $f_{pol} = (13.5 \pm 0.2)\%$ for the EAST region

- $f_{pol} = (51.6 \pm 1.5)\%$ for the WEST region,

using the same Eq.s 5.3.3 and 5.3.4.
We expected this result because of the fact that, with the RM synthesis, the bandwidth depolarization is reduced as much as possible using information on single narrow frequency channels.
For the NORTH region, we obtain a fractional polarization which is typical for radio relics ($\sim 20\%$, Stuardi et al., 2022).
However, even if the polarization fraction increases, it can not account for the low polarization value found in the E region, which remains lower than what is observed in other relics and in relic N. Hence, we will investigate in the next Section the role of beam depolarization.

5.4 Polarization at different resolutions

At this point, our aim is to study if and how the polarization fraction varies with respect to the beamsize. The dimension of the beamsize can be changed using a 2D Gaussian filter kernel on the images that constitute the cube. This kernel is implemented in Python using the `Gaussian2DKernel` function of the `Astropy v5.1` package (Astropy Collaboration et al., 2022), that requires the standard deviation of the Gaussian in pixel, and then the function `convolve` that convolves an array with the Gaussian kernel. All the cubes images have been "smoothed" with this routine, as well as the MFS images, and the values used for the kernel are listed in Tab. 5.2.
For each resolution we performed an analysis of polarization fraction following the routines explained in the previous Section, for both integrated and RM synthesis technique. The results for both total intensity (S_I) and polarized (S_P) flux densities, for both regions selected for the southern relic, are listed in Tab. 5.3 and 5.4, for the integrated analysis and RM synthesis, respectively.

Given these values of flux density, following Eq.s 5.3.3 and 5.3.4, we calculated the trend of polarization fraction with respect to the beamsize. The obtained values are listed in Tab. 5.5 and 5.6 for integrated and RM synthesis analysis, respectively. The fractional polarization as a function of the resolution is showed in Fig. 5.5 and 5.6. We see a decreasing trend, which is expected because we are experiencing beam depolarization as a depolarization mechanism. The plateau that shows up at lower resolutions is related to the fact that the magnetic field turbulent fluctuations within the beam become to be not particularly incisive for large beam sizes.
This trend is what we want to study in order to constrain the characteristics of the magnetic field within the cluster

Beam size	(kpc)	σ_{S_P} (Jy beam^{-1})	Theoretical σ_P (Jy beam^{-1})
13”	57.9	3×10^{-6}	3×10^{-6}
20”	89.0	2×10^{-6}	2×10^{-6}
25”	111.3	2×10^{-6}	1×10^{-6}
30”	133.5	2×10^{-6}	0.9×10^{-6}
35”	155.8	1×10^{-6}	0.7×10^{-6}
40”	178.0	1×10^{-6}	0.6×10^{-6}
45”	200.3	1×10^{-6}	0.5×10^{-6}
50”	222.5	1×10^{-6}	0.4×10^{-6}

Table 5.2: Characteristic of the different smoothed cubes used for the RM synthesis technique. Column 1: beam size for the different Gaussian kernel. Column 2: corresponding dimension in kpc. At the redshift of PSZ2 G096.88+24.18 ($z = 0.3$), 1” corresponds to a linear scale of 4.45 kpc. Column 3: average σ_{S_P} for all images of Stokes Q and U cubes for integrated analysis. Column 4: theoretical noise in P for RM synthesis analysis.

Beam size	Flux density S_I (Jy beam^{-1})	σ_I (Jy beam^{-1})
13”	6.100×10^{-3}	3.0×10^{-5}
20”	5.560×10^{-3}	4.0×10^{-5}
25”	5.139×10^{-3}	4.5×10^{-5}
30”	4.733×10^{-3}	4.9×10^{-5}
35”	4.365×10^{-3}	5.2×10^{-5}
40”	4.047×10^{-3}	5.5×10^{-5}
45”	3.779×10^{-3}	5.7×10^{-5}
50”	3.555×10^{-3}	6.0×10^{-5}

Beam size	Flux density S_I (Jy beam^{-1})	σ_I (Jy beam^{-1})
13”	5.042×10^{-3}	4.8×10^{-5}
20”	4.709×10^{-3}	6.6×10^{-5}
25”	4.440×10^{-3}	7.6×10^{-5}
30”	4.171×10^{-3}	8.4×10^{-5}
35”	3.906×10^{-3}	9.1×10^{-5}
40”	3.673×10^{-3}	9.6×10^{-5}
45”	3.440×10^{-3}	1.00×10^{-4}
50”	3.239×10^{-3}	1.03×10^{-4}

Beam size	Flux density S_I (Jy beam^{-1})	σ_I (Jy beam^{-1})
13”	5.89×10^{-4}	1.2×10^{-5}
20”	5.62×10^{-4}	1.8×10^{-5}
25”	5.40×10^{-4}	2.1×10^{-5}
30”	5.16×10^{-4}	2.4×10^{-5}
35”	4.92×10^{-4}	2.6×10^{-5}
40”	4.68×10^{-4}	2.9×10^{-5}
45”	4.45×10^{-4}	3.1×10^{-5}
50”	4.24×10^{-4}	3.2×10^{-5}

Table 5.3: Flux densities and relative errors measured for the selected regions, “N” (top), “E” (centre), and “W” (bottom). Column 1: beam size for the different Gaussian kernel. Column 2: flux density in total intensity S_I. Column 3: σ_I obtained as seen in Eq. 5.3.2.

Beam size	Integrated $S_{P,int}$ (Jy beam^{-1})	$\sigma_{P,int}$ (Jy beam^{-1})	RM synthesis $S_{P,RM}$ (Jy beam^{-1})	$\sigma_{P,RM}$ (Jy beam^{-1})
13”	7.99×10^{-4}	4×10^{-6}	1.242×10^{-3}	6×10^{-6}
20”	6.99×10^{-4}	5×10^{-6}	1.028×10^{-3}	7×10^{-6}
25”	6.31×10^{-4}	6×10^{-6}	9.37×10^{-4}	8×10^{-6}
30”	5.68×10^{-4}	6×10^{-6}	8.57×10^{-4}	9×10^{-6}
35”	5.14×10^{-4}	6×10^{-6}	7.87×10^{-4}	9×10^{-6}
40”	4.67×10^{-4}	6×10^{-6}	7.25×10^{-4}	1.0×10^{-5}
45”	4.28×10^{-4}	7×10^{-6}	6.68×10^{-4}	1.0×10^{-5}
50”	3.94×10^{-4}	7×10^{-6}	6.24×10^{-4}	1.1×10^{-5}

Beam size	Integrated $S_{P,int}$ (Jy beam^{-1})	$\sigma_{P,int}$ (Jy beam^{-1})	RM synthesis $S_{P,RM}$ (Jy beam^{-1})	$\sigma_{P,RM}$ (Jy beam^{-1})
13”	3.90×10^{-4}	4×10^{-6}	6.79×10^{-4}	6×10^{-6}
20”	3.09×10^{-4}	4×10^{-6}	5.03×10^{-4}	6×10^{-6}
25”	2.63×10^{-4}	4×10^{-6}	4.45×10^{-4}	7×10^{-6}
30”	2.26×10^{-4}	4×10^{-6}	3.96×10^{-4}	7×10^{-6}
35”	1.95×10^{-4}	4×10^{-6}	3.53×10^{-4}	7×10^{-6}
40”	1.71×10^{-4}	4×10^{-6}	3.15×10^{-4}	8×10^{-6}
45”	1.52×10^{-4}	5×10^{-6}	2.86×10^{-4}	8×10^{-6}
50”	1.34×10^{-4}	5×10^{-6}	2.63×10^{-4}	8×10^{-6}

Beam size	Integrated $S_{P,int}$ (Jy beam^{-1})	$\sigma_{P,int}$ (Jy beam^{-1})	RM synthesis $S_{P,RM}$ (Jy beam^{-1})	$\sigma_{P,RM}$ (Jy beam^{-1})
13”	1.63×10^{-4}	3×10^{-6}	3.04×10^{-4}	6×10^{-6}
20”	1.41×10^{-4}	4×10^{-6}	2.02×10^{-4}	6×10^{-6}
25”	1.25×10^{-4}	5×10^{-6}	1.69×10^{-4}	7×10^{-6}
30”	1.11×10^{-4}	5×10^{-6}	1.46×10^{-4}	7×10^{-6}
35”	9.9×10^{-5}	5×10^{-6}	1.27×10^{-4}	7×10^{-6}
40”	8.9×10^{-5}	6×10^{-6}	1.12×10^{-4}	7×10^{-6}
45”	8.1×10^{-5}	6×10^{-6}	1.0×10^{-5}	7×10^{-6}
50”	7.5×10^{-5}	6×10^{-6}	9.1×10^{-5}	7×10^{-6}

Table 5.4: Integrated and RM synthesis polarized flux densities and relative errors measured for the selected regions: “N” (top), “E” (centre) and “W” (bottom). Column 1: beam size for the different Gaussian kernel. Column 2: polarized flux density in integrated analysis $S_{P,int}$. Column 3: $\sigma_{P,int}$ obtained as seen in Eq. 5.3.2. Column 4: polarized flux density with RM synthesis $S_{P,RM}$. Column 5: error on flux density $\sigma_{P,RM}$.

Beam size	$f_{pol} \pm \delta f_{pol}$ NORTH	$f_{pol} \pm \delta f_{pol}$ EAST	$f_{pol} \pm \delta f_{pol}$ WEST
13”	$(13.1 \pm 0.1)\%$	$(7.7 \pm 0.1)\%$	$(27.7 \pm 0.6)\%$
20”	$(12.6 \pm 0.1)\%$	$(6.6 \pm 0.1)\%$	$(25.1 \pm 0.8)\%$
25”	$(12.3 \pm 0.1)\%$	$(5.9 \pm 0.1)\%$	$(23.2 \pm 0.9)\%$
30”	$(12.0 \pm 0.1)\%$	$(5.4 \pm 0.1)\%$	$(21.5 \pm 1.0)\%$
35”	$(11.8 \pm 0.1)\%$	$(5.0 \pm 0.1)\%$	$(20.1 \pm 1.1)\%$
40”	$(11.5 \pm 0.2)\%$	$(4.7 \pm 0.1)\%$	$(19.0 \pm 1.2)\%$
45”	$(11.3 \pm 0.2)\%$	$(4.4 \pm 0.1)\%$	$(18.3 \pm 1.3)\%$
50”	$(11.1 \pm 0.2)\%$	$(4.1 \pm 0.1)\%$	$(17.6 \pm 1.4)\%$

Beam size	$f_{pol} \pm \delta f_{pol}$ NORTH	$f_{pol} \pm \delta f_{pol}$ EAST	$f_{pol} \pm \delta f_{pol}$ WEST
13”	$(20.3 \pm 0.1)\%$	$(13.5 \pm 0.2)\%$	$(51.6 \pm 1.5)\%$
20”	$(18.5 \pm 0.2)\%$	$(10.6 \pm 0.2)\%$	$(35.9 \pm 1.6)\%$
25”	$(18.2 \pm 0.2)\%$	$(10.0 \pm 0.2)\%$	$(31.3 \pm 1.7)\%$
30”	$(18.1 \pm 0.3)\%$	$(9.5 \pm 0.3)\%$	$(28.3 \pm 1.9)\%$
35”	$(18.0 \pm 0.3)\%$	$(9.0 \pm 0.3)\%$	$(25.8 \pm 2.0)\%$
40”	$(17.9 \pm 0.3)\%$	$(8.6 \pm 0.3)\%$	$(23.9 \pm 2.1)\%$
45”	$(17.7 \pm 0.4)\%$	$(8.3 \pm 0.3)\%$	$(22.5 \pm 2.2)\%$
50”	$(17.5 \pm 0.4)\%$	$(8.1 \pm 0.4)\%$	$(21.5 \pm 2.3)\%$

Table 5.5: Polarization fractions and relative errors measured for the selected regions for different resolutions. Top: values for the integrated analysis. Bottom: values for RM synthesis technique analysis.

Column 1: beam size for the different Gaussian kernel. Column 2: polarization fraction for region NORTH and associated error, obtained as seen in Eq. 5.3.4. Column 3: same as Column 2 but for EAST region. Column 4: same as Column 2 but for WEST region.

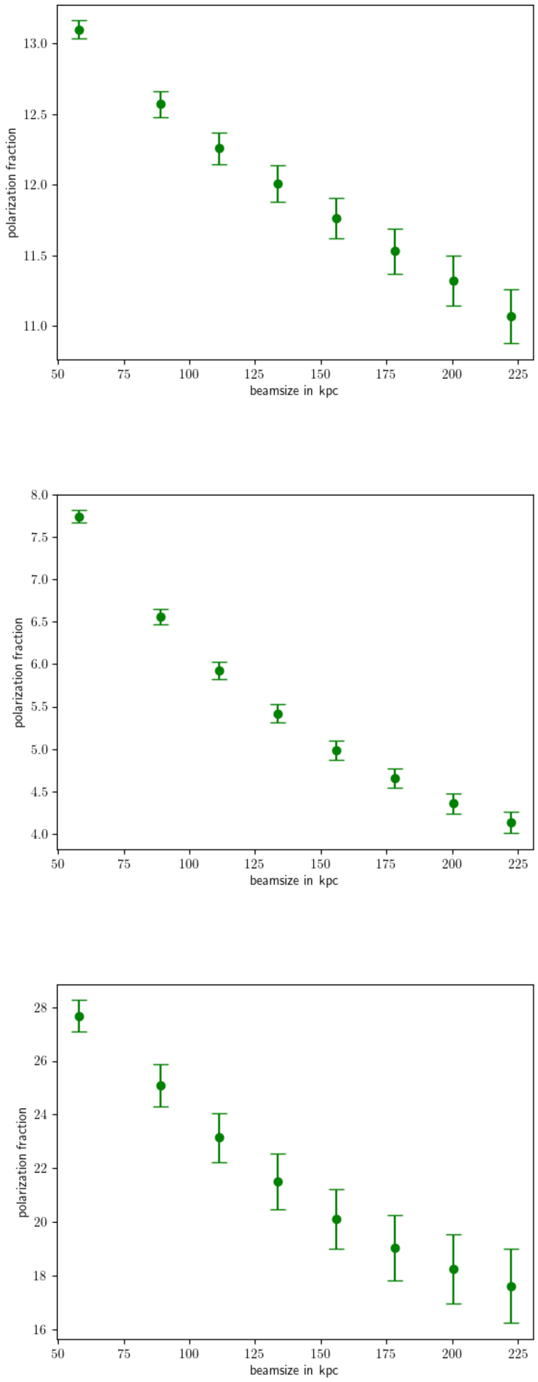

Figure 5.5: Trend of polarization fraction with respect to the beam size for the results obtained through integrated analysis.
Top: NORTH region. Centre: EAST region. Bottom: WEST region.
The plotted values, as well as the relative errors, are listed in Tab 5.5.

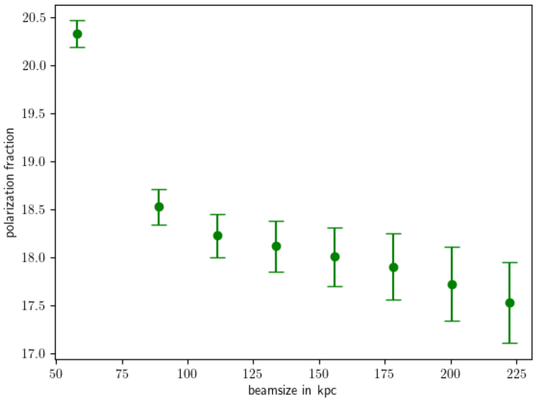

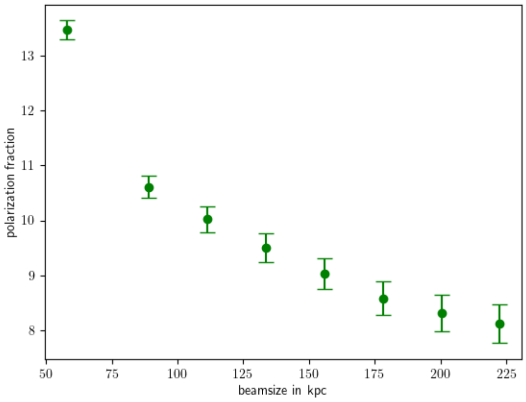

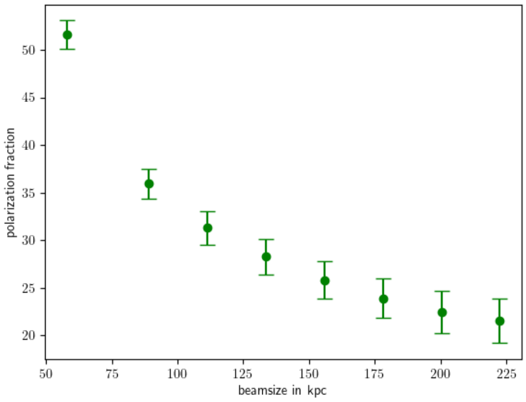

Figure 5.6: Trend of polarization fraction with respect to the beam size for the results obtained through RM synthesis technique.
Top: NORTH region. Centre: EAST region. Bottom: WEST region.
The plotted values, as well as the relative errors, are listed in Tab 5.5.

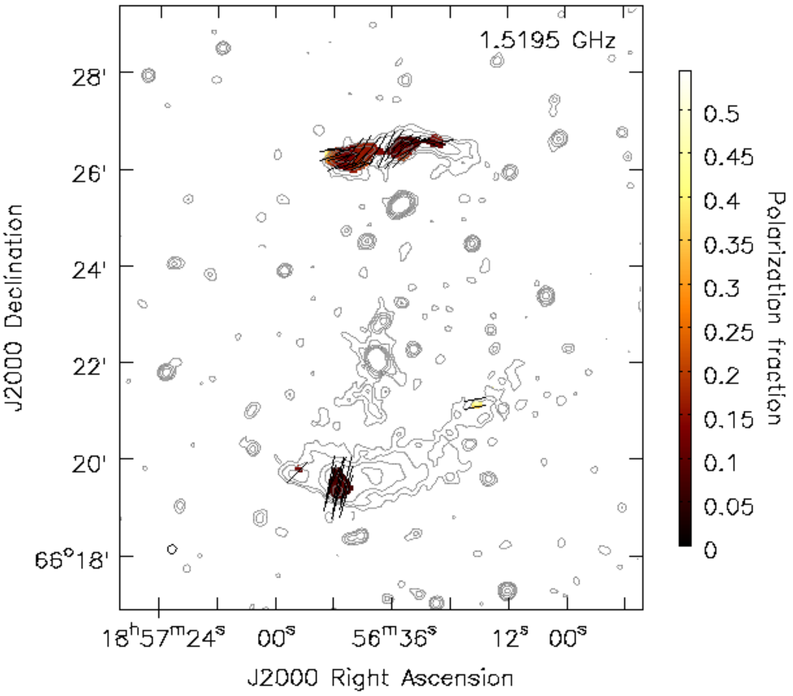

Figure 5.7: Polarization fraction (in color scale) as obtained for RM synthesis technique at resolution of 13". The contours (grey) are the same as described in Fig. 5.2, while the black lines represent the orientation of magnetic field vectors corrected for the galactic contribution of -4.5 rad m^{-2}.

Chapter 6

Simulations results and discussion

In this Chapter, we describe the 3D magnetic field simulations that we have made in order to constrain the magnetic field in front of the southern relic of PSZ2G096.88+24.18. We simulate magnetic fields with different spectra and derive the polarization fraction expected for different resolutions. Then, we compare these trends with observations to constrain the magnetic field spectrum. This last Chapter is divided in two different parts.
In the first one, the characteristics of the simulations used in this thesis work are presented and the more "operative" part is described.
Secondly, we will compare the observations with the simulations and discuss the results, also in terms of what is observed with polarization analysis in other clusters.

6.1 Magnetic field modeling

The determination of the cluster magnetic field properties from the RM measurements relies on the knowledge of, both, the thermal electron density and the magnetic field structure (see Eq. 1.2.19). In order to avoid simplistic assumptions, often used to solve the integral in Eq. 1.2.19, we produced synthetic RM maps by taking into account 3D models of the thermal electron density and of the magnetic field of a galaxy cluster. These RM maps can then directly be compared to observations, where the magnetic field model parameters can be constrained with a statistical approach. The necessity of producing RM maps is due to the fact that RM can cause also beamw depolarization, in case the turbulent magnetic field is changing within the observing beam.
This method has been applied in other works, like Bonafede et al. (2013) for Coma cluster or Stuardi et al. (2021) for Abell 2345, but, to our knowledge, it has never been applied for the variation of polarization fraction with respect to the resolution.

6.1.1 Simulations of RM maps

In order to produce a simulated distribution of thermal electrons and magnetic field we used a modified version of the MiRo code described in Bonafede et al. (2013). We present here in detail the different steps.

1. The code firstly uses a mock 3D thermal electron density distribution, that comes from MHD simulations in Domínguez-Fernández et al. (2019), of a merging clusters system. This simulation had a resolution of 16 kpc at z=0.02: it has been then re-scaled in order to adapt to our resolution.
   The two simulated X-ray clumps have a projected distance of ~ 900 kpc, more that observed in Finner et al. (2021), with a 1:1 mass ratio of the merging subclusters.
   Originally, our intention was to use X-ray observations in order to constrain the thermal electron density distribution (as described in Sec. 1.1.2): however, no useful information has been obtained.
   Other inputs were the size of the simulated box (512^3 pixels) and the cell resolution (8 kpc size, so $\sim 4^3$ Mpc^3 sampled).

2. Then, it produces a 3D distribution of the magnetic field, based on an analytical power spectrum within a fixed range of scales.
   A Kolmogorov power-law spectrum is used
   $$E_B \propto k^{-11/3} \tag{6.1.1}$$
   where $k = \sqrt{\sum_i k_i^2}$ (with i=1, 2, 3) is the wavenumber corresponding to the physical scale of the magnetic field fluctuations (e.g., $\Lambda \propto 1/k$). The power spectrum represents the magnetic field energy density (erg cm^{-3}) associated with each wavenumber.
   In order to obtain a divergence-free turbulent magnetic field, with this power spectrum, we first selected the corresponding power spectrum for the vector potential $\tilde{\mathbf{A}}(\mathbf{k})$ in Fourier space (Murgia et al., 2004, Tribble, 1991). For each pixel, in Fourier space, the amplitude, $A_{k,i}$, is taken from a Rayleigh distribution in order to have a Gaussian behaviour, and the phase of each component of $\tilde{\mathbf{A}}(\mathbf{k})$ is randomly drawn in range $[0,2\pi]$. The magnetic field vector in Fourier space is then $\tilde{\mathbf{B}}(\mathbf{k}) = i\mathbf{k} \times \tilde{\mathbf{A}}(\mathbf{k})$ and has the desired power spectrum. $\tilde{\mathbf{B}}(\mathbf{k})$ is transformed back into real space using an inverse Fast Fourier Transform (FFT) algorithm. The resulting magnetic field, $\mathbf{B}$, has components B_i following a Gaussian distribution, with $\langle B_i \rangle = 0$ and $\sigma^2_{B_I} = \langle B_i^2 \rangle$.
   The radial profile of the magnitude of the magnetic field is expected to scale with the thermal electron density (as seen in Sec. 1.2.2). This radial decrease of the magnetic field strength is also observed by MHD simulations (e.g. Domínguez-Fernández et al., 2019, Vazza et al., 2018). Therefore, we imposed that the cluster magnetic field scales with the thermal electron density following a power-law
   $$|B(r)| \propto n_e(r)^\eta, \tag{6.1.2}$$
   where η is a free parameter that we fixed to be 0.5, as obtained in Bonafede et al. (2010), which we expect if the energy in the magnetic field scales as the energy in the thermal plasma (assumed to be isothermal).
   The magnetic field is scaled by the density profile and then normalized for a value B_{mean} over the entire box. Hence, the generated cluster magnetic field is tangled on both small and large scales, and it decreases radially.

3. Finally, the code computes the cluster 2D RM map integrating the thermal electron density and magnetic field profile along one axis, solving Eq. 1.2.19, from the centre of the cluster, thus assuming that the sources lie on the plane parallel to the plane of the sky and crossing the cluster centre.
   As final products, this code produces a cube with three 2D maps of projected thermal electron density, magnetic field, and RM, respectively (Fig. 6.1).

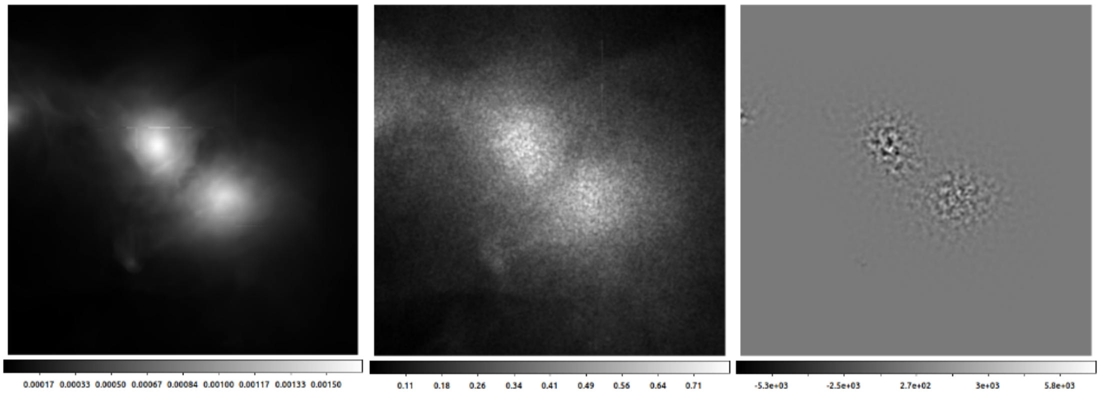

Figure 6.1: Final products of MiRo code for a combination of $B_{mean} = 0.5$ μG, $\Lambda_{min} = 45$ kpc and $\Lambda_{max} = 150$ kpc. Left: 2D map of thermal electron density (in particles cm^{-3}). Centre: 2D map of magnetic field (in μG). Right: 2D map of RM (in rad m^{-2}).

6.1.2 Determination of the simulations parameters

Our magnetic field model considers a total of three free parameters, that can be finally determined comparing with our observations, namely Λ_{min}, Λ_{max}, and B_{mean}, or rather the range of scales over which the Kolmogorov power spectrum is defined and the mean magnetic field used for the normalization within each cell. We want to find the combination of parameters that can better match the observed trend of the polarization fraction with beamsize.

From the simulated RM map produced as explained before, we selected a region with dimensions and position corresponding to the ones of the southern relic (presented in Ch. 4) in order to reproduce it. Within this "simulated" relic, the polarization analysis is performed.

In order to reduce the possible combination of parameters, we decided to fix the normalization value B_{mean} in order to reproduce the equipartition magnetic field at the relic position, found for the southern relic following Eq.s 1.2.14 and 1.2.15 (Govoni and Feretti, 2004), with the following assumptions:

- a depth intermediate between length and height, so 830 kpc;
- a radio brightness at 1.5 GHz of $S_{1.5} = 7.37 \times 10^{-4}$ mJy arcsec^{-2} with an $\alpha = 1.17$ (values taken from Jones et al., 2021);
- $k = 1$ as parameter describing the plasma nature, which means that the plasma is composed by electrons and protons with the same energy content;

- $\xi(\alpha, \nu_1, \nu_2) = 3.42 \times 10^{-13}$, as listed in Tab. 1 from Govoni and Feretti (2004).

The equipartition magnetic field found for the southern relic is 0.69 μG. The value of B_{mean} that is able to reproduce this value in the southern relic region is $B_{mean} = 0.5$ μG. This has been fixed to minimize the number of free parameters in our models. Once B_{mean} is fixed, we are left with two free parameters (Λ_{min} and Λ_{max}). Recalling Eq. 1.2.19, we can see that a variation of ϕ, and so of the polarization characteristics, can be due to both thermal electron density and magnetic field variations.

For the simulation of the polarization fraction at different beamsizes we have used the 2D RM map produced by the MiRo code. For a fair comparison with the observations, we "smoothed" the RM map firstly with a Gaussian kernel of 10", because this was the value with which the `WSClean` images were produced, and then we smoothed the maps a second time with the resolutions used for the data, reported in Tab. 5.2, as we did in Sec. 5.4.

This "depolarization" has been performed using a modified version of a code for the magnetic field modelling presented in Osinga et al. (2022)[3]. This code takes as input the 2D RM simulated map. In order to compute the simulated fractional polarization, we have to assume an intrinsic distribution of the polarization vectors for every pixel of our simulated RM map. We assume an intrinsic polarization angle $\chi_0 = 45°$, so given the RM values in any pixel produced by the simulation, we obtain observed polarization angles given by Eq. 1.2.21. We also need to assume an intrinsic polarized flux density in P, with a $P_{int} = 1$ Jy beam^{-1} chosen.

While the assumption on the polarization angle will be deleted by the Faraday rotation effect, this assumption on the intrinsic polarized flux density is important, because it determines the final value of P/P_{int} that will be compared with the data. Once obtained these two quantities, we can convert them to Stokes Q and U images using the following relations

$$P = \sqrt{Q^2 + U^2} \quad , \quad \chi = \frac{1}{2} \arctan \frac{U}{Q} \tag{6.1.3}$$

which we can convert to

$$Q = \pm \sqrt{\frac{P^2}{1 + \tan^2(2\chi)}} \quad , \quad U = \pm \sqrt{P^2 - Q^2}, \tag{6.1.4}$$

using the convention that Stokes Q is positive for $-\pi/2 \leq \chi \leq \pi/2$ and Stokes U is positive for $0 \leq \chi < \pi$.

The Q and U simulated images have been smoothed, as explained above, and from them the maps of polarized intensity over the intrinsic one are obtained at different resolutions (see for example Fig. 6.2).

From these maps, we obtained the simulated polarization fraction at different resolutions within the region correspondent to the southern relic as

$$f_{pol,SIM} = \frac{P}{P_{int}}. \tag{6.1.5}$$

---

[3] https://github.com/ErikOsinga/magneticfields.

For the magnetic field, we want to determine maximum and minimum scale of the Kolmogorov power spectrum that reproduce the polarization properties observed in the southern relic. From Jones et al. (2021), assuming that the turbulence is generated by the merger shock, the fraction of kinetic energy flux converted to turbulent energy, η, is given by $\frac{1}{2}\eta\rho_u v_s^3 \sim \rho_d \delta v_0^2 v_d$, where ρ_u and ρ_d are the upstream and downstream ICM densities respectively, v_s and v_d the shock and downstream velocities and δv_0 the turbulent velocity at the injection scale. This injection scale L_0 was found to be $\sim$ 100 kpc. Generally, an injection scale of $100 - 400$ kpc is typical for the ICM (Brunetti and Jones, 2014).
In this thesis work we want to constrain the scales over which the turbulence of the ICM is acting that allow to reproduce the observed polarization properties.

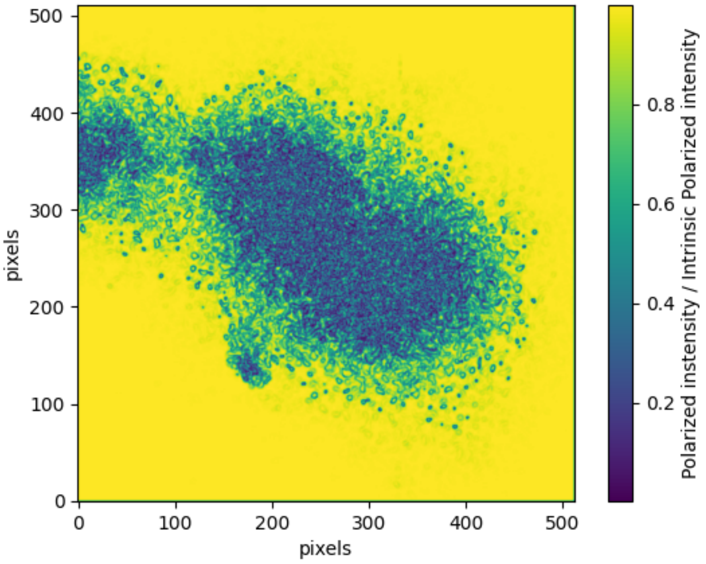

Figure 6.2: 2D smoothed map at 13" of polarized intensity over intrinsic polarized intensity, resulting from depolarization code presented in Osinga et al. (2022).

6.2 Results and discussion

We computed a simulated polarization trend for every combination of the scales listed in Tab. 5.2, with a $B_{mean} = 0.5$ μG and $\eta = 0.5$. In order to compare the simulations with the observations we perform a "reduced" chi-squared test

$$\chi^2_{dof} = \frac{1}{\text{d.o.f.}} \sum_{k=1}^{8} \frac{(O_k - E_k)^2}{\sigma_k^2}, \tag{6.2.1}$$

where O_k are the observed values, σ_k the relative error, and E_k the simulated data. In the denominator there is the number of degrees of freedom, which is given by the subtraction between the number of data points (8, here represented by k) and the number of free parameters (2, Λ_{min} and Λ_{max}). In our case, given that we have 6 d.o.f., we will use the notation χ^2_6.

The aim is to find what combination of scales minimize the reduced chi-squared value, which generally gives a good fit at values around the unity.

We decided to start to produce simulated RM maps combining a Λ_{min}=[16, 24, 32, 40, 45, 50] kpc and a Λ_{max}=[50, 100, 150, 200, 250] kpc, in order to understand on which scales the merger induced turbulence is acting within PSZ2 G096.88+24.18. The smaller scale (16 kpc) has been chosen in order to sample properly (about four times in this case) the higher resolution beamsize (13", so 57.9 kpc): from there, we increased the scales in order to find a best-fit for our simulations.

From the simulation we obtain the ratio between P and the intrinsic value P_{int}, which was assumed to be 1 Jy beam^{-1}: this means that we are not able to obtain information on the intrinsic polarized flux density, that depends only on our assumption, and so not on the intrinsic polarization fraction. In order to compare the observed and the simulated data we need then to find a common landmark for the polarization fraction.

Our choice is to normalize the values of fractional polarization with the one at 13", for each combination of scales, as well as for the observed data. This normalization corresponds to the assumption of an intrinsic polarization fraction at 13" of 20%: this value, besides being a common average value for radio relics (Stuardi et al., 2022), is strengthened by what has been observed for the northern relic (Fig. 5.6).

The error for each beamsize is the standard error

$$\sigma_{sim} = \frac{\sigma_{std}}{\sqrt{n_{beam}}}, \tag{6.2.2}$$

where σ_{std} is the standard deviation and n_{beam} is the number of beam within the selected region for each resolution. This error has been chosen in order to be consistent with the error calculated for the observed data.

This normalization affects also the errors on the observed polarization fraction (which determine the chi-squared value) and the simulated one.

6.2.1 Polarization results in the E and W regions of the relic

For the eastern region of the southern relic the reduced chi-squared results are presented in Fig. 6.3. From the plot we can see the presence of a minimum, with a reduced χ^2_6 of 3.38, corresponding to a Λ_{min} = 45 kpc and Λ_{max} = 150 kpc. This value of χ^2_6, taking into account the 6 degrees of freedom, stands within a significance that, in Gaussian terms, corresponds to $3 - 3.5\sigma$.

However, together with this absolute minimum, there are also two other significant results, two secondary minimum values with different combination of parameters.

- At $\Lambda_{min} = 45$ kpc and $\Lambda_{max} = 100$ kpc there is a reduced χ^2 of 3.56.
- At $\Lambda_{min} = 24$ kpc and $\Lambda_{max} = 150$ kpc there is a reduced χ^2 of 3.66.

both these values are within $4 - 4.5\sigma$ in Gaussian terms.

In Fig. 6.4 we can see the depolarization trend for the EAST region of the southern relic for both observations and simulations for the three minima discussed. We see that, for all cases, the central resolutions are the best reproduced by the simulations,

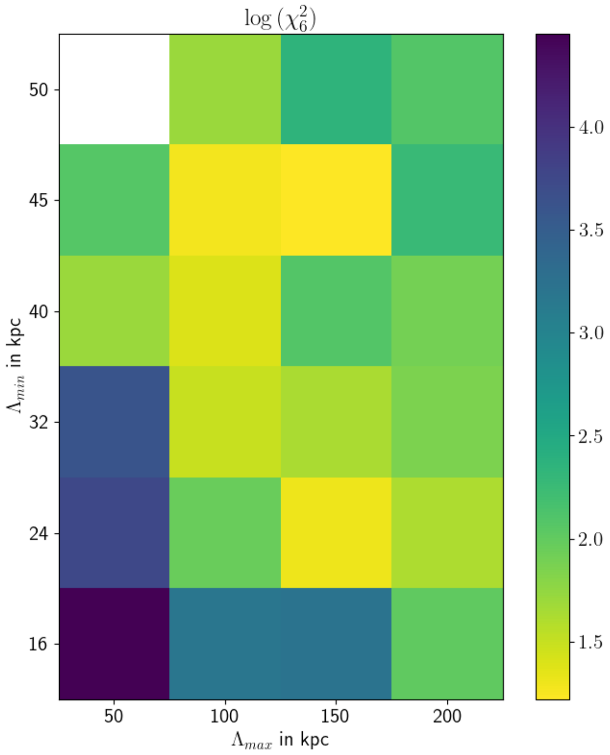

Figure 6.3: The reduced chi-squared value, in logarithmic scale, for the region EAST is represented for each combination of Λ_{max} and Λ_{min}. The white squares represent combinations of scales for which simulations have not been performed.

but in general the two trends are compatible within the errors of both observations and simulations.

From Fig. 6.4, we see that the data match the model predictions, once the errors of both data and simulations are considered. Hence, though more complex for the magnetic field could be considered and give a better χ^2 value, the modeling presented here can explain the depolarization trend observed in the E region of southern relic with a good approximation.

The resulting average magnetic field intensity, given the best fit combination of parameters for E region (corresponding to $B_{mean} = 0.5\ \mu$G, $\Lambda_{min} = 45$ kpc and $\Lambda_{max} = 150$ kpc) is

- $B = 2.15\ \mu$G within 100 kpc^3 from the centre of southern subcluster.
- $B = 1.31\ \mu$G within 1 Mpc^3 from the centre of southern subcluster

The average magnetic field evaluated within 1 Mpc^3 is consistent with the value found, within the same distance, for Abell 2345 in Stuardi et al. (2021).

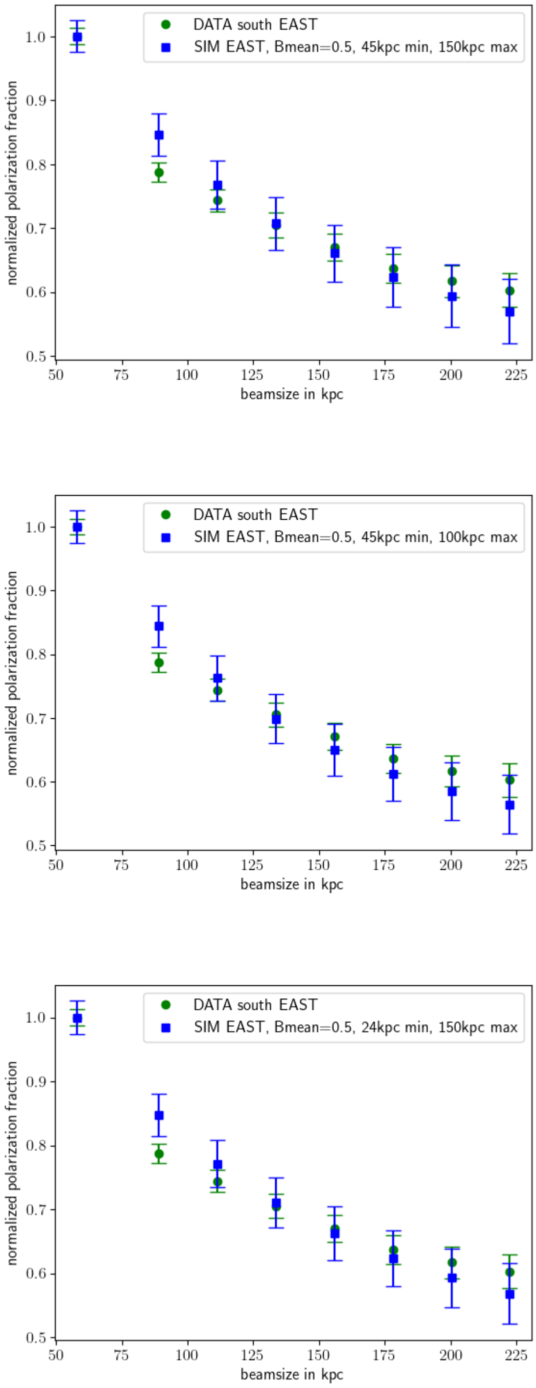

Figure 6.4: Trend of polarization fraction, normalized at 13”, with respect to the beamsize for both data (in green) and simulations (in blue) for the EAST region. These plots are related to the three combinations which show the best values of reduced χ^2_6 presented in Sec. 6.2.1 .
Top: $\Lambda_{min} = 45$ kpc, $\Lambda_{max} = 150$ kpc. Centre: $\Lambda_{min} = 45$ kpc, $\Lambda_{max} = 100$ kpc. Bottom: $\Lambda_{min} = 24$ kpc, $\Lambda_{max} = 150$ kpc.

In Fig. 6.5 we show the values of reduced χ^2_6 obtained for the WEST region of the southern relic.
Here the absolute minimum is better identified in a combination of $\Lambda_{min} = 45$ kpc and $\Lambda_{max} = 200$ kpc, that gives a reduced χ^2_6 of 12.76 with a correspondent Gaussian significance within 5σ. With respect to the eastern region, here we can clearly see a worse fit given by our simulations, both from χ^2_6 and Fig. 6.6, where a net difference between data and simulations is displayed.
Given that it seems to affect the whole trend, it could be probably be reduced by increasing the value of B_{mean} used for the normalization. This means that, for the western region, the magnetic field value should be different from the equipartition value assumed for B_{mean}.

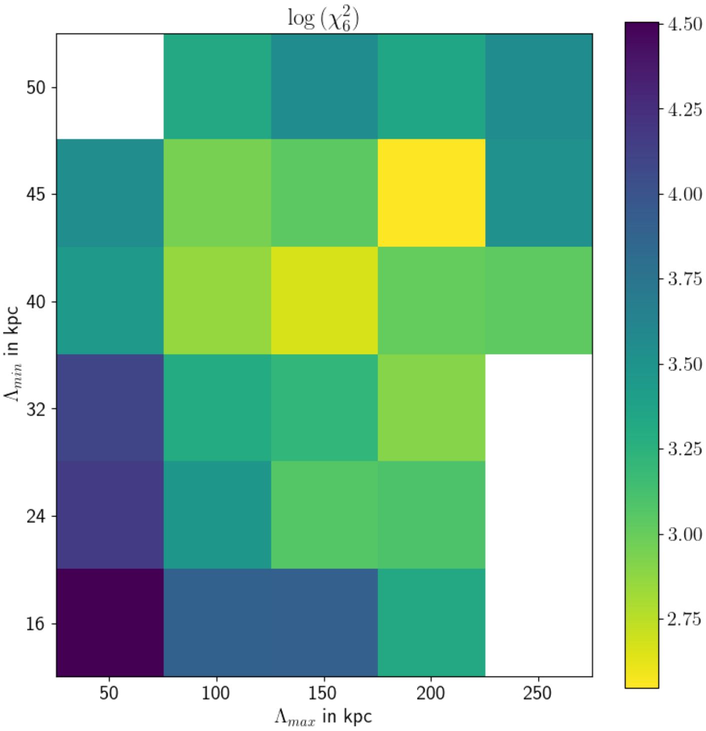

Figure 6.5: The reduced chi-squared value, in logarithmic scale, for the region WEST is represented for each combination of Λ_{max} and Λ_{min}. The white squares represent combinations of scales for which simulations have not been performed.

The E region is characterized by smaller magnetic field scales with respect to the W: this can be a possible explanation for the different polarization properties observed. In fact, bigger scales imply less significant fluctuations of the turbulent magnetic field within the beamsize, and so less beam depolarization.

Given the different positions of the two regions within the cluster, with the E region closer to the southern X-ray clump with respect to the W one, we expect that these different polarization properties can be due to different external depolarization from

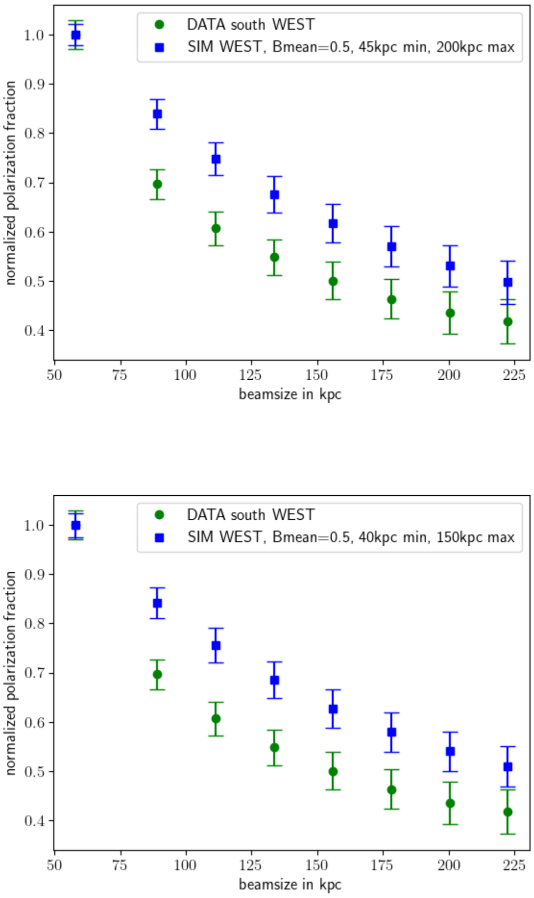

Figure 6.6: Trend of polarization fraction, normalized at 13", with respect to the beamsize for both data (in green) and simulations (in blue) for the WEST region. These plots are related to the three combinations which show the best values of reduced χ^2_6 presented in Sec. 6.2.1 . Top: Λ_{min} = 45 kpc, Λ_{max} = 200 kpc. Bottom: Λ_{min} = 40 kpc, Λ_{max} = 150 kpc.

the cluster ICM distribution. In this scenario, the W region would be located closer to the observer along the line of sight with respect to the E region of the southern relic. The polarized radiation from E should then cross more magnetized plasma, with a consequent increment of depolarization (Eq. 1.2.19). In order to confirm this scenario, we would need more detailed information on the gas distribution within the cluster, for example through a sophisticated modeling of the present X-ray observations.

Chapter 7

Conclusion and future perspectives

The goal of this thesis work was to understand the nature of the low polarization fraction found in previous works in the southern relic of the cluster PSZ2 G096.88+24.18. In fact, this relic showed peculiar features, such as low polarization fraction ($f_{pol} \leq 10\%$), contrary to what is commonly found in other relics, that are polarized up to 60% and show an average $f_{pol} \sim 20\%$.
For this thesis work, we used both archival and new JVLA observations in L-band, in B, C, and D array, in order to have both better angular resolution and sensitivity to extended emission than previous studies. We performed a self-calibration of the three datasets and combined them into one, in order to make the imaging. Using the combined dataset, we have performed our polarimetric analysis.
First of all, we selected two different regions for the southern relic (E and W regions). Within these two regions, calculating the observed polarization fraction with our improved observations, we found for the E region a value around 7%, while for the western edge of the relic, a value of almost $\sim 28\%$.
The EAST results are in line with what found by Jones et al. (2021), but still under the average value expected from radio relics. The WEST region, instead, has never been highlighted in previous works, and shows a good fractional polarization.

Starting from these results, we performed the RM synthesis technique. Using this technique, we can solve the bandwidth depolarization, and detect a higher polarized flux. In fact, using the value of Faraday depth that maximizes the polarized signal, it is possible to recover polarized flux, even if we work with narrow frequency channels.
With the RM synthesis, we have detected a higher polarization fraction of $\sim 13\%$ for the E region, and $\sim 51\%$ for the W.
This fractional polarization in higher with respect to the integrated analysis, but for the EAST region it is still under the average. Given these evidences, we wanted to understand if there is an effect of external depolarization and what configurations of magnetic field can cause it.

In order to constrain the properties of the magnetized plasma which is causing

the depolarization, we studied the trend of polarization fraction with respect to the resolution, that we changed with a Gaussian kernel. These trends, shown in Fig. 5.6, suggest the presence of beam depolarization which is acting on the radiation that comes from the relic.
We used these results to constrain the characteristic scales of magnetic field. We made 3D simulations of magnetic fields within the cluster using a Kolmogorov power spectrum, with variable range of scales, and a value of $B_{mean} = 0.5\ \mu$G for the in-cell normalization, in order to reproduce, at the relic position, the equipartition magnetic field of $B_{eq} = 0.69\ \mu$G. For the thermal electron density distribution, we used instead MHD cosmological simulations of a merging cluster, taken from Domínguez-Fernández et al. (2019). With these information, we produced 2D simulated RM maps at different resolutions, to be compared with the ones of observed polarization obtained using the RM synthesis technique.
The results of the simulation-data comparisons are shown in Fig. 6.4 and 6.6. In order to quantify the goodness of the fit, we performed a reduced chi-squared test, whose results are shown in Fig. 6.3 and 6.5.
We found, as best fit scales combination

- EAST region: $\Lambda_{min} = 45$ kpc, $\Lambda_{max} = 150$ kpc.
- WEST region: $\Lambda_{min} = 45$ kpc, $\Lambda_{max} = 200$ kpc.

The simulations are not in perfect agreement with the observations, especially for the W region. This could indicate that the model of magnetic field can be different with respect to the one assumed (with different power spectrum or normalization).
The average magnetic field within 1 Mpc from the centre of the southern X-ray clump is $\langle B_{1Mpc^3} \rangle = 1.3\ \mu$G, in agreement with values found in other clusters (e.g. Stuardi et al., 2021).

With these results, we found that the low polarization that characterizes the EAST region of the southern relic in PSZ2 G096.88+24.18 can be explained by external depolarization due to the magnetized ICM.
In the E and W regions, we detect different polarization fractions, that could be due to a different position or orientation of the relics along the line of sight: the emission from the E region could pass through a denser medium, as it is closer to the southern X-ray clump with respect to the W region, and/or it could be located closer to the observer along the line of sight than the W region.
Both these effects would produce a higher Faraday rotation (Eq. 1.2.19), and a more pronounced beam depolarization.
A sophisticated analysis of X-ray emission can confirm if the different polarization properties between the two relics are due to the different distribution of gas along the line of sight. PSZ2 G096.88+24.18 has however a complex structure, in which is difficult to determine the centre.
Another possibility is to use simulations for the true structure of the relic, given that, due to projection effects, is difficult to determine the exact geometry of their structure within the clusters.

These can be suggestions for future implementations of this thesis work.

Bibliography

R. Adam, H. Goksu, S. Brown, L. Rudnick, and C. Ferrari. γ-ray detection toward the Coma cluster with Fermi-LAT: Implications for the cosmic ray content in the hadronic scenario. *Astronomy and Astrophysics*, 648:A60, Apr. 2021. doi: 10.1051/0004-6361/202039660.

F. Andrade-Santos, C. Jones, W. R. Forman, L. Lovisari, A. Vikhlinin, R. J. van Weeren, S. S. Murray, M. Arnaud, G. W. Pratt, J. Démoclès, R. Kraft, P. Mazzotta, H. Böhringer, G. Chon, S. Giacintucci, T. E. Clarke, S. Borgani, L. David, M. Douspis, E. Pointecouteau, H. Dahle, S. Brown, N. Aghanim, and E. Rasia. The Fraction of Cool-core Clusters in X-Ray versus SZ Samples Using Chandra Observations. *Astrophysical Journal*, 843(1):76, July 2017. doi: 10.3847/1538-4357/aa7461.

M. Arnaud and A. E. Evrard. The L_X-T relation and intracluster gas fractions of X-ray clusters. *Monthly Notices of the Royal Astronomical Society*, 305(3): 631–640, May 1999. doi: 10.1046/j.1365-8711.1999.02442.x.

M. Arnaud, R. Rothenflug, O. Boulade, L. Vigroux, and E. Vangioni-Flam. Some constraints on the origin of the iron enriched intra-cluster medium. *Astronomy and Astrophysics*, 254:49–64, Feb. 1992.

Astropy Collaboration, A. M. Price-Whelan, P. L. Lim, N. Earl, N. Starkman, L. Bradley, D. L. Shupe, A. A. Patil, L. Corrales, C. E. Brasseur, M. Nöthe, A. Donath, E. Tollerud, B. M. Morris, A. Ginsburg, E. Vaher, B. A. Weaver, J. Tocknell, W. Jamieson, M. H. van Kerkwijk, T. P. Robitaille, B. Merry, M. Bachetti, H. M. Günther, T. L. Aldcroft, J. A. Alvarado-Montes, A. M. Archibald, A. Bódi, S. Bapat, G. Barentsen, J. Bazán, M. Biswas, M. Boquien, D. J. Burke, D. Cara, M. Cara, K. E. Conroy, S. Conseil, M. W. Craig, R. M. Cross, K. L. Cruz, F. D'Eugenio, N. Dencheva, H. A. R. Devillepoix, J. P. Dietrich, A. D. Eigenbrot, T. Erben, L. Ferreira, D. Foreman-Mackey, R. Fox, N. Freij, S. Garg, R. Geda, L. Glattly, Y. Gondhalekar, K. D. Gordon, D. Grant, P. Greenfield, A. M. Groener, S. Guest, S. Gurovich, R. Handberg, A. Hart, Z. Hatfield-Dodds, D. Homeier, G. Hosseinzadeh, T. Jenness, C. K. Jones, P. Joseph, J. B. Kalmbach, E. Karamehmetoglu, M. Kałuszyński, M. S. P. Kelley, N. Kern, W. E. Kerzendorf, E. W. Koch, S. Kulumani, A. Lee, C. Ly, Z. Ma, C. MacBride, J. M. Maljaars, D. Muna, N. A. Murphy, H. Norman, R. O'Steen, K. A. Oman, C. Pacifici, S. Pascual, J. Pascual-Granado, R. R. Patil, G. I. Perren, T. E. Pickering, T. Rastogi, B. R. Roulston, D. F. Ryan, E. S. Rykoff, J. Sabater, P. Sakurikar, J. Salgado,

A. Sanghi, N. Saunders, V. Savchenko, L. Schwardt, M. Seifert-Eckert, A. Y. Shih, A. S. Jain, G. Shukla, J. Sick, C. Simpson, S. Singanamalla, L. P. Singer, J. Singhal, M. Sinha, B. M. Sipőcz, L. R. Spitler, D. Stansby, O. Streicher, J. Šumak, J. D. Swinbank, D. S. Taranu, N. Tewary, G. R. Tremblay, M. d. Val-Borro, S. J. Van Kooten, Z. Vasović, S. Verma, J. V. de Miranda Cardoso, P. K. G. Williams, T. J. Wilson, B. Winkel, W. M. Wood-Vasey, R. Xue, P. Yoachim, C. Zhang, A. Zonca, and Astropy Project Contributors. The Astropy Project: Sustaining and Growing a Community-oriented Open-source Project and the Latest Major Release (v5.0) of the Core Package. *Astrophysical Journal*, 935(2):167, Aug. 2022. doi: 10.3847/1538-4357/ac7c74.

S. Banfi, F. Vazza, and D. Wittor. Shock waves in the magnetized cosmic web: the role of obliquity and cosmic ray acceleration. *Monthly Notices of the Royal Astronomical Society*, 496(3):3648–3667, Aug. 2020. doi: 10.1093/mnras/staa1810.

R. Beck and M. Krause. Revised equipartition and minimum energy formula for magnetic field strength estimates from radio synchrotron observations. *Astronomische Nachrichten*, 326(6):414–427, July 2005. doi: 10.1002/asna.200510366.

N. Biava, F. de Gasperin, A. Bonafede, H. W. Edler, S. Giacintucci, P. Mazzotta, G. Brunetti, A. Botteon, M. Brüggen, R. Cassano, A. Drabent, A. C. Edge, T. Enßlin, F. Gastaldello, C. J. Riseley, M. Rossetti, H. J. A. Rottgering, T. W. Shimwell, C. Tasse, and R. J. van Weeren. The ultra-steep diffuse radio emission observed in the cool-core cluster RX J1720.1+2638 with LOFAR at 54 MHz. *Monthly Notices of the Royal Astronomical Society*, 508(3):3995–4007, Dec. 2021. doi: 10.1093/mnras/stab2840.

M. Birkinshaw. The Sunyaev-Zel'dovich effect. *Physics Reports*, 310(2-3):97–195, Mar. 1999. doi: 10.1016/S0370-1573(98)00080-5.

H. Boehringer and N. Werner. X-ray Spectroscopy of Galaxy Clusters. *arXiv e-prints*, art. arXiv:0907.4277, July 2009.

A. Bonafede, L. Feretti, G. Giovannini, F. Govoni, M. Murgia, G. B. Taylor, H. Ebeling, S. Allen, G. Gentile, and Y. Pihlström. Revealing the magnetic field in a distant galaxy cluster: discovery of the complex radio emission from MACS J0717.5 +3745. *Astronomy and Astrophysics*, 503(3):707–720, Sept. 2009. doi: 10.1051/0004-6361/200912520.

A. Bonafede, L. Feretti, M. Murgia, F. Govoni, G. Giovannini, D. Dallacasa, K. Dolag, and G. B. Taylor. The Coma cluster magnetic field from Faraday rotation measures. *Astronomy and Astrophysics*, 513:A30, Apr. 2010. doi: 10.1051/0004-6361/200913696.

A. Bonafede, F. Govoni, L. Feretti, M. Murgia, G. Giovannini, and M. Brüggen. Fractional polarization as a probe of magnetic fields in the intra-cluster medium. *Astronomy and Astrophysics*, 530:A24, June 2011. doi: 10.1051/0004-6361/201016298.

A. Bonafede, M. Brüggen, R. van Weeren, F. Vazza, G. Giovannini, H. Ebeling, A. C. Edge, M. Hoeft, and U. Klein. Discovery of radio haloes and double relics in distant MACS galaxy clusters: clues to the efficiency of particle acceleration. *Monthly Notices of the Royal Astronomical Society*, 426(1):40–56, Oct. 2012. doi: 10.1111/j.1365-2966.2012.21570.x.

A. Bonafede, F. Vazza, M. Brüggen, M. Murgia, F. Govoni, L. Feretti, G. Giovannini, and G. Ogrean. Measurements and simulation of Faraday rotation across the Coma radio relic. *Monthly Notices of the Royal Astronomical Society*, 433(4): 3208–3226, Aug. 2013. doi: 10.1093/mnras/stt960.

A. Bonafede, H. T. Intema, M. Brüggen, M. Girardi, M. Nonino, N. Kantharia, R. J. van Weeren, and H. J. A. Röttgering. Evidence for Particle Re-acceleration in the Radio Relic in the Galaxy Cluster PLCKG287.0+32.9. *Astrophysical Journal*, 785(1):1, Apr. 2014a. doi: 10.1088/0004-637X/785/1/1.

A. Bonafede, H. T. Intema, M. Bruggen, H. R. Russell, G. Ogrean, K. Basu, M. Sommer, R. J. van Weeren, R. Cassano, A. C. Fabian, and H. J. A. Rottgering. A giant radio halo in the cool core cluster CL1821+643. *Monthly Notices of the Royal Astronomical Society*, 444:L44–L48, Oct. 2014b. doi: 10.1093/mnrasl/slu110.

M. A. Brentjens and A. G. de Bruyn. Faraday rotation measure synthesis. *Astronomy and Astrophysics*, 441(3):1217–1228, Oct. 2005. doi: 10.1051/0004-6361: 20052990.

D. S. Briggs. *High fidelity deconvolution of moderately resolved sources.* PhD thesis, New Mexico Institute of Mining and Technology, Jan. 1995.

M. Brüggen, A. Bykov, D. Ryu, and H. Röttgering. Magnetic Fields, Relativistic Particles, and Shock Waves in Cluster Outskirts. *Space Science Reviews*, 2012.

G. Brunetti and T. W. Jones. Cosmic Rays in Galaxy Clusters and Their Nonthermal Emission. *International Journal of Modern Physics D*, 23(4):1430007-98, Mar. 2014. doi: 10.1142/S0218271814300079.

G. Brunetti and A. Lazarian. Stochastic reacceleration of relativistic electrons by turbulent reconnection: a mechanism for cluster-scale radio emission? *Monthly Notices of the Royal Astronomical Society*, 458(3):2584–2595, May 2016. doi: 10.1093/mnras/stw496.

G. Brunetti, G. Setti, L. Feretti, and G. Giovannini. Particle reacceleration in the Coma cluster: radio properties and hard X-ray emission. *Monthly Notices of the Royal Astronomical Society*, 320(3):365–378, Jan. 2001. doi: 10.1046/j.1365-8711. 2001.03978.x.

E. Bulbul, M. Markevitch, A. Foster, R. K. Smith, M. Loewenstein, and S. W. Randall. Detection of an Unidentified Emission Line in the Stacked X-Ray Spectrum of Galaxy Clusters. *Astrophysical Journal*, 789(1):13, July 2014. doi: 10.1088/0004-637X/789/1/13.

B. J. Burn. On the depolarization of discrete radio sources by Faraday dispersion. *Monthly Notices of the Royal Astronomical Society*, 133:67, Jan. 1966. doi: 10.1093/mnras/133.1.67.

J. E. Carlstrom, G. P. Holder, and E. D. Reese. Cosmology with the Sunyaev-Zel'dovich Effect. *Annual Review of Astronomy and Astrophysics*, 40:643–680, Jan. 2002. doi: 10.1146/annurev.astro.40.060401.093803.

E. Carretti, V. Vacca, S. P. O'Sullivan, G. H. Heald, C. Horellou, H. J. A. Röttgering, A. M. M. Scaife, T. W. Shimwell, A. Shulevski, C. Stuardi, and T. Vernstrom. Magnetic field strength in cosmic web filaments. *Monthly Notices of the Royal Astronomical Society*, 512(1):945–959, May 2022. doi: 10.1093/mnras/stac384.

R. Cassano, G. Brunetti, H. J. A. Röttgering, and M. Brüggen. Unveiling radio halos in galaxy clusters in the LOFAR era. *Astronomy and Astrophysics*, 509: A68, Jan. 2010a. doi: 10.1051/0004-6361/200913063.

R. Cassano, S. Ettori, S. Giacintucci, G. Brunetti, M. Markevitch, T. Venturi, and M. Gitti. On the Connection Between Giant Radio Halos and Cluster Mergers. *Astrophysical Journal, Letters*, 721(2):L82–L85, Oct. 2010b. doi: 10.1088/2041-8205/721/2/L82.

A. Cavaliere and R. Fusco-Femiano. The Distribution of Hot Gas in Clusters of Galaxies. *Astronomy and Astrophysics*, 70:677, Nov. 1978.

E. Churazov, R. Sunyaev, W. Forman, and H. Böhringer. Cooling flows as a calorimeter of active galactic nucleus mechanical power. *Monthly Notices of the Royal Astronomical Society*, 332(3):729–734, May 2002. doi: 10.1046/j.1365-8711.2002.05332.x.

A. Cimatti, F. Fraternali, and C. Nipoti. *Introduction to Galaxy Formation and Evolution: From Primordial Gas to Present-Day Galaxies.* 2019.

B. G. Clark. An efficient implementation of the algorithm 'CLEAN'. *Astronomy and Astrophysics*, 89(3):377, Sept. 1980.

T. E. Clarke. Faraday Rotation Observations of Magnetic Fields in Galaxy Clusters. *Journal of Korean Astronomical Society*, 37(5):337–342, Dec. 2004. doi: 10.5303/JKAS.2004.37.5.337.

T. E. Clarke, P. P. Kronberg, and H. Böhringer. A New Radio-X-Ray Probe of Galaxy Cluster Magnetic Fields. *Astrophysical Journal, Lettersl*, 2001.

J. J. Condon and S. M. Ransom. *Essential Radio Astronomy.* 2016.

J. E. Conway, T. J. Cornwell, and P. N. Wilkinson. Multi-frequency synthesis : a new technique in radio interferometrie imaging. *Monthly Notices of the Royal Astronomical Society*, 246:490, Oct. 1990.

T. J. Cornwell. Multiscale clean deconvolution of radio synthesis images. *IEEE Journal of Selected Topics in Signal Processing*, 2(5):793–801, 2008. doi: 10.1109/JSTSP.2008.2006388.

T. J. Cornwell, K. Golap, and S. Bhatnagar. The Noncoplanar Baselines Effect in Radio Interferometry: The W-Projection Algorithm. *IEEE Journal of Selected Topics in Signal Processing*, 2(5):647–657, Nov. 2008. doi: 10.1109/JSTSP.2008.2005290.

L. L. Cowie and A. Songaila. Thermal evaporation of gas within galaxies by a hot intergalactic medium. *Nature*, 1977.

C. S. Crawford, S. W. Allen, H. Ebeling, A. C. Edge, and A. C. Fabian. The ROSAT Brightest Cluster Sample - III. Optical spectra of the central cluster galaxies. *Monthly Notices of the Royal Astronomical Society*, 1999.

F. de Gasperin, E. Orrú, M. Murgia, A. Merloni, H. Falcke, R. Beck, R. Beswick, L. Bîrzan, A. Bonafede, M. Brüggen, G. Brunetti, K. Chyży, J. Conway, J. H. Croston, T. Enßlin, C. Ferrari, G. Heald, S. Heidenreich, N. Jackson, G. Macario, J. McKean, G. Miley, R. Morganti, A. Offringa, R. Pizzo, D. Rafferty, H. Röttgering, A. Shulevski, M. Steinmetz, C. Tasse, S. van der Tol, W. van Driel, R. J. van Weeren, J. E. van Zwieten, A. Alexov, J. Anderson, A. Asgekar, M. Avruch, M. Bell, M. R. Bell, M. Bentum, G. Bernardi, P. Best, F. Breitling, J. W. Broderick, A. Butcher, B. Ciardi, R. J. Dettmar, J. Eisloeffel, W. Frieswijk, H. Gankema, M. Garrett, M. Gerbers, J. M. Griessmeier, A. W. Gunst, T. E. Hassall, J. Hessels, M. Hoeft, A. Horneffer, A. Karastergiou, J. Köhler, Y. Koopman, M. Kuniyoshi, G. Kuper, P. Maat, G. Mann, M. Mevius, D. D. Mulcahy, H. Munk, R. Nijboer, J. Noordam, H. Paas, M. Pandey, V. N. Pandey, A. Polatidis, W. Reich, A. P. Schoenmakers, J. Sluman, O. Smirnov, C. Sobey, B. Stappers, J. Swinbank, M. Tagger, Y. Tang, I. van Bemmel, W. van Cappellen, A. P. van Duin, M. van Haarlem, J. van Leeuwen, R. Vermeulen, C. Vocks, S. White, M. Wise, O. Wucknitz, and P. Zarka. M 87 at metre wavelengths: the LOFAR picture. *Astronomy and Astrophysics*, 547:A56, Nov. 2012. doi: 10.1051/0004-6361/201220209.

F. de Gasperin, R. J. van Weeren, M. Brüggen, F. Vazza, A. Bonafede, and H. T. Intema. A new double radio relic in PSZ1 G096.89+24.17 and a radio relic mass-luminosity relation. *Monthly Notices of the Royal Astronomical Society*, 444(4): 3130–3138, Nov. 2014. doi: 10.1093/mnras/stu1658.

F. de Gasperin, L. Rudnick, A. Finoguenov, D. Wittor, H. Akamatsu, M. Brüggen, J. O. Chibueze, T. E. Clarke, W. Cotton, V. Cuciti, P. Domínguez-Fernández, K. Knowles, S. P. O'Sullivan, and L. Sebokolodi. MeerKAT view of the diffuse radio sources in Abell 3667 and their interactions with the thermal plasma. *Astronomy and Astrophysics*, 659:A146, Mar. 2022. doi: 10.1051/0004-6361/202142658.

G. Di Gennaro, R. J. van Weeren, L. Rudnick, M. Hoeft, M. Brüggen, D. Ryu, H. J. A. Röttgering, W. Forman, A. Stroe, T. W. Shimwell, R. P. Kraft, C. Jones, and D. N. Hoang. Downstream Depolarization in the Sausage Relic: A 1-4 GHz

Very Large Array Study. *Astrophysical Journal*, 911(1):3, Apr. 2021. doi: 10.3847/1538-4357/abe620.

K. Dolag, M. Bartelmann, and H. Lesch. SPH simulations of magnetic fields in galaxy clusters. *Astronomy and Astrophysics*, 348:351–363, Aug. 1999.

K. Dolag, S. Schindler, F. Govoni, and L. Feretti. Correlation of the magnetic field and the intra-cluster gas density in galaxy clusters. *Astronomy and Astrophysics*, 378:777–786, Nov. 2001. doi: 10.1051/0004-6361:20011219.

K. Dolag, M. Bartelmann, and H. Lesch. Evolution and structure of magnetic fields in simulated galaxy clusters. *Astronomy and Astrophysics*, 387:383–395, May 2002. doi: 10.1051/0004-6361:20020241.

P. Domínguez-Fernández, F. Vazza, M. Brüggen, and G. Brunetti. Dynamical evolution of magnetic fields in the intracluster medium. *Monthly Notices of the Royal Astronomical Society*, 486(1):623–638, June 2019. doi: 10.1093/mnras/stz877.

J. Donnert, F. Vazza, M. Brüggen, and J. ZuHone. Magnetic Field Amplification in Galaxy Clusters and Its Simulation. *Space Science Reviews*, 214(8):122, Dec. 2018. doi: 10.1007/s11214-018-0556-8.

A. Dressler. Galaxy morphology in rich clusters: implications for the formation and evolution of galaxies. *Astrophysical Journal*, 1980.

T. A. Enßlin and M. Brüggen. On the formation of cluster radio relics. *Monthly Notices of the Royal Astronomical Society*, 331(4):1011–1019, Apr. 2002. doi: 10.1046/j.1365-8711.2002.05261.x.

T. A. Enßlin and Gopal-Krishna. Reviving fossil radio plasma in clusters of galaxies by adiabatic compression in environmental shock waves. *Astronomy and Astrophysics*, 366:26–34, Jan. 2001. doi: 10.1051/0004-6361:20000198.

T. A. Enßlin, P. L. Biermann, U. Klein, and S. Kohle. Cluster radio relics as a tracer of shock waves of the large-scale structure formation. *Astronomy and Astrophysics*, 332:395–409, Apr. 1998.

A. C. Fabian. Observational Evidence of Active Galactic Nuclei Feedback. *Annual Review of Astronomy and Astrophysics*, 50:455–489, Sept. 2012. doi: 10.1146/annurev-astro-081811-125521.

B. L. Fanaroff and J. M. Riley. The morphology of extragalactic radio sources of high and low luminosity. *Monthly Notices of the Royal Astronomical Society*, 167:31P–36P, May 1974. doi: 10.1093/mnras/167.1.31P.

K. Finner, K. HyeongHan, M. J. Jee, D. Wittman, W. R. Forman, R. J. van Weeren, N. R. Golovich, W. A. Dawson, A. Jones, F. de Gasperin, and C. Jones. Exemplary Merging Clusters: Weak-lensing and X-Ray Analysis of the Double Radio Relic, Merging Galaxy Clusters MACS J1752.0+4440 and ZWCL 1856.8+6616. *Astrophysical Journal*, 918(2):72, Sept. 2021. doi: 10.3847/1538-4357/ac0d00.

M. Gendron-Marsolais, J. Hlavacek-Larrondo, R. J. van Weeren, T. Clarke, A. C. Fabian, H. T. Intema, G. B. Taylor, K. M. Blundell, and J. S. Sanders. Deep 230-470 MHz VLA observations of the mini-halo in the Perseus cluster. *Monthly Notices of the Royal Astronomical Society*, 469(4):3872–3880, Aug. 2017. doi: 10.1093/mnras/stx1042.

M. Gendron-Marsolais, J. Hlavacek-Larrondo, R. J. van Weeren, L. Rudnick, T. E. Clarke, B. Sebastian, T. Mroczkowski, A. C. Fabian, K. M. Blundell, E. Sheldahl, K. Nyland, J. S. Sanders, W. M. Peters, and H. T. Intema. High-resolution VLA low radio frequency observations of the Perseus cluster: radio lobes, mini-halo, and bent-jet radio galaxies. *Monthly Notices of the Royal Astronomical Society*, 499(4):5791–5805, Dec. 2020. doi: 10.1093/mnras/staa2003.

S. J. George, J. M. Stil, and B. W. Keller. Detection Thresholds and Bias Correction in Polarized Intensity. *Publications of the Astronomical Society of Australia*, 29 (3):214–220, Oct. 2012. doi: 10.1071/AS11027.

S. Giacintucci, M. Markevitch, G. Brunetti, J. A. ZuHone, T. Venturi, P. Mazzotta, and H. Bourdin. Mapping the Particle Acceleration in the Cool Core of the Galaxy Cluster RX J1720.1+2638. *Astrophysical Journal*, 795(1):73, Nov. 2014. doi: 10.1088/0004-637X/795/1/73.

G. Giovannini, M. Tordi, and L. Feretti. Radio halo and relic candidates from the NRAO VLA Sky Survey. *New Astronomy*, 4(2):141–155, Mar. 1999. doi: 10.1016/S1384-1076(99)00018-4.

G. Giovannini, A. Bonafede, L. Feretti, F. Govoni, M. Murgia, F. Ferrari, and G. Monti. Radio halos in nearby (z ¡ 0.4) clusters of galaxies. *Astronomy and Astrophysics*, 507(3):1257–1270, Dec. 2009. doi: 10.1051/0004-6361/200912667.

G. Giovannini, M. Cau, A. Bonafede, H. Ebeling, L. Feretti, M. Girardi, M. Gitti, F. Govoni, A. Ignesti, M. Murgia, G. Taylor, and V. Vacca. Diffuse radio sources in a statistically complete sample of high redshift galaxy clusters. 06 2020.

N. Golovich, W. A. Dawson, D. M. Wittman, M. J. Jee, B. Benson, B. C. Lemaux, R. J. van Weeren, F. Andrade-Santos, D. Sobral, F. de Gasperin, M. Brüggen, M. Bradač, K. Finner, and A. Peter. Merging Cluster Collaboration: Optical and Spectroscopic Survey of a Radio-selected Sample of 29 Merging Galaxy Clusters. *Astrophysical Journal, Supplement*, 240(2):39, Feb. 2019. doi: 10.3847/1538-4365/aaf88b.

F. Govoni and L. Feretti. Magnetic Fields in Clusters of Galaxies. *International Journal of Modern Physics D*, 13(8):1549–1594, Jan. 2004. doi: 10.1142/S0218271804005080.

F. Govoni, M. Murgia, H. Xu, H. Li, M. L. Norman, L. Feretti, G. Giovannini, and V. Vacca. Polarization of cluster radio halos with upcoming radio interferometers. *Astronomy and Astrophysics*, 554:A102, June 2013. doi: 10.1051/0004-6361/201321403.

F. Govoni, M. Murgia, V. Vacca, F. Loi, M. Girardi, F. Gastaldello, G. Giovannini, L. Feretti, R. Paladino, E. Carretti, R. Concu, A. Melis, S. Poppi, G. Valente, G. Bernardi, A. Bonafede, W. Boschin, M. Brienza, T. E. Clarke, S. Colafrancesco, F. de Gasperin, D. Eckert, T. A. Enßlin, C. Ferrari, L. Gregorini, M. Johnston-Hollitt, H. Junklewitz, E. Orrù, P. Parma, R. Perley, M. Rossetti, G. B Taylor, and F. Vazza. Sardinia Radio Telescope observations of Abell 194. The intra-cluster magnetic field power spectrum. *Astronomy and Astrophysics*, 603:A122, July 2017. doi: 10.1051/0004-6361/201630349.

J. E. Gunn and I. Gott, J. Richard. On the Infall of Matter Into Clusters of Galaxies and Some Effects on Their Evolution. *Astrophysical Journal*, 1972.

F. Guo and J. Giacalone. The Acceleration of Electrons at Collisionless Shocks Moving Through a Turbulent Magnetic Field. *Astrophysical Journal*, 802(2):97, Apr. 2015. doi: 10.1088/0004-637X/802/2/97.

J.-H. Ha, D. Ryu, and H. Kang. Properties of Merger Shocks in Merging Galaxy Clusters. *Astrophysical Journal*, 857(1):26, Apr. 2018. doi: 10.3847/1538-4357/aab4a2.

C. A. Hales, B. M. Gaensler, R. P. Norris, and E. Middelberg. Analytic detection thresholds for measurements of linearly polarized intensity using rotation measure synthesis. *Monthly Notices of the Royal Astronomical Society*, 424(3):2160–2172, Aug. 2012. doi: 10.1111/j.1365-2966.2012.21372.x.

M. J. Hardcastle and J. H. Croston. Radio galaxies and feedback from AGN jets. *New Astronomy Review*, 88:101539, June 2020. doi: 10.1016/j.newar.2020.101539.

G. Heald. The Faraday rotation measure synthesis technique. In K. G. Strassmeier, A. G. Kosovichev, and J. E. Beckman, editors, *Cosmic Magnetic Fields: From Planets, to Stars and Galaxies*, volume 259, pages 591–602, Apr. 2009. doi: 10.1017/S1743921309031421.

D. N. Hoang, T. W. Shimwell, A. Stroe, H. Akamatsu, G. Brunetti, J. M. F. Donnert, H. T. Intema, D. D. Mulcahy, H. J. A. Röttgering, R. J. van Weeren, A. Bonafede, M. Brüggen, R. Cassano, K. T. Chyży, T. Enßlin, C. Ferrari, F. de Gasperin, L. Gu, M. Hoeft, G. K. Miley, E. Orrú, R. Pizzo, and G. J. White. Deep LOFAR observations of the merging galaxy cluster CIZA J2242.8+5301. *Monthly Notices of the Royal Astronomical Society*, 471(1):1107–1125, Oct. 2017. doi: 10.1093/mnras/stx1645.

M. Hoeft and M. Brüggen. Radio signature of cosmological structure formation shocks. *Monthly Notices of the Royal Astronomical Society*, 375(1):77–91, Feb. 2007. doi: 10.1111/j.1365-2966.2006.11111.x.

J. A. Högbom. Aperture Synthesis with a Non-Regular Distribution of Interferometer Baselines. *Astronomy and Astrophysics, Supplement*, 1974.

W. J. Jaffe. Origin and transport of electrons in the halo radio source in the Coma cluster. *Astrophysical Journal*, 212:1–7, Feb. 1977. doi: 10.1086/155011.

M. Johnston-Hollitt, S. Dehghan, and L. Pratley. Using the morphology and magnetic fields of tailed radio galaxies as environmental probes. In F. Massaro, C. C. Cheung, E. Lopez, and A. Siemiginowska, editors, *Extragalactic Jets from Every Angle*, 2015.

A. Jones, F. de Gasperin, V. Cuciti, D. N. Hoang, A. Botteon, M. Brüggen, G. Brunetti, K. Finner, W. R. Forman, C. Jones, R. P. Kraft, T. Shimwell, and R. J. van Weeren. Radio relics in PSZ2 G096.88+24.18: a connection with pre-existing plasma. *Monthly Notices of the Royal Astronomical Society*, 2021.

T. Kahniashvili, Y. Maravin, A. Natarajan, N. Battaglia, and A. G. Tevzadze. Constraining Primordial Magnetic Fields through Large-scale Structure. *Astrophysical Journal*, 770(1):47, June 2013. doi: 10.1088/0004-637X/770/1/47.

A. V. Kravtsov and S. Borgani. Formation of Galaxy Clusters. *Annual Review of Astronomy and Astrophysics*, 50:353–409, Sept. 2012. doi: 10.1146/annurev-astro-081811-125502.

A. G. Kritsuk. Dynamics of the sweeping of interstellar clouds from a rotating galaxy as it moves in the intergalactic medium. *Astrophysics*, 1983.

L. D. Landau and E. M. Lifshit's. *Theory of elasticity*. 1959.

E. Le Roux. Étude théorique du rayonnement synchrotron des radiosources. *Annales d'Astrophysique*, 24:71, Feb. 1961.

N. T. Locatelli, K. Rajpurohit, F. Vazza, F. Gastaldello, D. Dallacasa, A. Bonafede, M. Rossetti, C. Stuardi, E. Bonassieux, G. Brunetti, M. Brüggen, and T. Shimwell. Discovering the most elusive radio relic in the sky: diffuse shock acceleration caught in the act? *Monthly Notices of the Royal Astronomical Society*, 496(1): L48–L53, July 2020. doi: 10.1093/mnrasl/slaa074.

M. S. Longair. *High Energy Astrophysics*. 2011.

P. Mazzotta and S. Giacintucci. Do Radio Core-Halos and Cold Fronts in Non-Major-Merging Clusters Originate from the Same Gas Sloshing? *Astrophysical Journal, Letters*, 675(1):L9, Mar. 2008. doi: 10.1086/529433.

J. P. McMullin, B. Waters, D. Schiebel, W. Young, and K. Golap. CASA Architecture and Applications. In R. A. Shaw, F. Hill, and D. J. Bell, editors, *Astronomical Data Analysis Software and Systems XVI*, volume 376 of *Astronomical Society of the Pacific Conference Series*, page 127, Oct. 2007.

B. R. McNamara, P. E. J. Nulsen, M. W. Wise, D. A. Rafferty, C. Carilli, C. L. Sarazin, and E. L. Blanton. The heating of gas in a galaxy cluster by X-ray cavities and large-scale shock fronts. *Nature*, 433(7021):45–47, Jan. 2005. doi: 10.1038/nature03202.

G. Miley. The structure of extended extragalactic radio sources. *Annual Review of Astronomy and Astrophysics*, 1980.

M. Murgia, F. Govoni, L. Feretti, G. Giovannini, D. Dallacasa, R. Fanti, G. B. Taylor, and K. Dolag. Magnetic fields and Faraday rotation in clusters of galaxies. *Astronomy and Astrophysics*, 424:429–446, Sept. 2004. doi: 10.1051/0004-6361:20040191.

C. Nipoti. The special growth history of central galaxies in groups and clusters. *Monthly Notices of the Royal Astronomical Society*, 467(1):661–673, May 2017. doi: 10.1093/mnras/stx112.

J. Oemler, A. The structure of elliptical and cD galaxies. *Astrophysical Journal*, 1976.

A. R. Offringa, B. McKinley, N. Hurley-Walker, F. H. Briggs, R. B. Wayth, D. L. Kaplan, M. E. Bell, L. Feng, A. R. Neben, J. D. Hughes, J. Rhee, T. Murphy, N. D. R. Bhat, G. Bernardi, J. D. Bowman, R. J. Cappallo, B. E. Corey, A. A. Deshpande, D. Emrich, A. Ewall-Wice, B. M. Gaensler, R. Goeke, L. J. Greenhill, B. J. Hazelton, L. Hindson, M. Johnston-Hollitt, D. C. Jacobs, J. C. Kasper, E. Kratzenberg, E. Lenc, C. J. Lonsdale, M. J. Lynch, S. R. McWhirter, D. A. Mitchell, M. F. Morales, E. Morgan, N. Kudryavtseva, D. Oberoi, S. M. Ord, B. Pindor, P. Procopio, T. Prabu, J. Riding, D. A. Roshi, N. U. Shankar, K. S. Srivani, R. Subrahmanyan, S. J. Tingay, M. Waterson, R. L. Webster, A. R. Whitney, A. Williams, and C. L. Williams. WSCLEAN: an implementation of a fast, generic wide-field imager for radio astronomy. *Monthly Notices of the Royal Astronomical Society*, 444(1):606–619, Oct. 2014. doi: 10.1093/mnras/stu1368.

E. Osinga, R. J. van Weeren, F. Andrade-Santos, L. Rudnick, A. Bonafede, T. Clarke, K. Duncan, S. Giacintucci, T. Mroczkowski, and H. J. A. Röttgering. The detection of cluster magnetic fields via radio source depolarisation. *arXiv e-prints*, art. arXiv:2207.09717, July 2022.

S. P. O'Sullivan, S. Brown, T. Robishaw, D. H. F. M. Schnitzeler, N. M. McClure-Griffiths, I. J. Feain, A. R. Taylor, B. M. Gaensler, T. L. Landecker, L. Harvey-Smith, and E. Carretti. Complex Faraday depth structure of active galactic nuclei as revealed by broad-band radio polarimetry. *Monthly Notices of the Royal Astronomical Society*, 421(4):3300–3315, Apr. 2012. doi: 10.1111/j.1365-2966.2012.20554.x.

V. Petrosian. On the Nonthermal Emission and Acceleration of Electrons in Coma and Other Clusters of Galaxies. *Astrophysical Journal*, 557(2):560–572, Aug. 2001. doi: 10.1086/321557.

C. Pfrommer, V. Springel, T. A. Enßlin, and M. Jubelgas. Detecting shock waves in cosmological smoothed particle hydrodynamics simulations. *Monthly Notices of the Royal Astronomical Society*, 367(1):113–131, Mar. 2006. doi: 10.1111/j.1365-2966.2005.09953.x.

C. Pfrommer, R. Pakmor, K. Schaal, C. M. Simpson, and V. Springel. Simulating cosmic ray physics on a moving mesh. *Monthly Notices of the Royal Astronomical Society*, 465(4):4500–4529, Mar. 2017. doi: 10.1093/mnras/stw2941.

Planck Collaboration, P. A. R. Ade, N. Aghanim, M. Arnaud, M. Ashdown, J. Aumont, C. Baccigalupi, A. Balbi, A. J. Banday, R. B. Barreiro, M. Bartelmann, J. G. Bartlett, E. Battaner, R. Battye, K. Benabed, A. Benoît, J. P. Bernard, M. Bersanelli, R. Bhatia, J. J. Bock, A. Bonaldi, J. R. Bond, J. Borrill, F. R. Bouchet, M. L. Brown, M. Bucher, C. Burigana, P. Cabella, C. M. Cantalupo, J. F. Cardoso, P. Carvalho, A. Catalano, L. Cayón, A. Challinor, A. Chamballu, R. R. Chary, L. Y. Chiang, C. Chiang, G. Chon, P. R. Christensen, E. Churazov, D. L. Clements, S. Colafrancesco, S. Colombi, F. Couchot, A. Coulais, B. P. Crill, F. Cuttaia, A. da Silva, H. Dahle, L. Danese, R. J. Davis, P. de Bernardis, G. de Gasperis, A. de Rosa, G. de Zotti, J. Delabrouille, J. M. Delouis, F. X. Désert, C. Dickinson, J. M. Diego, K. Dolag, H. Dole, S. Donzelli, O. Doré, U. Dörl, M. Douspis, X. Dupac, G. Efstathiou, P. Eisenhardt, T. A. Enßlin, F. Feroz, F. Finelli, I. Flores-Cacho, O. Forni, P. Fosalba, M. Frailis, E. Franceschi, S. Fromenteau, S. Galeotta, K. Ganga, R. T. Génova-Santos, M. Giard, G. Giardino, Y. Giraud-Héraud, J. González-Nuevo, R. González-Riestra, K. M. Górski, K. J. B. Grainge, S. Gratton, A. Gregorio, A. Gruppuso, D. Harrison, P. Heinämäki, S. Henrot-Versillé, C. Hernández-Monteagudo, D. Herranz, S. R. Hildebrandt, E. Hivon, M. Hobson, W. A. Holmes, W. Hovest, R. J. Hoyland, K. M. Huffenberger, G. Hurier, N. Hurley-Walker, A. H. Jaffe, W. C. Jones, M. Juvela, E. Keihänen, R. Keskitalo, T. S. Kisner, R. Kneissl, L. Knox, H. Kurki-Suonio, G. Lagache, J. M. Lamarre, A. Lasenby, R. J. Laureijs, C. R. Lawrence, M. Le Jeune, S. Leach, R. Leonardi, C. Li, A. Liddle, P. B. Lilje, M. Linden-Vørnle, M. López-Caniego, P. M. Lubin, J. F. Macías-Pérez, C. J. MacTavish, B. Maffei, D. Maino, N. Mandolesi, R. Mann, M. Maris, F. Marleau, E. Martínez-González, S. Masi, S. Matarrese, F. Matthai, P. Mazzotta, S. Mei, P. R. Meinhold, A. Melchiorri, J. B. Melin, L. Mendes, A. Mennella, S. Mitra, M. A. Miville-Deschênes, A. Moneti, L. Montier, G. Morgante, D. Mortlock, D. Munshi, A. Murphy, P. Naselsky, F. Nati, P. Natoli, C. B. Netterfield, H. U. Nørgaard-Nielsen, F. Noviello, D. Novikov, I. Novikov, M. Olamaie, S. Osborne, F. Pajot, F. Pasian, G. Patanchon, T. J. Pearson, O. Perdereau, L. Perotto, F. Perrotta, F. Piacentini, M. Piat, E. Pierpaoli, R. Piffaretti, S. Plaszczynski, E. Pointecouteau, G. Polenta, N. Ponthieu, T. Poutanen, G. W. Pratt, G. Prézeau, S. Prunet, J. L. Puget, J. P. Rachen, W. T. Reach, R. Rebolo, M. Reinecke, C. Renault, S. Ricciardi, T. Riller, I. Ristorcelli, G. Rocha, C. Rosset, J. A. Rubiño-Martín, B. Rusholme, E. Saar, M. Sandri, D. Santos, R. D. E. Saunders, G. Savini, B. M. Schaefer, D. Scott, M. D. Seiffert, P. Shellard, G. F. Smoot, A. Stanford, J. L. Starck, F. Stivoli, V. Stolyarov, R. Stompor, R. Sudiwala, R. Sunyaev, D. Sutton, J. F. Sygnet, N. Taburet, J. A. Tauber, L. Terenzi, L. Toffolatti, M. Tomasi, J. P. Torre, M. Tristram, J. Tuovinen, L. Valenziano, L. Vibert, P. Vielva, F. Villa, N. Vittorio, L. A. Wade, B. D. Wandelt, J. Weller, S. D. M. White, M. White, D. Yvon, A. Zacchei, and A. Zonca. Planck early results. VIII. The all-sky early Sunyaev-Zeldovich cluster sample. *Astronomy and Astrophysics*, 536:A8, Dec. 2011. doi: 10.1051/0004-6361/201116459.

Planck Collaboration, P. A. R. Ade, N. Aghanim, M. Arnaud, M. Ashdown, J. Aumont, C. Baccigalupi, A. J. Banday, R. B. Barreiro, R. Barrena, J. G. Bartlett, N. Bartolo, E. Battaner, R. Battye, K. Benabed, A. Benoît, A. Benoit-Lévy,

J. P. Bernard, M. Bersanelli, P. Bielewicz, I. Bikmaev, H. Böhringer, A. Bonaldi, L. Bonavera, J. R. Bond, J. Borrill, F. R. Bouchet, M. Bucher, R. Burenin, C. Burigana, R. C. Butler, E. Calabrese, J. F. Cardoso, P. Carvalho, A. Catalano, A. Challinor, A. Chamballu, R. R. Chary, H. C. Chiang, G. Chon, P. R. Christensen, D. L. Clements, S. Colombi, L. P. L. Colombo, C. Combet, B. Comis, F. Couchot, A. Coulais, B. P. Crill, A. Curto, F. Cuttaia, H. Dahle, L. Danese, R. D. Davies, R. J. Davis, P. de Bernardis, A. de Rosa, G. de Zotti, J. Delabrouille, F. X. Désert, C. Dickinson, J. M. Diego, K. Dolag, H. Dole, S. Donzelli, O. Doré, M. Douspis, A. Ducout, X. Dupac, G. Efstathiou, P. R. M. Eisenhardt, F. Elsner, T. A. Enßlin, H. K. Eriksen, E. Falgarone, J. Fergusson, F. Feroz, A. Ferragamo, F. Finelli, O. Forni, M. Frailis, A. A. Fraisse, E. Franceschi, A. Frejsel, S. Galeotta, S. Galli, K. Ganga, R. T. Génova-Santos, M. Giard, Y. Giraud-Héraud, E. Gjerløw, J. González-Nuevo, K. M. Górski, K. J. B. Grainge, S. Gratton, A. Gregorio, A. Gruppuso, J. E. Gudmundsson, F. K. Hansen, D. Hanson, D. L. Harrison, A. Hempel, S. Henrot-Versillé, C. Hernández-Monteagudo, D. Herranz, S. R. Hildebrandt, E. Hivon, M. Hobson, W. A. Holmes, A. Hornstrup, W. Hovest, K. M. Huffenberger, G. Hurier, A. H. Jaffe, T. R. Jaffe, T. Jin, W. C. Jones, M. Juvela, E. Keihänen, R. Keskitalo, I. Khamitov, T. S. Kisner, R. Kneissl, J. Knoche, M. Kunz, H. Kurki-Suonio, G. Lagache, J. M. Lamarre, A. Lasenby, M. Lattanzi, C. R. Lawrence, R. Leonardi, J. Lesgourgues, F. Levrier, M. Liguori, P. B. Lilje, M. Linden-Vørnle, M. López-Caniego, P. M. Lubin, J. F. Macías-Pérez, G. Maggio, D. Maino, D. S. Y. Mak, N. Mandolesi, A. Mangilli, P. G. Martin, E. Martínez-González, S. Masi, S. Matarrese, P. Mazzotta, P. McGehee, S. Mei, A. Melchiorri, J. B. Melin, L. Mendes, A. Mennella, M. Migliaccio, S. Mitra, M. A. Miville-Deschênes, A. Moneti, L. Montier, G. Morgante, D. Mortlock, A. Moss, D. Munshi, J. A. Murphy, P. Naselsky, A. Nastasi, F. Nati, P. Natoli, C. B. Netterfield, H. U. Nørgaard-Nielsen, F. Noviello, D. Novikov, I. Novikov, M. Olamaie, C. A. Oxborrow, F. Paci, L. Pagano, F. Pajot, D. Paoletti, F. Pasian, G. Patanchon, T. J. Pearson, O. Perdereau, L. Perotto, Y. C. Perrott, F. Perrotta, V. Pettorino, F. Piacentini, M. Piat, E. Pierpaoli, D. Pietrobon, S. Plaszczynski, E. Pointecouteau, G. Polenta, G. W. Pratt, G. Prézeau, S. Prunet, J. L. Puget, J. P. Rachen, W. T. Reach, R. Rebolo, M. Reinecke, M. Remazeilles, C. Renault, A. Renzi, I. Ristorcelli, G. Rocha, C. Rosset, M. Rossetti, G. Roudier, E. Rozo, J. A. Rubiño-Martín, C. Rumsey, B. Rusholme, E. S. Rykoff, M. Sandri, D. Santos, R. D. E. Saunders, M. Savelainen, G. Savini, M. P. Schammel, D. Scott, M. D. Seiffert, E. P. S. Shellard, T. W. Shimwell, L. D. Spencer, S. A. Stanford, D. Stern, V. Stolyarov, R. Stompor, A. Streblyanska, R. Sudiwala, R. Sunyaev, D. Sutton, A. S. Suur-Uski, J. F. Sygnet, J. A. Tauber, L. Terenzi, L. Toffolatti, M. Tomasi, D. Tramonte, M. Tristram, M. Tucci, J. Tuovinen, G. Umana, L. Valenziano, J. Valiviita, B. Van Tent, P. Vielva, F. Villa, L. A. Wade, B. D. Wandelt, I. K. Wehus, S. D. M. White, E. L. Wright, D. Yvon, A. Zacchei, and A. Zonca. Planck 2015 results. XXVII. The second Planck catalogue of Sunyaev-Zeldovich sources. *Astronomy and Astrophysics*, 594:A27, Sept. 2016. doi: 10.1051/0004-6361/201525823.

C. R. Purcell, C. L. Van Eck, J. West, X. H. Sun, and B. M. Gaensler. RM-Tools:

Rotation measure (RM) synthesis and Stokes QU-fitting. Astrophysics Source Code Library, record ascl:2005.003, May 2020.

K. Rajpurohit, M. Hoeft, R. J. van Weeren, L. Rudnick, H. J. A. Röttgering, W. R. Forman, M. Brüggen, J. H. Croston, F. Andrade-Santos, W. A. Dawson, H. T. Intema, R. P. Kraft, C. Jones, and M. J. Jee. Deep VLA Observations of the Cluster 1RXS J0603.3+4214 in the Frequency Range of 1-2 GHz. *Astrophysical Journal*, 852(2):65, Jan. 2018. doi: 10.3847/1538-4357/aa9f13.

K. Rajpurohit, R. J. van Weeren, M. Hoeft, F. Vazza, M. Brienza, W. Forman, D. Wittor, P. Domínguez-Fernández, S. Rajpurohit, C. J. Riseley, A. Botteon, E. Osinga, G. Brunetti, E. Bonnassieux, A. Bonafede, A. S. Rajpurohit, C. Stuardi, A. Drabent, M. Brüggen, D. Dallacasa, T. W. Shimwell, H. J. A. Röttgering, F. d. Gasperin, G. K. Miley, and M. Rossetti. Deep Low-frequency Radio Observations of A2256. I. The Filamentary Radio Relic. *Astrophysical Journal*, 927(1): 80, Mar. 2022. doi: 10.3847/1538-4357/ac4708.

U. Rau and T. J. Cornwell. A multi-scale multi-frequency deconvolution algorithm for synthesis imaging in radio interferometry. *Astronomy and Astrophysics*, 532: A71, Aug. 2011. doi: 10.1051/0004-6361/201117104.

M. J. Rees. Origin of cosmic magnetic fields. *Astronomische Nachrichten*, 327:395, June 2006. doi: 10.1002/asna.200610540.

Y. Rephaeli. Relativistic electrons in the intracluster space of clusters of galaxies: the hard X-ray spectra and heating of the gas. *Astrophysical Journal*, 227:364–369, Jan. 1979. doi: 10.1086/156740.

Y. Rephaeli, M. Ulmer, and D. Gruber. OSSE Search for High-Energy X-Ray Emission from the Coma Cluster. *Astrophysical Journal*, 429:554, July 1994. doi: 10.1086/174343.

M. Ruszkowski and S. P. Oh. Shaken and Stirred: Conduction and Turbulence in Clusters of Galaxies. *Astrophysical Journal*, 713(2):1332–1342, Apr. 2010. doi: 10.1088/0004-637X/713/2/1332.

D. Ryu, H. Kang, E. Hallman, and T. W. Jones. Cosmological Shock Waves and Their Role in the Large-Scale Structure of the Universe. *Astrophysical Journal*, 593(2):599–610, Aug. 2003. doi: 10.1086/376723.

C. L. Sarazin. *X-ray emission from clusters of galaxies.* 1988.

C. L. Sarazin and J. C. Kempner. Nonthermal Bremsstrahlung and Hard X-Ray Emission from Clusters of Galaxies. *Astrophysical Journal*, 533(1):73–83, Apr. 2000. doi: 10.1086/308649.

C. E. Shannon. Communication in the Presence of Noise. *IEEE Proceedings*, 37: 10–21, Jan. 1949. doi: 10.1109/JPROC.1998.659497.

D. D. Sokoloff, A. A. Bykov, A. Shukurov, E. M. Berkhuijsen, R. Beck, and A. D. Poezd. Depolarization and Faraday effects in galaxies. *Monthly Notices of the Royal Astronomical Society*, 299(1):189–206, Aug. 1998. doi: 10.1046/j.1365-8711.1998.01782.x.

J. Spitzer, Lyman and W. Baade. Stellar Populations and Collisions of Galaxies. *Astrophysical Journal*, 1951.

C. Stuardi, A. Bonafede, L. Lovisari, P. Domínguez-Fernández, F. Vazza, M. Brüggen, R. J. van Weeren, and F. de Gasperin. The intracluster magnetic field in the double relic galaxy cluster Abell 2345. *Monthly Notices of the Royal Astronomical Society*, 502(2):2518–2535, Apr. 2021. doi: 10.1093/mnras/stab218.

C. Stuardi, A. Bonafede, K. Rajpurohit, M. Brüggen, F. de Gasperin, D. Hoang, R. J. van Weeren, and F. Vazza. Using the polarization properties of double radio relics to probe the turbulent compression scenario. *arXiv e-prints*, art. arXiv:2207.00503, July 2022.

R. A. Sunyaev and Y. B. Zeldovich. The Spectrum of Primordial Radiation, its Distortions and their Significance. *Comments on Astrophysics and Space Physics*, 2:66, Mar. 1970.

J. C. Tarter. *The Interaction of Gas and Galaxies Within Galaxy Clusters.* PhD thesis, University of California, Berkeley, Jan. 1975.

A. R. Thompson, J. M. Moran, and J. Swenson, George W. *Interferometry and Synthesis in Radio Astronomy, 3rd Edition.* 2017. doi: 10.1007/978-3-319-44431-4.

P. C. Tribble. Radio emission in random magnetic field : radio haloes and the structure of the magnetic field in the Coma cluster. *Monthly Notices of the Royal Astronomical Society*, 253:147, Nov. 1991. doi: 10.1093/mnras/253.1.147.

V. Vacca, M. Murgia, F. Govoni, T. Enßlin, N. Oppermann, L. Feretti, G. Giovannini, and F. Loi. Magnetic Fields in Galaxy Clusters and in the Large-Scale Structure of the Universe. *Galaxies*, 6(4):142, Dec. 2018. doi: 10.3390/galaxies6040142.

R. J. van Weeren, H. J. A. Röttgering, M. Brüggen, and M. Hoeft. Particle Acceleration on Megaparsec Scales in a Merging Galaxy Cluster. *Science*, 330(6002): 347, Oct. 2010. doi: 10.1126/science.1194293.

R. J. van Weeren, G. Brunetti, M. Brüggen, F. Andrade-Santos, G. A. Ogrean, W. L. Williams, H. J. A. Röttgering, W. A. Dawson, W. R. Forman, F. de Gasperin, M. J. Hardcastle, C. Jones, G. K. Miley, D. A. Rafferty, L. Rudnick, J. Sabater, C. L. Sarazin, T. W. Shimwell, A. Bonafede, P. N. Best, L. Bîrzan, R. Cassano, K. T. Chyży, J. H. Croston, T. J. Dijkema, T. Enßlin, C. Ferrari, G. Heald, M. Hoeft, C. Horellou, M. J. Jarvis, R. P. Kraft, M. Mevius, H. T. Intema, S. S. Murray, E. Orrú, R. Pizzo, S. S. Sridhar, A. Simionescu, A. Stroe, S. van der Tol, and G. J. White. LOFAR, VLA, and Chandra Observations of the Toothbrush Galaxy Cluster. *Astrophysical Journal*, 818(2):204, Feb. 2016. doi: 10.3847/0004-637X/818/2/204.

R. J. van Weeren, G. A. Ogrean, C. Jones, W. R. Forman, F. Andrade-Santos, C. J. J. Pearce, A. Bonafede, M. Brüggen, E. Bulbul, T. E. Clarke, E. Churazov, L. David, W. A. Dawson, M. Donahue, A. Goulding, R. P. Kraft, B. Mason, J. Merten, T. Mroczkowski, P. E. J. Nulsen, P. Rosati, E. Roediger, S. W. Randall, J. Sayers, K. Umetsu, A. Vikhlinin, and A. Zitrin. Chandra and JVLA Observations of HST Frontier Fields Cluster MACS J0717.5+3745. *Astrophysical Journal*, 835(2):197, Feb. 2017. doi: 10.3847/1538-4357/835/2/197.

R. J. van Weeren, F. de Gasperin, H. Akamatsu, M. Brüggen, L. Feretti, H. Kang, A. Stroe, and F. Zandanel. Diffuse Radio Emission from Galaxy Clusters. *Space Science Reviews*, 2019.

F. Vazza and M. Brüggen. Do radio relics challenge diffusive shock acceleration? *Monthly Notices of the Royal Astronomical Society*, 437(3):2291–2296, Jan. 2014. doi: 10.1093/mnras/stt2042.

F. Vazza, M. Brüggen, R. van Weeren, A. Bonafede, K. Dolag, and G. Brunetti. Why are central radio relics so rare? *Monthly Notices of the Royal Astronomical Society*, 421(3):1868–1873, Apr. 2012. doi: 10.1111/j.1365-2966.2011.20160.x.

F. Vazza, M. Brüggen, C. Gheller, and P. Wang. On the amplification of magnetic fields in cosmic filaments and galaxy clusters. *Monthly Notices of the Royal Astronomical Society*, 445(4):3706–3722, Dec. 2014. doi: 10.1093/mnras/stu1896.

F. Vazza, D. Eckert, M. Brüggen, and B. Huber. Electron and proton acceleration efficiency by merger shocks in galaxy clusters. *Monthly Notices of the Royal Astronomical Society*, 451(2):2198–2211, Aug. 2015. doi: 10.1093/mnras/stv1072.

F. Vazza, M. Brüggen, D. Wittor, C. Gheller, D. Eckert, and M. Stubbe. Constraining the efficiency of cosmic ray acceleration by cluster shocks. *Monthly Notices of the Royal Astronomical Society*, 459(1):70–83, June 2016. doi: 10.1093/mnras/stw584.

F. Vazza, G. Brunetti, M. Brüggen, and A. Bonafede. Resolved magnetic dynamo action in the simulated intracluster medium. *Monthly Notices of the Royal Astronomical Society*, 474(2):1672–1687, Feb. 2018. doi: 10.1093/mnras/stx2830.

T. Venturi, M. Rossetti, G. Brunetti, D. Farnsworth, F. Gastaldello, S. Giacintucci, D. V. Lal, L. Rudnick, T. W. Shimwell, D. Eckert, S. Molendi, and M. Owers. The two-component giant radio halo in the galaxy cluster Abell 2142. *Astronomy and Astrophysics*, 603:A125, July 2017. doi: 10.1051/0004-6361/201630014.

A. Vikhlinin, A. Kravtsov, W. Forman, C. Jones, M. Markevitch, S. S. Murray, and L. Van Speybroeck. Chandra Sample of Nearby Relaxed Galaxy Clusters: Mass, Gas Fraction, and Mass-Temperature Relation. *Astrophysical Journal*, 640 (2):691–709, Apr. 2006. doi: 10.1086/500288.

A. von der Linden, A. Mantz, S. W. Allen, D. E. Applegate, P. L. Kelly, R. G. Morris, A. Wright, M. T. Allen, P. R. Burchat, D. L. Burke, D. Donovan, and H. Ebeling. Robust weak-lensing mass calibration of Planck galaxy clusters. *Monthly Notices* *of the Royal Astronomical Society*, 443(3):1973–1978, Sept. 2014. doi: 10.1093/mnras/stu1423.

J. F. C. Wardle and P. P. Kronberg. The linear polarization of quasi-stellar radio sources at 3.71 and 11.1 centimeters. *Astrophysical Journal*, 194:249, Jan. 1974. doi: 10.1086/153240.

Wikipedia. Faraday effect — wikipedia, the free encyclopedia, 2022. URL `https://en.wikipedia.org/wiki/Faraday_effect`.

M. A. G. Willson. Radio observations of the cluster of galaxies in Coma Berenices - the 5C4 survey. *Monthly Notices of the Royal Astronomical Society*, 151:1, Jan. 1970. doi: 10.1093/mnras/151.1.1.

D. Wittor, F. Vazza, and M. Brüggen. Testing cosmic ray acceleration with radio relics: a high-resolution study using MHD and tracers. *Monthly Notices of the Royal Astronomical Society*, 464(4):4448–4462, Feb. 2017. doi: 10.1093/mnras/stw2631.

J. A. ZuHone, M. Markevitch, G. Brunetti, and S. Giacintucci. Turbulence and Radio Mini-halos in the Sloshing Cores of Galaxy Clusters. *Astrophysical Journal*, 762(2):78, Jan. 2013. doi: 10.1088/0004-637X/762/2/78.

J. A. ZuHone, G. Brunetti, S. Giacintucci, and M. Markevitch. Testing Secondary Models for the Origin of Radio Mini-Halos in Galaxy Clusters. *Astrophysical Journal*, 801(2):146, Mar. 2015. doi: 10.1088/0004-637X/801/2/146.

F. Zwicky, E. Herzog, P. Wild, M. Karpowicz, and C. T. Kowal. *Catalogue of galaxies and of clusters of galaxies, Vol. I.* 1961.